

DOCTORAL THESIS

Quantum Dynamics of Noble Gas Atoms and Methane in the Molecular Cavity of Fullerene: Terahertz Spectroscopy Study

Tanzeeha Jafari

TALLINN UNIVERSITY OF TECHNOLOGY
DOCTORAL THESIS
6/2025

Quantum Dynamics of Noble Gas Atoms and Methane in the Molecular Cavity of Fullerene: Terahertz Spectroscopy Study

TANZEEHA JAFARI



TALLINN UNIVERSITY OF TECHNOLOGY

School of Science

Department of Cybernetics

NATIONAL INSTITUTE OF CHEMICAL PHYSICS AND BIOPHYSICS

Laboratory of Chemical Physics

The dissertation was accepted for the defence of the degree of Doctor of Philosophy (Applied Physics) on 20 December 2024

Supervisor: PhD Toomas Rõõm,
National Institute of Chemical Physics and Biophysics,
Tallinn, Estonia

Co-supervisor: PhD Urmas Nagel,
National Institute of Chemical Physics and Biophysics,
Tallinn, Estonia

Opponents: Prof Ferenc Simon,
Faculty of Natural Sciences, Department of Physics,
Budapest University of Technology and Economics,
Budapest, Hungary

Prof Tanel Käämbre,
Institute of Physics, Laboratory of X-Ray Spectroscopy,
University of Tartu,
Tartu, Estonia

Defence of the thesis: 31 January 2025, Tallinn

Declaration:

Hereby I declare that this doctoral thesis, my original investigation and achievement, submitted for the doctoral degree at Tallinn University of Technology, has not been submitted for any academic degree elsewhere.

Tanzeeha Jafari

signature



European Union
European Regional
Development Fund



Investing
in your future

Copyright: Tanzeeha Jafari, 2025

ISSN 2585-6898 (publication)

ISBN 978-9916-80-248-9 (publication)

ISSN 2585-6901 (PDF)

ISBN 978-9916-80-249-6 (PDF)

DOI <https://doi.org/10.23658/taltech.6/2025>

Printed by Koopia Niini & Rauam

Jafari, T. (2025). Quantum Dynamics of Noble Gas Atoms and Methane in the Molecular Cavity of Fullerene: Terahertz Spectroscopy Study [TalTech Press]. <https://doi.org/10.23658/taltech.6/2025>

TALLINNA TEHNIKAÜLIKOO
DOKTORITÖÖ
6/2025

**Väarisgaasi aatomite ja metaani
kvantdünaamika fullereeni
molekulaarses õõnsuses:
terahertsspektroskoopia uurimus**

TANZEEHA JAFARI



Contents

List of publications	7
Author's contributions to the publications	8
Abbreviations	10
Symbols	11
Units	11
Introduction	13
1 Overview	15
1.1 Molecular C ₆₀	15
1.2 Crystalline C ₆₀	16
1.2.1 Intermolecular and intramolecular vibrations	18
1.3 Origin of endofullerenes	19
2 Theory	21
2.1 Quantized translational motion of confined atom: A@C ₆₀	21
2.1.1 Quantum dynamics of particles in spherically symmetric potential .	21
2.1.2 Spherical harmonic oscillator	21
2.1.3 Anharmonic 3D oscillator	23
2.1.4 Induced dipole moment	24
2.1.5 THz absorption line intensities	24
2.1.6 Matrix elements of the spherical potential and the dipole moment operator	25
2.1.7 Fitting of THz absorption spectra with the quantum mechanical model	26
2.2 Lennard-Jones two-body interaction potential	27
3 Experimental details	29
3.1 Infrared spectroscopy of molecules	29
3.2 Principles of FTIR spectroscopy	30
3.2.1 Michelson interferometer	30
3.2.2 Martin-Puplett interferometer	34
3.3 Spectrometer Vertex 80v	35
3.4 Preparation of endofullerene samples for THz spectroscopy	37
3.5 Variable temperature THz and IR spectroscopy from 5 to 300 K using Ver- tex 80v	39
3.6 Low temperature THz spectroscopy with TeslaFIR	40
3.7 Derivation of absorption spectra from the experimental data	42
4 Results and discussion	45
4.1 Noble gas atoms in C ₆₀	45
4.1.1 He@C ₆₀	45
4.1.2 Ne@C ₆₀	49
4.1.3 Ar@C ₆₀	50
4.1.4 Kr@C ₆₀	50

4.2 Methane inside C ₆₀	51
4.3 Comparison of spherical oscillator parameters and deviations from the model	52
5 Summary	57
List of Figures	61
References	62
Acknowledgements	69
Abstract.....	70
Kokkuvõte	72
Appendix 1.....	75
Appendix 2	87
Appendix 3	99
Curriculum Vitae	111
Elulookirjeldus.....	114

List of publications

The present Ph.D. thesis is based on the following publications that are referred to in the text by Roman numbers.

- I G. R. Bacanu, T. Jafari, M. Aouane, J. Rantaharju, M. Walkey, G. Hoffman, A. Shugai, U. Nagel, M. Jiménez- Ruiz, A. J. Horsewill, S. Rols, T. Rõõm, R. J. Whitby, and M. H. Levitt, "Experimental determination of the interaction potential between a helium atom and the interior surface of a C₆₀ fullerene molecule" *J. Chem. Phys.*, vol. 155, p. 144302, October 2021.
- II T. Jafari, G. R. Bacanu, A. Shugai, U. Nagel, M. Walkey, G. Hoffman, M. H. Levitt, R. J. Whitby, and T. Rõõm, *Phys. Chem. Chem. Phys.* 24, 9943–9952 (2022) "Terahertz spectroscopy of the helium endofullerene He@C₆₀," *Phys. Chem. Chem. Phys.*, vol. 24, p. 9943, April 2022.
- III T. Jafari, A. Shugai, U. Nagel, G. R. Bacanu, M. Aouane, M. Jiménez- Ruiz, S. Rols, S. Bloodworth, M. Walkey, G. Hoffman, R. J. Whitby, M. H. Levitt, and T. Rõõm, "Ne, Ar, and Kr oscillators in the molecular cavity of fullerene C₆₀," *J. Chem. Phys.*, vol. 158, p. 234305, June 2023.

Author's contributions to the publications

- I In 1, I carried out THz spectroscopy experiments on He samples with different filling factors in KBF₄. I analyzed the spectra and prepared figures for the paper.
- II In 2, I derived the potential parameters for He@C₆₀ by fitting THz spectra. I prepared the figures and wrote the manuscript.
- III In 3, I performed the THz experiment with Ne@C₆₀, Ar@C₆₀, and Kr@C₆₀. I interpreted the spectra, prepared some figures, and wrote the manuscript.

Approbation

I presented the results of the thesis at the following conferences:

1. **T. Jafari**, A. Shugai, T. Rõõm, U. Nagel, G. R. Bacanu, M. C. Walkey, G. Hoffman, M. H. Levitt, R. J. Whitby. "Quantized translational motion of ^3He and ^4He atoms inside C_{60} molecular cage," 5th Grandmaster Early-Career Workshop in Physics: 7–11 September 2020, Prague, Czech Republic, Virtual.
2. **T. Jafari**, A. Shugai, T. Rõõm, U. Nagel, G. R. Bacanu, M. C. Walkey, G. Hoffman, M. H. Levitt, R. J. Whitby. "Quantized translational motion of ^3He and ^4He atoms inside C_{60} molecular cage," Scientist from the Southampton University : 12 November 2020, Virtual.
3. **T. Jafari**, A. Shugai, T. Rõõm, U. Nagel, G. R. Bacanu, M. C. Walkey, G. Hoffman, M. H. Levitt, R. J. Whitby. "Quantized translational motion of ^3He and ^4He atoms inside C_{60} molecular cage," APS March Meeting : 15–19 March 2021, Virtual.
4. **T. Jafari**, A. Shugai, T. Rõõm, U. Nagel, G. R. Bacanu, M. C. Walkey, G. Hoffman, M. H. Levitt, R. J. Whitby. "Quantized translational motion of ^3He and ^4He atoms inside C_{60} molecular cage," GSFMT scientific conference : 14–15 June 2021, Tartu, Estonia.
5. **T. Jafari**, A. Shugai, T. Rõõm, U. Nagel, G. R. Bacanu, M. C. Walkey, S. Bloodworth, G. Hoffman, M. H. Levitt, R. J. Whitby. "Noble gas atom as a quantum oscillator in the fullerene C_{60} ," GSFMT scientific conference : 23–24 May 2023, Tartu, Estonia.
6. **T. Jafari**, A. Shugai, T. Rõõm, U. Nagel, G. R. Bacanu, M. C. Walkey, G. Hoffman, M. H. Levitt, R. J. Whitby. "Interaction of endohedral noble gas atom with fullerene C_{60} : THz study," Seminar KBF1 : 19 June 2023, Tallinn, Estonia.

Abbreviations

BMS	Beamsplitter
FIR	Far-infrared
FM	Fixed mirror
FTIR	Fast transform infrared
FWHM	Full width at half maximum
HPLC	High pressure liquid chromatography
INS	Inelastic Neutron Scattering
IR	Infrared
KBFI	National Institute of Chemical Physics and Biophysics (Keemilise ja Bioloogilise Füüsika Instituut)
LJ	Lennard-Jones
MIR	Mid-infrared
Ng	Noble gas
NIR	Near-infrared
RT	Room temperature, 293 K
THz	Terahertz, 1 THz = 10^{12} Hz
TR	Translational-rotational
UV	Ultraviolet
ZPD	Zero path difference of interferometer

Symbols

n	Principal quantum number of spherical harmonic oscillator
ℓ	Angular momentum quantum number of spherical harmonic oscillator
ω'	Angular frequency of spherical harmonic oscillator
c_0	Speed of light in vacuum, $c_0 = (\epsilon_0\mu_0)^{-1/2}$
k_B	Boltzmann constant
f	Frequency
ω	Angular frequency, $\omega = 2\pi f$
E	Energy, $E = \hbar\omega$
λ	Wavelength of electromagnetic radiation
T	Temperature
$\bar{\nu}$	Wavenumber, number of waves in one centimeter

Units

$$1 \text{ THz} = 10^{12} \text{ Hz} = 33 \text{ cm}^{-1} = 4.1 \text{ meV}$$

$$1 \text{ cm}^{-1} = 0.03 \text{ THz} = 0.12 \text{ meV}$$

$$1 \text{ meV} = 0.24 \text{ THz} = 8 \text{ cm}^{-1}$$

Introduction

Endohedral fullerene (also known as endofullerene), is a supramolecular complex in which atoms or molecules are embedded inside the hollow shell of nano-carbon cage. They are denoted as $X@C_n$ where X represents the encapsulated species and n is the number of C-atoms in the host fullerene. Among many derivatives of endofullerene, the molecular C_{60} , forming $X@C_{60}$ gather more attention due its most stable carbon structure. The confinement of the atoms or molecules inside C_{60} molecule breaks new ground in various research areas. Apart from the substantial study on confinement effects on the reactivity and properties of the C_{60} [1–4], significant research has also been devoted to exploring the physical characteristics of endohedral species in a constrained environment, with a major focus on small-molecule endofullerenes $H_2@C_{60}$ [5–16], $H_2O@C_{60}$ [16–23] and $HF@C_{60}$ [16, 24, 25]. C_{60} molecule is an ideal system to study the non-bonded host-guest interaction, which is dominated by weak van der Waals forces: carbon cages are homogeneous, highly symmetric and isolate the guest species from the outer surrounding.

The confining potential of C_{60} restricts the free motion of guest species, leading to the quantization of translational degrees of freedom. For molecular guests the system becomes more complicated due to the presence of additional degrees of freedom, rotational and vibrational. The confinement prompts the coupling of translational and rotational degrees of freedom, giving rise to translational-rotational (TR) energy levels. The fine structure of TR energy levels has been a subject of many theoretical and experimental studies on $CO@C_{60}$ [26], $H_2@C_{60}$ [7, 9, 12, 13, 27], $HF@C_{60}$ [16, 24, 25] and $H_2O@C_{60}$ [18, 22, 23, 28]. Furthermore, some encapsulated molecules exhibit nuclear spin isomerism. The Pauli exclusion principle imposes the correlation between nuclear spin states and the rotational states of a molecule, making the TR energy spectrum even more intriguing and complex.

The TR energy level structure, signature of the guest-host interaction, can be directly probed by Raman spectroscopy, inelastic neutron scattering (INS) and terahertz (THz) and infrared (IR) spectroscopy. Raman spectroscopy is an excellent technique to study the quantum dynamics of encapsulated species. However, most of the Raman study primarily focused on metallofullerenes [29–31]. The Raman studies of other endofullerenes is limited to the perturbation C_{60} vibrational modes by the host [32]. INS is a powerful tool to study motion of atoms and molecules. In general, it does not have specific selection rules [33, 34] like Raman and IR spectroscopies, thus a large number of energy levels can be probed. However, some nuclei are not good neutron scatterers which limits the number of molecules and atoms to be studied. Also, sample quantities of the order of 100 mg are required to obtain an adequate signal. Such quantities can be synthesized by molecular surgery [35] but not all the species can be encapsulated with the same high yield. For example, despite the fact that Kr has larger neutron scattering cross-section than Ne [36], the amount of the sample has been limited because Kr requires a larger orifice of an open cage fullerene than Ne and the yield in the photochemical closure of the large orifice is low. This limitation in sample quantity gives an advantage to THz and IR spectroscopy, which provide informative spectra even with a few mg of sample.

Here we present the results of THz and IR spectroscopic studies of several noble gas (Ng) atoms encapsulated in C_{60} , 3He , 4He , Ne, Ar, Kr and a spherical top molecule CH_4 . The first aim of this study is to probe the quantized translational motion of atoms. Naively, $Ng@C_{60}$ is not an ideal endohedral complex to study by THz spectroscopy because the encapsulated atom is neutral and does not have permanent electric dipole moment neither. Therefore, THz radiation does not interact with the translational motion of an atom. However, as observed in $H_2@C_{60}$ [12], the IR-activity is induced by the translational motion itself. This gives the motivation to test the induced-dipole-hypothesis on encapsulated

atoms. If the induced dipole moment is sufficiently strong the energy spectrum of quantized translational motion could be determined. If the test is successful this would mark the first THz study of the quantized translational mode of Ng@C₆₀.

The second goal is to experimentally derive the guest-host interaction potential energy functions for Ng@C₆₀. As the atom size increases, the potential well gets more tight. The potential should not depend on the isotope of an atom, it is on its mass. This could be verified explicitly by measuring the two isotopes of the helium. So, we intend to compare the tendencies for the interaction energies of guest species of different sizes and masses. There has been considerable theoretical research on noble gas endofullerenes with an emphasize on the host-guest interaction potential [32,37–39] but there is no experimental data to support the theoretical findings. Determining interaction potential function would be beneficial for quantum chemistry calculation of non-bonded dispersive interactions.

The third goal is to characterize the quantum dynamics of CH₄@C₆₀. Methane, like Ng@C₆₀, lacks a permanent dipole moment. CH₄ is a spherical top molecule and therefore it is expected that the TR coupling is negligible compared to diatomic molecules like H₂ and HF. Therefore the translational motion of its centre of mass can be treated separately from the rotations of the molecule. This adds an interesting member to the Ng atom series because CH₄ is lighter than Ne, Ar and Kr, and has diameter comparable to Ar. If the translational mode is visible in the THz spectra then the potential energy function of CH₄@C₆₀ could be compared with Ng@C₆₀ potentials. Therefore, a comparison of Ng@C₆₀ and CH₄@C₆₀ provides an insight into the quantum nature of a confined system and a clearer understanding of how mass and size affect the potential energy function.

1 Overview

In 1985 Kroto et al. [40] discovered a hollow sphere-shaped molecule C_{60} , shown in Fig. 1. It is the variant of fullerenes, an allotrope of carbon in which atoms are arranged as closed mesh structure. Another two most notable fullerenes beside C_{60} are C_{70} and C_{84} . Even after four decades, it remains the subject of interest for the research fraternity to trap atoms or molecules inside the hollow cavity and to study properties of these *endofullerenes*. Other classes of fullerene are *exohedral fullerenes* in which a chemical group is attached to the outer surface of the fullerene and *heterofullerenes* in which one or more carbon atoms are replaced by another atoms.

Endofullerenes can be classified as : endohedral metallofullerenes and endofullerenes. Endohedral metallofullerenes contain one or more metal atoms forming a chemical bond with the carbon cage whereas the hollow cage is usually not stable [41]. The endofullerenes contain atoms or small molecules without forming chemical bonds with the cage and the hollow host is stable. This classification is not strict as exemplified by the first discovered (metallo)endofullerene $La@C_{60}$ [42].

Here, we focus on endofullerenes $X@C_{60}$, where X represents a small atom or molecule. This chapter covers the basic structure of the C_{60} molecule, the properties of solid C_{60} , and the synthesis methods adopted to prepare endohedral complexes $X@C_{60}$.

1.1 Molecular C_{60}

The highly symmetric C_{60} molecule is composed of 60 carbon atoms placed at the vertices of a truncated icosahedron to form a hollow sphere, Fig. 1. The structure of C_{60} , with 32 faces arranged as 12 pentagons and 20 hexagons, is strikingly similar to that of a soccer ball. Each pentagonal face is connected to five hexagons whereas each hexagonal face is connected to three alternate hexagons and pentagons. This structure was first proposed together with the report of the discovery of C_{60} [40]. The distinct feature of the truncated icosahedron with C atoms at the vertices is that all C atoms are equivalent. This was later validated by the NMR spectrum of C_{60} , which consists of a single sharp ^{13}C line [43].

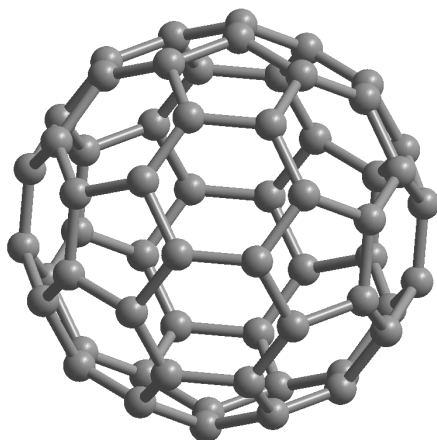


Figure 1: C_{60} molecule formed of sixty carbon atoms, gray spheres, connected by covalent bonds, sticks. The 3D structure of C_{60} is created by Diamond software [44].

Although the C_{60} molecule holds the icosahedral (I_h) symmetry and has the closest re-

semblance to the spherical molecule, it is not a regular truncated icosahedron due to non-equivalent bond lengths. 60 carbon atoms are connected by 90 covalent bonds, where 30 bonds are electron-rich double bonds and 60 are electron-deficient single bonds. The best current bond length estimates are from neutron diffraction [45]. At 4 K bond length $h = 138.1 \pm 0.3$ pm for C—C double-bond shared by two hexagons and $p = 146.0 \pm 0.2$ pm for C—C single-bond shared by a hexagon and a pentagon; the distance of all carbon atoms from the cage center $r = 354.7 \pm 0.5$ pm.

The icosahedral symmetry point group I_h has the largest number of symmetry elements among the point groups. The symmetry operations that transform a molecule into itself are rotation about an axis, reflection through the plane and inversion across a point. C_{60} has three rotational symmetry axes, Fig. 1. 1) Rotation about the axis connecting the

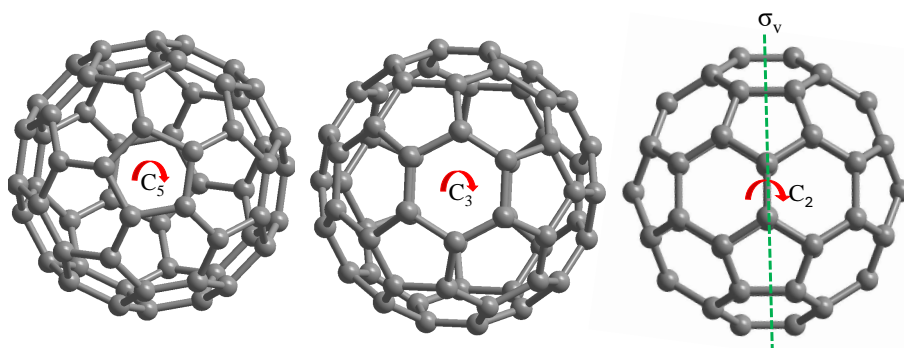


Figure 2: Rotational symmetry operations of C_{60} molecule. C_5 rotation axis connects the centres of two facing pentagons, C_3 rotation axis connects the centers of two facing hexagons and C_2 rotation axis is through the centres of the covalent bonds between the two hexagons. The green dotted line shows the σ_v mirror plane which bisect the C_{60} into two equal halves.

centers of two pentagons facing each other. $2\pi/5$ rotation about this axes leaves C_{60} invariant. There are 12 pentagons which gives 6 distinct 5-fold axes denoted as C_5 . 2) The rotation $2\pi/3$ about the axis through the centers of two hexagons facing each other. There are 20 hexagons what gives us 10 distinct C_3 axes. 3) Finally, the 2-fold rotations by π about the C_2 axis across the center of two opposite hexagonal edges. Likewise, since there are 30 hexagonal edges, there are 15 distinct 2-fold axes. The mirror symmetry element σ_v of C_{60} can be visualized as a mirror plane that contains the C_2 axis and the double bonds on the opposite sides of C_{60} . With 30 hexagonal edges, there are 15 distinct mirror planes. Finally, C_{60} has inversion symmetry about its geometric center. All the rotational symmetry operations are combined with the inversion, resulting in total of 120 distinct symmetry operations [46].

1.2 Crystalline C_{60}

C_{60} molecules are bound together by weak van der Waals force to form crystalline C_{60} . Under normal conditions at room temperature C_{60} molecules are in an orientationally disor-

dered phase, known as a plastic crystal phase. The uncorrelated rotation of C_{60} molecules in the solid phase has been studied by NMR [47] and quasi-elastic neutron scattering [48] and X-ray diffuse scattering [49]. The molecules of solid C_{60} are arranged in the face-centered cubic (fcc) lattice having four equivalent molecules per unit cell: one at the origin and others at the centers of faces of the cubic unit cell. This structure with lattice parameter 14.15 \AA has space group $Fm\bar{3}m$.

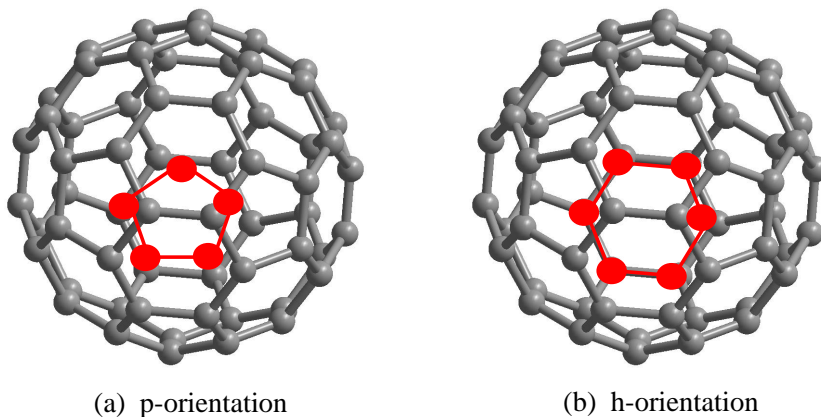


Figure 3: An illustration of the *p* and *h* orientation of C_{60} . C_{60} has electron-rich double bonds between two hexagons and electron-poor single bonds between hexagon and pentagon. (a) Pentagon moiety of C_{60} (red) facing electron rich double bond of neighbouring cage. (b) Hexagon moiety of C_{60} (red) facing electron rich double bond of neighbouring cage.

At temperature below $T \simeq 260 \text{ K}$, the crystalline C_{60} exhibits structural phase transition from the orientationally disordered to the ordered phase. The uncorrelated rotation of C_{60} molecules above 260 K turns into a uniaxial hindered rotation about one of the 3-fold axes below 260 K [50]. During this transition, molecules remain positioned at fcc sites but their rotation axis aligns along one of the four body-diagonals of the cubic unit cell. The fcc structure turns into crystal with four penetrating simple cubic (sc) sublattices each with fixed direction of $C_{60} C_3$ axis. This sc structure belongs to the space group $Pa\bar{3}$ (or T_h^6).

At $T = 90 \text{ K}$ there is another phase transition, below which crystalline C_{60} enters an orientationally frozen state where molecules stop rotating. Here molecules exist in two different orientations, depending on the alignment of central fullerene with its twelve neighboring C_{60} . In *p*-orientation, the electron-deficient pentagonal face is directly opposite to the electron-rich hexagonal double bond and in *h*-orientation the hexagonal face is directly opposite to electron rich double bond, see Fig 3. Below 90 K , a large fraction of molecules are locked in *p*-configuration while small number in *h*-configurations, resulting in a merohedral disorder. It has been reported that *p* configuration is 11.4 meV below *h* configuration and is therefore more populated at low temperatures [50]. The relative

population of molecules in the p and h configuration is 85% and 15%, respectively, meaning that on average every C_{60} molecule has two out of 12 neighbours in the h configuration. However, as the temperature goes above 90 K, the relative configuration fluctuates between dominant p and less dominant h, as the corresponding populations are temperature dependent [51].

During this whole phase transition starting from 300 K, the lattice parameter decreases slowly with temperature, with a significant drop at 260K, followed by a smooth transition with a slight jump at 90 K [50].

1.2.1 Intermolecular and intramolecular vibrations

The vibrations of crystalline C_{60} can be divided into intermolecular and intramolecular vibrations. Intermolecular, also known as the lattice modes, can be additionally subclassified into three categories: acoustic, optical, and librational modes. Acoustic modes in crystal dynamics are identified as in-phase vibrations of atoms within a unit cell, whereas optical modes are out-of phase vibrations of atoms at wave-vector $k = 0$. Both, the acoustic and optical modes are translational modes where the center of mass of an atom (or a molecule in a molecular crystal) moves. In a 3-dimensional crystal there are three acoustic modes which have zero energy at the k-vector $k = 0$ and $3(N - 1)$ optical modes at finite frequency at $k = 0$. With four molecules per unit cell, $N = 4$, solid C_{60} has three acoustic and nine optical modes. Librational mode, the third subclass of lattice modes, originates from the moment of inertia and includes back-and-forth rotation of C_{60} molecule about an axis with nearly fixed orientation. Number of rotational degrees of freedom is $3N$, which gives 12 librational modes in solid C_{60} . Hence, all together there are 24 intermolecular modes.

The lattice dynamics of C_{60} can be interpreted at low temperature where the rotation of C_{60} molecule turns into librational motion. The 24 lattice modes are superposition's of triply degenerate translations (T_u) and rotations (T_g) of four molecules. In the space group $Pa\bar{3}$ the 24 degrees of freedom give ten modes in the zone center ($k = 0$) classified according to irreducible representations as:

$$\Gamma_{\text{inter}} = A_g + E_g + 3T_g + A_u + E_u + 3T_u. \quad (1)$$

In Eq. 1, the even (g) and odd (u) modes are librational and translational modes, respectively. Out of three T_u modes, two T_u modes are IR-active optical modes and one T_u mode is the acoustic mode with zero energy at $k = 0$. A_u and E_u modes are neither IR nor Raman active. The librational modes of C_{60} are Raman-active as they are even.

The intermolecular lattice modes appear usually at low frequency ($\leq 100 \text{ cm}^{-1}$) due to the weak coupling between the C_{60} molecules, its large mass and moment of inertia. The librational modes are below 30 cm^{-1} whereas two IR-active translational modes have been observed between 40 and 60 cm^{-1} [50, 52, 53].

Fullerene C_{60} has 180 degrees of freedom. Subtracting 3 rotational and 3 translational degrees of freedom gives 174 vibrational degrees of freedom. Which leads to 46 distinct intramolecular (or molecular) modes, that correspond to the following irreducible representations:

$$\Gamma_{\text{intra}} = 2A_g + 3F_{1g} + 4F_{2g} + 6G_g + 8H_g + A_u + 4F_{1u} + 5F_{2u} + 6G_u + 7H_u \quad (2)$$

Due to the highly symmetric nature of C_{60} , a large number of molecular mode frequencies are degenerate. According to group theory, out of 46 modes, 10 are Raman active, 4 are

active in IR spectroscopy, and what remains, i.e., 32 are optically silent modes that can be accessed by INS spectroscopy.

Intramolecular modes are generally divided into two groups: radial modes ($240\text{ cm}^{-1} < E < 880\text{ cm}^{-1}$) and tangential modes ($920\text{ cm}^{-1} < E < 1600\text{ cm}^{-1}$). The radial modes involve radial displacement of carbon atoms while the tangential mode contains displacement which involves the contraction and stretching of C–C bonds. The lattice modes (phonons and librations) do not deform the molecular cage while the molecular modes deform the cage periodically.

Phonon state distribution shows a clear separation between low energy intermolecular modes ($E < 80\text{ cm}^{-1}$) and high energy intramolecular modes ($E > 240\text{ cm}^{-1}$), which coincides well with the nature of inter and intramolecular modes. This separation is usually called a “gap”, which is extended over the broad frequency range of around 160 cm^{-1} [50].

1.3 Origin of endofullerenes

The large central cavity of C_{60} gives an intuitive inspiration to scientists to fill the cavity with atoms, ions, molecules, or clusters giving rise to the concept of endofullerene. The first reported endohedral complex was metallo-endofullerene $La@C_{60}$, not long after the discovery of fullerene [42]. This complex was formed by laser vaporization of graphite impregnated with lanthanum. A few years later in 1991 [54], Smalley and coworkers synthesized $La@C_{82}$ using the sublimation technique, and in the same research, they also introduced @ notation for the first time to represent such endohedral complexes. This groundbreaking study triggered a new field of research which led to the exploration of various endofullerenes with different atoms and molecules encapsulated inside fullerene.

The first non-metal endofullerenes were reported in 1991 when in a series of mass spectroscopy experiments highly accelerated C_{60}^+ or C_{70}^+ were struck with the atoms in the helium gas which resulted in the insertion of a single He atom by C_{60} cage [55–58].

These experiments demonstrated the possibility of encapsulating endohedral species but were not ideal for large-scale production of endofullerenes.

The fullerenes are generally prepared by using the standard arc discharge method, in which carbon is vaporized at high temperature. Noble gas endofullerenes may be synthesized by vaporizing carbon in the presence of noble gas at high temperature so that noble gas atoms are captured during the formation of a carbon cage. Saunders et al. reported a small amount of $Ne@C_{60}$ and $He@C_{60}$ during the formation of fullerene in noble gas atmosphere [59].

Endofullerene may also be synthesized by subjecting fullerene to the high temperature and pressure of noble gases. Under high temperatures, the carbon bonds of C_{60} cage break temporarily, the atom penetrates through the wall and is trapped once the cage restores its shape. The high temperature and pressure experiment results in the incorporation of 0.1% of He, 0.2% of Ne, 0.3% of Ar and Kr and, 0.008% of Xe [60]. Subsequently, the incorporation fraction is improved by grounding C_{60} together with potassium cyanide (KCN) to form a fine mixture before exposing it to high temperature and pressure, which leads to 1% insertion of He and 0.3% of Ne, Ar and Kr [61–63]. Considerable enrichment was achieved for heavy Ng-atoms by removing the traces of empty C_{60} through many cycles of HPLC. However, the yield was quite, about 1 mg of $Kr@C_{60}$ with 99% filling, 1.3 mg $Ar@C_{60}$, 99% filled, and 0.3 mg of $Xe@C_{60}$, 50% filled. Similarly, $(2He)@C_{60}$, $N_2@C_{60/70}$ and $CO@C_{60}$ were synthesized by subjecting fullerene (C_{60} or C_{70}) to high temperature under the high pressure of the given diatomic gases [64]. Another approach for the synthesis of atomic endofullerene is ion implantation in which C_{60} is bombarded with ions generated from a plasma ion source. This method resulted in the production of rather a

small amount of N@C_{60} [65] and P@C_{60} [66]. Alternatively, glow discharge can be used for ion generation to encapsulate atomic nitrogen. This method also leads to the formation of a small amount of $\text{N}_2\text{@C}_{60}$ [67].

All of these methods produce atomic or molecule endofullerenes with a low yield. A new method, which does not need extreme conditions, was introduced by Rubin et al [68] and is known as “molecular surgery”. It was the first organic synthesis to insert an atom or molecule through open cage fullerene. The method involves a sequence of controlled chemical reactions to open the orifice of C_{60} , followed by widening of the orifice relative to the size of the atom or molecule, and finally putting the guest species into the cage at moderate temperature and pressure, resulting in an open cage endofullerene. By using molecular surgery approach, an open cage endofullerene comprising single ^3He or H_2 was synthesized, but with the low yield [68]. In a subsequent open cage endofullerene experiment Komatsu and coworkers effectively boosted the yield of H_2 to 100% [69], followed by the complete reseal of the cage to produce the first $\text{H}_2\text{@C}_{60}$ [70], which has proven to be one remarkable achievement. Down the same path, Murata and Kurotobi successfully encapsulated water molecule in C_{60} [71].

“Molecular surgery” has proven to be an optimum approach to produce endofullerenes with high-yield and now a broad range of non-metal endofullerenes are available in macroscopic quantity for spectroscopic studies: noble gas endofullerenes [72–74], $\text{H}_2\text{@C}_{60}$, $\text{H}_2\text{O@C}_{60}$ and their isotopologues, HF@C_{60} [75] and $\text{CH}_4\text{@C}_{60}$ [76]. There is also a possibility to incorporate two H_2 molecules inside C_{70} [77]. Our collaborators recently mark a milestone in organic chemistry by synthesizing $\text{CH}_2\text{O@C}_{60}$ [78]. This is a remarkable achievement because the largest van der Waals dimension of formaldehyde is larger than the cavity diameter of C_{60} .

2 Theory

In this chapter the quantum behavior of endohedral species in $A@C_{60}$ ($A = {}^3\text{He}, {}^4\text{He}, {}^{20}\text{Ne}, {}^{40}\text{Ar}, {}^{84}\text{Kr}$ and CH_4) is discussed in detail. The goal is to provide a model for the theoretical interpretation and analysis of THz spectroscopy results. The Hamiltonian for the translational motion of A trapped inside C_{60} fullerene is presented, and the confining potential is described as a function of the displacement \mathbf{r} from the C_{60} molecular cavity geometric center.

Although C_{60} holds the icosahedral symmetry, we assume spherical symmetry. In the light of this approximation, we can neglect the influence of C_{60} rotations and librations to the motion of encapsulated specie A . In addition, the potential function of A depends only on the length of \mathbf{r} and not on its orientation. Since the mass of C_{60} is one to two orders of magnitude larger than that of encapsulated species A , we assume that C_{60} center of mass is not moving because of the motion of A . We ignore the coupling of A to vibrations of C_{60} and to lattice modes of solid C_{60} . Hence, we assume that the confining potential is temperature independent. Thus, in this approximation, A moves in a spherically symmetric and rigid potential well and can be described by a spherical harmonic oscillator model with additional anharmonic terms. To describe quantitatively the THz line intensities of translational modes of $A@C_{60}$ we assume that in the course of translational motion when A moves off-center it acquires electric dipole moment on its interaction with C_{60} . This electric dipole moment couples to the electric field of THz radiation.

This chapter is concluded with the derivation of the Ng- C_{60} interaction potential from the two-body Ng-C Lennard-Jones (LJ) potentials using the parameters from the work of Pang and Brisse [38]. The LJ potential function will be compared to the experimentally determined spherical potential function in Chapter 4.

2.1 Quantized translational motion of confined atom: $A@C_{60}$

2.1.1 Quantum dynamics of particles in spherically symmetric potential

In quantum mechanics, the time-independent Schrödinger equation for n particle is

$$\hat{H}(\mathbf{r}_1, \mathbf{r}_2 \dots) \psi_{\mathbf{k}}(\mathbf{r}_1, \mathbf{r}_2 \dots, \mathbf{r}_n) = E_{\mathbf{k}} \psi_{\mathbf{k}}(\mathbf{r}_1, \mathbf{r}_2 \dots, \mathbf{r}_n), \quad (3)$$

where vectors $\mathbf{r}_1, \mathbf{r}_2 \dots, \mathbf{r}_n$ are the spatial coordinates of the n particles, $\psi_{\mathbf{k}}$ describes the eigenfunction, \mathbf{k} is any set of quantum numbers, $\mathbf{k} = \{k_1, k_2, k_3 \dots\}$, and $E_{\mathbf{k}}$ is the energy of that state. The Hamiltonian operator for a system of n interacting particles can be written as:

$$\hat{H}(\mathbf{r}_1, \mathbf{r}_2 \dots, \mathbf{r}_n) = \sum_{j=1}^n \frac{\hat{p}_j^2}{2M_j} + V(\mathbf{r}_1, \mathbf{r}_2 \dots, \mathbf{r}_n), \quad (4)$$

where \hat{p}_j is the momentum operator, and M_j is the mass of particle j and, $V(\mathbf{r}_1, \mathbf{r}_2 \dots, \mathbf{r}_n)$ is the potential energy function associated with n particles located at $\mathbf{r}_1, \mathbf{r}_2 \dots, \mathbf{r}_n$. For $A@C_{60}$, we treated C_{60} as a rigid body. Under this assumption A interacts with the entire C_{60} molecular cage as a whole rather than with each of the 60 C atoms individually. This approach simplifies the interaction between A and C_{60} .

2.1.2 Spherical harmonic oscillator

The spherical harmonic oscillator is the special case of eqn. (4) where a particle is subjected to quadratic potential in all spatial directions and the potential energy can be written as $V(r) = \frac{1}{2}kr^2$, where $k=m\omega^2$. The Hamiltonian of a particle of mass m of a spherically

symmetric oscillator is given by:

$$\hat{H}_0 = \frac{\hat{p}^2}{2m} + V(r), \quad (5)$$

$$\hat{H}_0 = \frac{\hat{p}^2}{2m} + V_2 r^2 = \frac{\hat{p}^2}{2m} + \frac{1}{2} m \omega^2 r^2. \quad (6)$$

where the position of particle is expressed in the spherical coordinates, $\mathbf{r} = (r, \theta, \phi)$. In the case of Ng@C₆₀, there is one trapped particle, thus the eigenfunction depends only on the position of Ng relative to the C₆₀ cage center. If we ignore the coupling of CH₄ rotations to its translational motion then \mathbf{r} is the position of CH₄ center of mass with respect to the C₆₀ cage center. The Schrödinger equation for a particle with mass m in the spherical potential is [79]:

$$-\frac{\hbar^2}{2m} \left[\frac{1}{r^2} \frac{\partial}{\partial r} \left(r^2 \frac{\partial}{\partial r} \right) + \frac{1}{r^2 \sin \theta} \frac{\partial}{\partial \theta} \left(\sin \theta \frac{\partial}{\partial \theta} \right) + \frac{1}{r^2 \sin^2 \theta} \left(\frac{\partial^2}{\partial \phi^2} \right) + V \right] \psi = E \psi. \quad (7)$$

To determine the solution of the Schrödinger equation, the wavefunction is decomposed into radial and angular parts:

$$\psi_{n\ell m}(r, \theta, \phi) = R_{n\ell}(r) Y_{\ell m}(\theta, \phi), \quad (8)$$

where r , θ and ϕ are defined within intervals $0 \leq r \leq \infty$, $0 \leq \theta \leq \pi$, and $0 \leq \phi \leq 2\pi$, respectively. Substituting eqn. (8) into eqn. (7) and separating the radial and angular parts we obtain two separate equations.

The angular part is

$$\sin \theta \frac{\partial}{\partial \theta} \left(\sin(\theta) \frac{\partial Y_{\ell m}}{\partial \theta} \right) + \frac{\partial^2 Y_{\ell m}}{\partial \phi^2} = -\ell(\ell+1) \sin^2(\theta) Y_{\ell m}. \quad (9)$$

The radial part can be simplified by introducing $w(r) = r R_{n\ell}(r)$:

$$-\frac{\hbar}{2m} \frac{\partial^2 w(r)}{\partial r^2} + \left[V(r) + \frac{\hbar^2}{2m} \frac{\ell(\ell+1)}{r^2} \right] w(r) = E w(r). \quad (10)$$

The solution of eqn. (9) is the spherical harmonics which are the function of θ and ϕ :

$$Y_{\ell m}(\theta, \phi) = (-1)^m \sqrt{\frac{(2\ell+1)(\ell-m)!}{4\pi(\ell+m)!}} e^{im\phi} P_{\ell m}(\cos(\theta)), \quad (11)$$

$$P_{\ell m}(x) = (1-x^2)^{m/2} \left(\frac{d}{dx} \right)^m P_{\ell}(x), \quad (12)$$

$$P_{\ell}(x) = \frac{1}{2^{\ell} \ell!} \left(\frac{d}{dx} \right)^{\ell} (x^2 - 1)^{\ell}. \quad (13)$$

Here, $P_{\ell m}$ and $P_{\ell}(x)$ are known as the associated Legendre function and the Legendre polynomials respectively, where ℓ is the orbital angular momentum, and m is the azimuthal quantum number that describes the projection of ℓ onto the quantization axis z . The phase convention used here is the Condon-Shortley phase convention where $(-1)^m$ is part of the spherical harmonic definition after omitting it in the definition of $P_{\ell m}$ [80]. Spherical harmonics are ortho-normalized:

$$\int_0^{2\pi} d\phi \int_0^{\pi} \sin \theta d\theta [Y_{\ell' m'}(\theta, \phi)]^* Y_{\ell m}(\theta, \phi) = \delta_{\ell \ell'} \delta_{m m'}, \quad (14)$$

and the complex conjugate is:

$$[Y_{\ell m}(\theta, \phi)]^* = Y_{\ell m}(\theta, -\phi) = (-1)^m Y_{\ell, -m}(\theta, \phi). \quad (15)$$

Sum over m for constant ℓ is [81]:

$$\sum_{m=-\ell}^{\ell} [Y_{\ell m}(\theta, \phi)]^* Y_{\ell m}(\theta, \phi) = \frac{2\ell+1}{4\pi}. \quad (16)$$

The solution of radial part of the wavefunction is:

$$R_{n\ell}(r) = \mathcal{C}(n, \ell, \zeta) e^{-\frac{\zeta r^2}{2}} (\zeta r^2)^{\frac{\ell}{2}} \mathcal{L}_{\frac{n-\ell}{2}}^{\ell+\frac{1}{2}} [\zeta r^2], \quad (17)$$

where $\mathcal{L}_n^{\ell+\frac{1}{2}}[x]$ is the generalized Laguerre polynomial, $\zeta = m\omega^t \hbar^{-1}$ and $\mathcal{C}(n, \ell, \zeta)$ is the normalization constant of radial wavefunction given as [82]:

$$\mathcal{C}(n, \ell, \zeta) = \sqrt{\frac{2 \left(\frac{n-\ell}{2}\right)!}{\left(\frac{n+\ell+1}{2}\right)!}} \zeta^{\frac{3}{4}}. \quad (18)$$

The angular frequency of the spherical harmonic oscillator is:

$$\omega^t = \sqrt{\frac{k}{m}} = \sqrt{\frac{2V_2}{m}}, \quad (19)$$

and the energy levels are:

$$E_{n,\ell} = \hbar\omega^t \left(n + \frac{3}{2}\right), \quad (20)$$

where n is the principal quantum number, ℓ is the angular momentum quantum number and m is the azimuthal quantum number. The allowed values of quantum numbers are:

$$\begin{aligned} n &\in \{0, 1, 2, \dots\}, \\ \ell &\in \{0, 2, \dots, n\}, \text{ for } n \text{ even}, \\ \ell &\in \{1, 3, \dots, n\}, \text{ for } n \text{ odd}, \\ m &\in \{-\ell, -\ell+1, \dots, \ell-1, \ell\}. \end{aligned} \quad (21)$$

For every ℓ there exist $(2\ell+1)$ values of m . The energy of the harmonic spherical oscillator is independent of ℓ and m and each $E_{n,\ell}$ is $(2\ell+1)$ -fold degenerate. As we see below, the degeneracy of energy levels in ℓ is lifted but not the degeneracy in m by the spherically symmetric anharmonic terms in the potential function.

2.1.3 Anharmonic 3D oscillator

The spherical harmonic oscillator potential $V(r) = \frac{1}{2}kr^2$ is not sufficient to accurately model the bounding potential of the endohedral species A inside C_{60} . To ensure reliable reproducibility of our experimental THz results, we add anharmonic corrections to the harmonic Hamiltonian. eqn. (6):

$$\hat{H} = \left(\frac{\hat{p}^2}{2m} + V_2 r^2\right) + V'(r), \quad (22)$$

$$V'(r) = V_4 r^4 + V_6 r^6 + \dots \quad (23)$$

In this case study, to accurately reproduce the observed THz line frequency of He@C₆₀ we include anharmonic potential terms $V_4 r^4$ and $V_6 r^6$. For other endohedral species, the anharmonic potential term $V_4 r^4$ was sufficient to adequately describe the THz absorption spectrum .

2.1.4 Induced dipole moment

To fit the peak intensities of THz absorption spectra $A@C_{60}$, the induced dipole moment operator is introduced. We derive the dipole moment term by assuming that the A is displaced from the center of the cage. The dipole term as a function of spherical harmonics of rank 1 can be written as:

$$d_{1m} = \sqrt{\frac{4\pi}{3}} A_{pm} r^p Y_{1m}(\theta, \phi), \quad (24)$$

where A_{1m} is real-valued dipole absorption coefficient amplitude and $m \in \{-1, 0, +1\}$. In spherical symmetry, there is no dependence on m , so for simplicity, the coefficient term can be written as $A_{pm} = A_p$. As dipole moment is a polar vector, so r takes odd values of p i.e, $p \in \{1, 3, \dots, n\}$. For $He@C_{60}$ studied here, first two terms were included for fitting:

$$d_{1m} = \sqrt{\frac{4\pi}{3}} (A_1 r + A_3 r^3) Y_{1m}(\theta, \phi) \quad (25)$$

and using eqn (16) the length of the induced dipole moment vector is:

$$|\mathbf{d}| = \sqrt{\sum_{m=-1}^{+1} (d_{1m})^* d_{1m}} = A_1 r + A_3 r^3. \quad (26)$$

For other studied endohedral species, we found that $A_1 r$ term is sufficient to describe the THz line intensities. Thus, we ignore the cubic and higher order dipole terms.

2.1.5 THz absorption line intensities

We use Fermi's Golden rule to describe the THz absorption line area for light linearly polarized in z direction, which interacts with the z component of dipole moment ($d_z = d_{10}$). The absorption coefficient is given as [22]:

$$\sigma_{fi} = \int_{\omega_{fi}} \alpha_{fi}(\omega) d\omega = N' f \frac{2\pi^2}{h\epsilon_0 c_0 \eta} \left(\frac{\eta^2 + 2}{3} \right)^2 \omega_{fi} (P_f - P_i) X_{fi}. \quad (27)$$

The integral is taken over the frequency range covering the full width of the absorption line corresponding to the transition from state $|i\rangle \rightarrow |f\rangle$. c_0 is the speed of light in vacuum, ϵ_0 is the permittivity of vacuum. According to [83], $(\eta^2 + 2)/3$ is the strength of the radiation electric field, experienced by the molecule embedded into the dielectric with index of refraction η (for C_{60} $\eta = 2$, Ref. [84]). $N' = 1.48 \times 10^{27} \text{ m}^{-3}$ is the number density of molecules in solid C_{60} and $f = N_\bullet/N'$ is the filling factor; $N' = N_o + N_\bullet$ where N_o is the number density of empty and N_\bullet is the number density of filled C_{60} cages. All quantities are in SI, and frequency ω_{fi} is calculated in wavenumbers defined as number of waves per unit meter, $[\omega_{fi}] = \text{m}^{-1}$.

P_k is the thermal Boltzmann population of initial ($k = i$) or final state ($k = f$):

$$P_k = \frac{e^{-E_k/k_B T}}{\sum_j (2\ell_j + 1) e^{-E_j/k_B T}}, \quad (28)$$

where $2\ell_j + 1$ is the degeneracy of state $|v_j, \ell_j, m_j\rangle$ in quantum number m_j and the sum runs over all states $|v_j, \ell_j, m_j\rangle$.

The X_{f_i} term is the square of the dipole matrix element given as:

$$\sum_{m_i, m_f} |\langle \mathbf{v}_f, \ell_f, m_f | d_{10} | \mathbf{v}_i, \ell_i, m_i \rangle|^2 = \frac{1}{3} |\langle \mathbf{v}_f, \ell_f || d_1 || \mathbf{v}_i, \ell_i \rangle|^2, \quad (29)$$

where $\langle \mathbf{v}_f, \ell_f || d_1 || \mathbf{v}_i, \ell_i \rangle$ is the reduced matrix element of d_{1m} , eqn. (25).

2.1.6 Matrix elements of the spherical potential and the dipole moment operator

To work with a basis which contains spherical harmonics it is useful to use the spherical tensor operator formalism [80, 81]. The matrix element of a spherical tensor operator $T_q^{(k)}$ of rank k is

$$\langle \ell_f m_f | T_q^{(k)} | \ell_i m_i \rangle = (-1)^{\ell_f - m_f} \begin{pmatrix} \ell_f & k & \ell_i \\ -m_f & q & m_i \end{pmatrix} \langle \ell_f || T^{(k)} || \ell_i \rangle, \quad (30)$$

where $|lm\rangle = Y_{lm}$ and the 2×3 array represents the Wigner $3j$ -symbol. The angular part of the reduced matrix element is the reduced matrix element of a spherical harmonic [80]:

$$\langle \ell_f || T^{(k)} || \ell_i \rangle \equiv \langle \ell_f || Y_k || \ell_i \rangle = (-1)^{\ell_f} \sqrt{\frac{(2\ell_f + 1)(2k + 1)(2\ell_i + 1)}{4\pi}} \begin{pmatrix} \ell_f & k & \ell_i \\ 0 & 0 & 0 \end{pmatrix}. \quad (31)$$

The $3j$ -symbol has the property that it vanishes if $|\ell_f - \ell_i| \leq k \leq \ell_f + \ell_i$ and $-m_f + q + m_i = 0$ is not true; if $m_f = q = m_i = 0$, then the $3j$ -symbol is not zero only if $\ell_f + k + \ell_i$ is an even number [80].

The spherical harmonic oscillator \hat{H}_0 , eqn (6), is diagonal within its own basis, eqn (8), with eigenenergies in the entries:

$$\langle \psi_{nlm} | \hat{H}_0 | \psi_{n'\ell'm'} \rangle = E_{n\ell} \delta_{nn'} \delta_{\ell\ell'} \delta_{mm'}, \quad (32)$$

where Kronecker delta $\delta_{nn'} = \delta_{\ell\ell'} = \delta_{mm'} = 1$ if $n = n'$, $\ell = \ell'$ and $m = m'$ and zero otherwise.

However, there is no exact analytical solution to eqn. (22) due to the significant complications caused by higher-order potential terms. Alternatively, the solution can be calculated using the numerical linear algebra method. One needs to build the matrix representation of the Hamiltonian operators to use such linear algebra techniques. The expression of a matrix element of a given Hamiltonian operator \hat{H} is given by:

$$\langle \psi_i | \hat{H} | \psi_j \rangle = \int_0^\infty \int_0^\pi \int_0^{2\pi} \psi_i^* \hat{H} \psi_j r^2 \sin(\theta) dr d\theta d\phi. \quad (33)$$

Since this is the case of a spherically symmetric oscillator, where the potential is independent of the angular variables θ and ϕ , the eqn. (33) can be simplified from orthonormalization condition of spherical harmonics, see eqn. (14).

To solve the Hamiltonian, we construct the matrix representation of \hat{H} using the basis set of \hat{H}_0 . The matrix is restricted to the finite size basis of the harmonic Hamiltonian \hat{H}_0 eigenstates; we used $n_{max} = 18$. The higher potential terms, $V_N, N > 2$ bring off-diagonal elements to the matrix representation. The Hamiltonian is numerically diagonalized with matrix elements given by $\langle \psi_{nlm} | \hat{H} | \psi_{n'\ell'm'} \rangle$.

Formally we can write the spherical potential, eqn. (23), as rank zero spherical tensor operator:

$$V(r) = V_4 r^4 + V_6 r^6 + \dots = \sqrt{4\pi} (V_4 r^4 + V_6 r^6 + \dots) Y_{00}, \quad (34)$$

where $Y_{00} = 1/\sqrt{4\pi}$. Under this condition, different ℓ and m eigenstates are not mixed. However, adding an anharmonic potential $V_N r^N$ results in mixing of the different n states

and the eigenstate of Hamiltonian of eqn. (22), $|v, \ell, m\rangle$, is then a linear superposition of eigenstates $|n, \ell, m\rangle$, eqn. (8).

While evaluating the matrix element $\langle R_{n_f \ell_f} | r^N | R_{n_i \ell_i} \rangle$ at $\ell_f = \ell_i$, it turns out that non-zero elements are $|n_f - n_i| \leq N$; n_i and n_f must have the same parity because $\ell_f = \ell_i$, consequence of eqn. (21). As the energy levels of the Hamiltonian in eqn. (22) are $(2\ell + 1)$ -fold degenerate in m , we can use the basis function $|n, \ell, 0\rangle$ by excluding m , which reduces the number of states by the factor of $(2\ell + 1)$ for each ℓ .

The rank of the electric dipole moment tensor is $k = 1$, eqn. (25). From the properties of 3 j -symbols we get the selection rule $\ell_f = \ell_i \pm 1$ for the THz absorption spectra. The selection rule for the quantum number n is determined by $\langle R_{n_f \ell_{i\pm 1}} | r^N | R_{n_i \ell_i} \rangle$. For the linear term in eqn. (25) the selection rule is $n_f = n_i \pm 1$ and for the cubic term it is $|n_f - n_i| \leq 3$; n_i and n_f must have different parity because of $\ell_f = \ell_i \pm 1$, consequence of eqn. (21).

2.1.7 Fitting of THz absorption spectra with the quantum mechanical model

To find the best fit parameters of the quantum mechanical model we minimize the difference between experimental spectra and spectra calculated with the quantum mechanical model. As there is always a background absorption in $A@C_{60}$, see Section 3.7, which is not the absorption by endohedral oscillator, two different approaches are used to determine the experimental line frequencies and intensities, one for He and the other for the rest of the atoms and CH_4 . In general, spherical oscillator has one absorption line in the limit of zero temperature. As the temperature is increased more lines appear in the spectrum. In the case of He these lines are well separated while for the other studied species they form a broad band.

For ${}^3He@C_{60}$ and ${}^4He@C_{60}$ a synthetic experimental spectrum $s(\omega_n)$ is calculated using the absorption line frequencies and line areas determined from the fits of experimental lines with the Gaussian lineshape function, see Ref [85, Fig. 6]. Since our quantum mechanical model does not describe line-broadening effects, the full-width at half maximum (FWHM) is set to the fixed value for all lines at all temperatures in the synthetic spectra; we use $\Delta\omega = 1.5 \text{ cm}^{-1}$. With this $\Delta\omega$ and Gaussian-fitted line frequencies and areas a synthetic experimental spectrum is calculated for each temperature with the distance between points in the spectrum $\omega_n - \omega_{n-1} = \Delta\omega/4$. For a given model Hamiltonian, eqn. (22), and the dipole operator, eqn. (25), the matrix elements are determined analytically in a symbolic form using the Wolfram Mathematica software [86]. The symbols are replaced for the numerical values of $\{\kappa\} = \{V_2, V_4, V_6, A_1, A_3\}$ in the energy and dipole moment matrices. Hamiltonian is diagonalized numerically and the numerical dipole matrix is transformed into a new basis in which the Hamiltonian is diagonal. For every step of minimization the chi squared is calculated:

$$\chi^2 = \sum_n [s(\omega_n) - m(\omega_n, \{\kappa\})]^2, \quad (35)$$

where $m(\omega_n, \{\kappa\})$ is the theoretical spectrum for a given set of $\{\kappa\}$ having the same line width and line shape as the experimental synthetic spectrum.

For the other studied endohedral species (Ne, Ar, Kr, CH_4) the experimental lines are not resolved into separate well-defined spectral lines. Therefore, the baseline-corrected experimental spectra are used in eqn. (35) instead of a synthetic spectrum $s(\omega_n)$. As for $He@C_{60}$, we use eigenstates up to $n_{max} = 18$ but the number of fitted parameters is less, $\{\kappa\} = \{V_2, V_4, A_1\}$. For atoms having more than one isotope, the Hamiltonian diagonalization and the dipole matrix calculation are done separately for each mass. Spectra of isotopes are added up using the natural abundance as a weighting factor. For $Ne@C_{60}$,

Ar@C₆₀ and Kr@C₆₀ the minimization is done simultaneously across several temperatures, assuming that the line width is temperature independent. The linewidth of the CH₄@C₆₀ absorption lines varied with temperature, so minimization is carried out at many temperatures, with linewidth for each temperature equal to the corresponding experimental THz line width. To calculate the uncertainty $\{\Delta\kappa\}$ of the fit parameters of A@C₆₀ we used the method described in [22].

2.2 Lennard-Jones two-body interaction potential

Lennard-Jones (LJ) potential 12-6 is an inter-atomic potential function which describe the interaction energy between two atoms as a function of distance between them. The LJ potential 12-6 is usually expressed as:

$$V_{LJ}(r) = 4\epsilon \left[\left(\frac{\sigma}{r_{ij}} \right)^{12} - \left(\frac{\sigma}{r_{ij}} \right)^6 \right], \quad (36)$$

where r is the distance between two atoms and ϵ denotes the depth of potential well and σ is the inter-atomic distance where $V_{LJ}(\sigma) = 0$. The r^{-12} term represents the repulsive force between the atoms at a short distance due to the overlap of electronic clouds of atoms and r^{-6} is the long-range attractive part of potential that describes the dispersion forces.

In case of Ng@C₆₀, the interaction potential of Ng is derived by off-setting the Ng atom from the geometric center of the C₆₀ by a distance r and summing the contribution of all sixty Ng-C two body interaction potentials. When the Ng atom is moved along different orientations in the C₆₀ cage the effect on the calculated potential curve is negligible over a pertinent energy range [87, Fig.S2]. The LJ potential presented in this case study is determined by moving the Ng atom toward the center of the hh bond (bond shared by two hexagons).

To model the 3D structure of C₆₀ we fixed the position of all carbon atoms to the best estimates from the neutron scattering [45] and assumed that the effect of the endohedral atom on the 3D structure is negligible. The given parameters are: $r_0 = 354.8 \pm 0.5$ pm, the distance of all carbon nuclei from the center of the cage, $h = 138 \pm 0.27$ pm, the length of the bond shared by two hexagonal C₆ rings, and $p = 145.97 \pm 0.18$ pm, the length of the bond shared by pentagonal C₅ and hexagonal C₆ ring. The LJ parameters given by Pang and Brisse in their work [38] are by a mistake off by a factor of 1000. The parameters corrected by Jiménez-Vázquez and Cross [88] are used to derive the Ng@C₆₀ LJ potentials, Table 1.

Table 1: Parameters of the Lennard-Jones 12-6 two body potential for Ng and carbon atom [88].

Ng	ϵ (kJ/mol)	σ (Å)
He	0.1554	2.971
Ne	0.3178	3.029
Ar	0.5965	3.323
Kr	0.7071	3.434

3 Experimental details

The endofullerene samples were prepared by molecular surgery method by our collaborators Richard Whitby and co-workers at the University of Southampton, United Kingdom. The IR and THz spectroscopy measurements discussed in this work were carried out at KBFI in Tallinn, Estonia. The spectrometers used were either Michelson interferometer Vertex 80v or Martin-Puplett interferometer SPS-200. In this chapter, we discuss the principles of interferometric spectroscopy, describe our spectrometers and cryostats for sample cooling and give an overview of sample preparation for the spectroscopic studies. This chapter is concluded with the section where we describe the extraction of the absorption coefficient from the temperature-dependent spectra.

3.1 Infrared spectroscopy of molecules

IR spectroscopy is an analytical technique that uses the IR region of electromagnetic radiation to probe matter. IR region of the electromagnetic spectrum can be divided roughly into far-IR (FIR) ($10\text{--}400\text{ cm}^{-1}$), mid-IR (MIR) ($400\text{--}5000\text{ cm}^{-1}$) and near-IR (NIR) ($5000\text{--}12500\text{ cm}^{-1}$). Also, THz ($1\text{ THz} = 10^{12}\text{ Hz} \approx 33\text{ cm}^{-1}$) spectral range is used as a synonym to FIR spectral range.

IR absorption spectroscopy measures the intensity of radiation transmitted through a sample. The IR radiation is absorbed whenever the frequency of radiation matches the separation between the energy levels *and* there is an electric or magnetic dipole moment oscillating at this frequency in the probed sample. Usually the electric field coupling to the electric dipole moment dominates over magnetic field coupling to the magnetic dipole moment. Thus, measurement of frequencies where the radiation is absorbed allows us to determine the separation of energy levels in the sample and the amount of absorbed radiation gives us the size of the electric dipole moment of this transition.

IR spectral range is important because it covers the rotational and vibrational frequencies of molecules. The vibrational motion is a periodic motion of atoms within a molecule, such as stretching or bending of chemical bonds, leaving the molecule center of mass intact. The rotational motion is the rotation of the entire molecule about its center of mass. The IR radiation is absorbed by the vibrational motion of the molecule only if the vibration induces electric dipole moment and by the rotational motion only if molecule has a permanent electric dipole moment. Molecules without the center of inversion are rotationally IR-active. A molecule is vibrationally IR-active if it lacks the center of inversion or if the vibration breaks the inversion symmetry. For example, H_2 is rotationally and vibrationally IR-inactive and CH_4 is rotationally IR-inactive but has two IR-active vibrations.

IR spectroscopy has also proven to be a useful tool for studying the quantum dynamics of endohedral small molecules. Confined molecules retain their rotational and vibrational degrees of freedom, as is known for X@C_{60} [12, 22, 24] and X@C_{70} [14]. In the confined environment the translational energy (center of mass kinetic energy) becomes quantized. Oscillatory motion of a charge-neutral molecule in the cavity with inversion symmetry does not interact with the electromagnetic radiation. However, when the molecule moves off-center the dipole moment is induced and this renders translational modes IR-active in C_{60} [27]. The translational energy, in the first approximation, is inversely related to the square root of the mass of the guest. Therefore, lighter molecules exhibit higher translational frequencies compared to heavier ones. For example, the translational mode of $\text{H}_2\text{@C}_{60}$ is at 180 cm^{-1} [12]. This frequency is higher relative to heavier molecules such as $\text{H}_2\text{O@C}_{60}$ (translational mode at 110 cm^{-1} [22]) and HF@C_{60} (translational mode at 80 cm^{-1} [24]). Additionally, the frequency depends, beside the mass, on the confining

potential. Larger molecules experience a tighter confining potential for the same host. At the end, the interplay of the mass and the size of the guest molecule determines the translational frequency. In this study, we take the advantage of induced dipole moment that allows us using THz spectroscopy to investigate the quantized translational motion of noble gas atoms and CH₄ molecule inside the molecular cavity of C₆₀.

3.2 Principles of FTIR spectroscopy

FTIR spectroscopy is a widely used spectroscopic technique to study rotational and vibrational spectra of molecules. It is based on the principle of interference of light beams to form an interferogram. The interferogram is a superposition of light beams of different frequencies recorded by an FTIR spectrometer as a function of the optical path difference between the beams. The Fourier transform, a mathematical function, transforms interferogram into a spectrum.

3.2.1 Michelson interferometer

FTIR spectrometers are usually based on the Michelson-type interferometer. Michelson interferometer is typically comprised of a beamsplitter (*BMS*) and two mirrors, one fixed and the other moving along an axis perpendicular to the mirror plane to create an optical path difference. The central part of the interferometer is the *BMS*, which bisects the beam in two and then recombines the beams after they are reflected back from the mirrors. The ideal *BMS* transmits and reflects 50% of incident radiation at all wavelengths of interest. The *BMS* made of a dielectric substrate is coated from one or from both sides or left uncoated. The choice of substrate, its thickness and coating layers determine the spectral range of the interferometer. A Michelson interferometer where the two arms of the interferometer form a right angle, is shown in Fig. 4.

As follows, we derive a broad-band light source interferogram as a function of optical path difference. The Michelson interferometer problem can be approached by treating light as a superposition of classical monochromatic plane waves each with frequency ω_i . To begin with we start with one component where $\omega \equiv \omega_i$ and introduce ω_i when we sum up monochromatic components of the electric field. The intensity measured by the detector is defined as the time-average of the electric field [89]:

$$I = \langle \mathbf{E} \cdot \mathbf{E} \rangle_T. \quad (37)$$

\mathbf{E} is the real part of a complex field:

$$\mathbf{E}(\mathbf{r}, t) = \text{Re}\{\mathbf{A}(\mathbf{r})e^{i\omega t}\}, \quad (38)$$

where \mathbf{A} is the complex amplitude. Using the complex conjugate of $\mathbf{A}(\mathbf{r})e^{i\omega t}$ the electric field is:

$$\mathbf{E} = \frac{1}{2}\{\mathbf{A}(\mathbf{r})e^{i\omega t} + \mathbf{A}(\mathbf{r})^*e^{-i\omega t}\}. \quad (39)$$

The complex amplitude of plane wave in the Cartesian coordinates is:

$$\mathbf{A}(\mathbf{r}) = a_1\hat{\mathbf{x}}e^{-i2\pi N_1\bar{\nu}\hat{\mathbf{k}}\cdot\mathbf{r}} + a_2\hat{\mathbf{y}}e^{-i2\pi N_2\bar{\nu}\hat{\mathbf{k}}\cdot\mathbf{r}} + a_3\hat{\mathbf{x}}e^{-i2\pi N_3\bar{\nu}\hat{\mathbf{k}}\cdot\mathbf{r}}, \quad (40)$$

where $\hat{\mathbf{k}}$ is the unit vector in the wave propagation direction, a_i ($i = 1, 2, 3$) is the real-valued amplitude, N_i is the index of refraction for the linear polarization with amplitude a_i , and $\bar{\nu}$ is the wavenumber, $\bar{\nu} = \lambda^{-1} = \nu c_0^{-1}$ where c_0 is the speed of light in vacuum and ν is frequency, $\nu = \omega(2\pi)^{-1}$, $\hat{\mathbf{x}}$, $\hat{\mathbf{y}}$ and $\hat{\mathbf{z}}$ are the unit vectors in x , y and z directions.

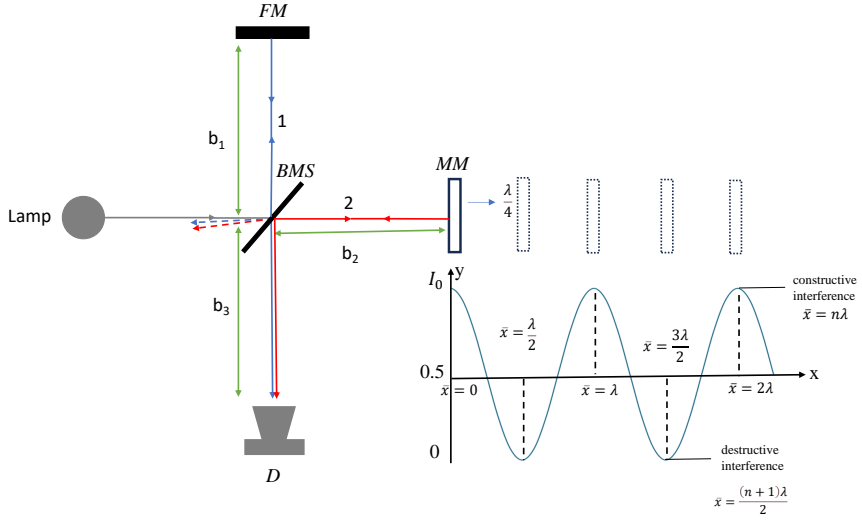


Figure 4: Schematic representation of two-beam Michelson interferometer and interferogram of monochromatic source. S - source, D - detector, SM - stationary mirror, MM - movable mirror, BMS - beamsplitter. The distance of mirrors from the BMS is b_1 and b_2 and the distance of the D from the BMS is b_3 . Here, 1 refers to the beams reflected towards SM (blue lines) and 2 refers to the beam transmitted towards MM (red lines). BMS splits the incoming beam into two components. The beams after reflecting from the mirrors are divided by the BMS second time. Two beams travel toward the detector (solid lines) and two beams return to the source (dashed lines).

We assume that light is linearly polarized along $\hat{\mathbf{z}}$. Also, the light is propagating in vacuum, thus the refractive index N is independent of the direction of propagation $\hat{\mathbf{k}}$ and is equal to 1. Hence, the beam leaving the source and reaching the BMS has electric field:

$$\mathbf{E}_0(\mathbf{z}, t) = \frac{a_0}{2} \hat{\mathbf{z}} \left[e^{i(\omega t - 2\pi \hat{\mathbf{v}} \hat{\mathbf{k}} \cdot \mathbf{r})} + e^{-i(\omega t - 2\pi \hat{\mathbf{v}} \hat{\mathbf{k}} \cdot \mathbf{r})} \right]. \quad (41)$$

The source intensity is:

$$I_0 = \langle \mathbf{E}_0 \cdot \mathbf{E}_0 \rangle_T = \frac{a_0^2}{2}. \quad (42)$$

The beam of amplitude a_0 is divided by the BMS into two components. Here, we assume that the BMS is ideal, which besides splitting the beam into equal amplitudes $a_0/\sqrt{2}$, does not change the phase of transmitted light and changes the phase of the reflected light by 90° . Mirrors, upon reflection change the phase by 180° . If you put this together, the energy sum on the detector and on the source is independent of path difference.

One component (beam 1) is reflected at 90° towards the fixed mirror FM placed at distance b_1 from BMS , while the other component (beam 2) is transmitted to the movable mirror MM , placed at a distance b_2 from the BMS . The two beams are reflected back by the mirrors and return to the BMS . The beam 1 which is previously transmitted is now reflected and vice versa for beam 2. Both the beams pass again through the BMS , where their amplitudes are further reduced by $\sqrt{2}$. From here, the beams are directed toward the detector D , placed at a distance b_3 from BMS . During this travel, beam 1 acquires the phase shift $\delta_1 = \mathbf{k}l_1 = 2\pi \hat{\mathbf{v}} l_1$ and beam 2 acquires the phase shift $\delta_2 = \mathbf{k}l_2 = 2\pi \hat{\mathbf{v}} l_2$. Here,

$l_1 = (2b_1 + b_3)$ is the total distance traveled by beam 1 from *BMS* to the *FM*, back to the *BMS*, and finally to the *D*. Similarly, $l_2 = (2b_1 + b_3)$ is the total distance travel by the beam 2 from *BMS* to the *MM*, back to the *BMS* and then to the *D*. The resultant electric field on the detector is the sum of two fields:

$$\begin{aligned}\mathbf{E}_1 &= \sum_i \frac{\hat{\mathbf{z}}}{2} [A_{1i}e^{i\omega_i t} + A_{1i}^*e^{-i\omega_i t}], \\ \mathbf{E}_2 &= \sum_j \frac{\hat{\mathbf{z}}}{2} [A_{2j}e^{i\omega_j t} + A_{2j}^*e^{-i\omega_j t}],\end{aligned}\quad (43)$$

where the sum is taken over monochromatic waves with frequency ω_i . The time-independent amplitudes are:

$$\begin{aligned}A_{1i} &= \frac{a_{0i}}{2} e^{-i(2\pi\bar{\nu}_i\hat{\mathbf{k}}\cdot\mathbf{r}-\delta_{1i})}, \\ A_{2j} &= \frac{a_{0j}}{2} e^{-i(2\pi\bar{\nu}_j\hat{\mathbf{k}}\cdot\mathbf{r}-\delta_{2j})}.\end{aligned}\quad (44)$$

From eqn. (37) the intensity at the detector of two linearly polarized waves, $\mathbf{E} = \mathbf{E}_1 + \mathbf{E}_2$, is:

$$\langle \mathbf{E} \cdot \mathbf{E} \rangle_T = \langle \mathbf{E}_1 \cdot \mathbf{E}_1 \rangle_T + \langle \mathbf{E}_2 \cdot \mathbf{E}_2 \rangle_T + 2 \langle \mathbf{E}_1 \cdot \mathbf{E}_2 \rangle_T, \quad (45)$$

where after inserting (43) and taking the time-average, the time-dependent terms where $\omega_i \neq \omega_j$ or $\omega = \pm 2\omega_i$ average to zero. This leads to intensity:

$$\langle (\mathbf{E}_1 + \mathbf{E}_2) \cdot (\mathbf{E}_1 + \mathbf{E}_2) \rangle_T = \sum_i \frac{1}{2} (A_{1i}A_{1i}^* + A_{2i}A_{2i}^* + A_{1i}A_{2i}^* + A_{1i}^*A_{2i}),$$

where by substituting the values of complex amplitudes from eqn. (44) and inserting the source value from eqn. (42), we get the output interferogram as a sum of interferograms at each frequency.

$$I(\bar{x}) = \sum_i \frac{I_0(\bar{\nu}_i)}{2} [1 + \cos(2\pi\bar{\nu}_i\bar{x})], \quad (46)$$

where $\bar{x} = l_2 - l_1$ is the optical path difference (OPD), difference in distance travelled by the light in two arms of the interferometer. The condition when both mirrors are equidistant from the *BMS*, $l_2 = l_1$, is known as zero path difference (ZPD), $\bar{x} = 0$. In the particular Michelson interferometer configuration, shown in Fig. 4, $\bar{x} = 2x$ where x is the moving mirror displacement from ZPD.

By changing \bar{x} we modulate the output intensity between zero and I_0 , Fig. 4. At ZPD both beams are in phase as they recombine at the detector. In this case, the two beams interfere constructively, and the light intensity at the detector is equal to that of the source intensity I_0 . If *MM* is displaced by $\lambda/4$, the optical path difference will become $\bar{x} = \lambda/2$. Now, both the beams are exactly half wavelength out of phase. The beams recombine destructively and the intensity at the detector is zero. A further displacement of the moving mirror by $\lambda/4$ brings the two beams back in phase with a path difference of λ . The two beams will continue to interfere constructively if the path difference is an integral multiple of their wavelength, $n\lambda$ where $n = 1, 2, 3, \dots$. On the other hand, if the path difference is half an integral multiple of wavelength i.e. $(n + 1/2)\lambda$ then the two beams will continue to interfere destructively.

In a practical IR spectrometer the light source is a heated black-body thermal radiation source which has continuous broad spectrum. The total intensity at the detector for the

continuous spectrum is [90]

$$I(\bar{x}) = \frac{1}{2} \int_0^{\infty} d\bar{v} S(\bar{v}) [1 + \cos(2\pi\bar{v}\bar{x})], \quad (47)$$

where $S(\bar{v}) = |E_s(\bar{v})|^2$ is the power spectrum of the source. We are interested in the modulated component, so the terms independent of \bar{x} can be ignored. At zero path difference, $\bar{x} = 0$, the intensity at the detector equals to the source intensity,

$$I_0 = \int_0^{\infty} S(\bar{v}) d\bar{v}. \quad (48)$$

At large path difference the intensity of the light reaching the detector is 50% of the intensity at ZPD,

$$I_{\infty} = \frac{1}{2} \int_0^{\infty} S(\bar{v}) d\bar{v}. \quad (49)$$

The normalized interferogram can be written as:

$$\gamma(\bar{x}) = \frac{I(\bar{x}) - I_{\infty}}{I_0}. \quad (50)$$

By this definition, eqn. (47) becomes:

$$\gamma(\bar{x}) = \frac{1}{2I_0} \int_0^{\infty} d\bar{v} S(\bar{v}) \cos(2\pi\bar{v}\bar{x}). \quad (51)$$

The inverse Fourier transform of the $\gamma(\bar{x})$ gives spectrum $P(\bar{v})$:

$$P(\bar{v}) = \frac{2}{\pi} \int_{-\infty}^{\infty} \gamma(\bar{x}) e^{-2i\bar{v}\bar{x}} d\bar{x}. \quad (52)$$

where is $P(\bar{v}) = \frac{S(\bar{v})}{I_0}$. Eqn. (52) is applicable if interferogram $\gamma(\bar{x})$ is symmetric about $\bar{x} = 0$ i.e $\gamma(\bar{x}) = \gamma(-\bar{x})$. In practice, the peak maximum of the interferogram is off-centered and not symmetrical around $\bar{x} = 0$. This asymmetrical nature of the interferogram is due to the multiple phase errors which come from the spectrometer such as interferogram arms length is not identical, detector response time is slow, misalignment and inaccuracies in measuring the mirror position.

In case of phase error, the Fourier transform of interferogram is:

$$\gamma(\bar{x}) = \frac{1}{2I_0} \int_0^{\infty} d\bar{v} S(\bar{v}) \cos(2\pi\bar{v}\bar{x} + \phi(\bar{v})), \quad (53)$$

where $\phi(\bar{v})$ is the phase error at frequency \bar{v} . The phase error can be corrected by multiplying the inverse Fourier transform by $e^{-2i\bar{v}\bar{x}}$

$$P(\bar{v}) e^{i\phi(\bar{v})} = \frac{2}{\pi} \int_{-\infty}^{\infty} \gamma(\bar{x}) e^{-2i\bar{v}\bar{x}} d\bar{x}. \quad (54)$$

The correction of phase errors in Fourier transform spectroscopy is discussed in detail in ref [90].

3.2.2 Martin-Puplett interferometer

The Martin-Puplett interferometer was designed by D.H. Martin and E. Puplett to probe the polarized signal, particularly in the THz region. It is similar to the Michelson interferometer. However, it differs in a few aspects: (1) the *BMS* is replaced by a wire grid polarizer, which splits the incoming beam into two orthogonal polarizations; wiregrid reflects the light polarized along the wires and transmits the light polarized perpendicular to wires, (2) the mirrors in the two arms of the interferometer are roof mirrors, which consist of two reflecting orthogonal planes. Roof mirror rotates the polarization of light by 90° upon reflecting the light polarized under $\pm 45^\circ$ relative to the mirror roof.

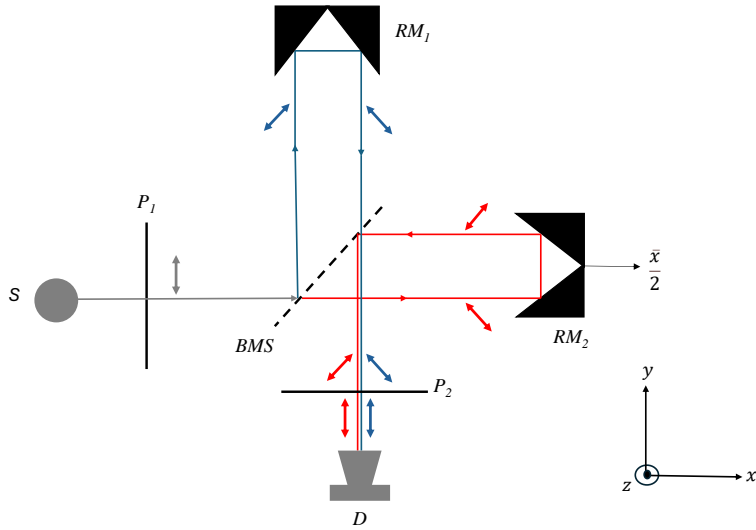


Figure 5: Martin-Puplett interferometer. *S* - source, *RM*₁ - fixed roof mirror, *RM*₂ - movable roof mirror, *P*₁ and *P*₂ - polarizers, *D* - detector, *BMS* - beamsplitter. The *z* axis is defined along the beam travel direction and the *y* axis vertical (out of the drawing plane). *P*₁ and *P*₂ polarizers transmit light with an electric field vector in the *y* direction, whereas the polarization axis of the *BMS* is rotated by 45° from the *y* axis. The beam with polarization along *y* is divided into two orthogonal polarizations by the *BMS*. The grey color shows the beam before *BMS* splits it into two halves: blue and red. The polarization component parallel to the *BMS* grid is reflected, and the polarization component perpendicular to the *BMS* is transmitted. The polarization of the two components is rotated by 90° upon reflection from the roof mirror. The previously reflected beam is transmitted through the *BMS*, while the *BMS* reflects the previously transmitted beam. The output polarizer transmits the parallel polarization from both beams and directs it towards the *D*, where they interfere.

The schematic representation of the Martin-Puplett interferometer is shown in Fig. 5. The incident beam from the source transmitted through input wire-grid polarizer *P*₁ is linearly polarized with its electric field in a vertical direction. The linearly polarized light travels towards the wire-grid beam splitter (*BMS*), which has its polarization axis under 45° relative to the incoming beam. *BMS* splits the light into two orthogonally polarized components with equal amplitudes: the component with electric field parallel to the wires is reflected and the component with electric field perpendicular to the wires is transmitted. Therefore, the polarizing wiregrid *BMS* is ideal as opposed to a dielectric *BMS* of Michelson interferometer. The reflected beam reaches the fixed roof mirror *RM*₁ while

the transmitted one reaches the movable roof mirror RM_2 . The roofs of the mirrors are at 45° relative to the direction of wires in the BMS . Hence, the two field components come back to the BMS after reflection from the roof mirrors, which rotate the polarization by 90° . Due to this polarization rotation, the BMS transmits the initially reflected component and reflects the initially transmitted component. The two components propagated towards the output wire-grid polarizer P_2 .

As the roof mirror RM_2 moves in x direction, it changes the path difference between the two orthogonally polarized components. The path difference \bar{x} creates a phase difference $\delta = 2\pi\bar{v}\bar{x}$, which depends on the wavenumber, $\bar{v} = \lambda^{-1}$. As the two beams travel different paths, the light reaches the second polarizer P_2 and will be elliptically polarized where the ellipticity is determined by the phase difference between the two perpendicular components. For a polychromatic source the light at P_2 , depending on wavelength, can exhibit all kinds of polarizations from linear to elliptical to circular. However, at ZPD ($\bar{x} = 0$) the light is linearly polarized along the polarization of the input polarizer for any \bar{v} . The light intensity after BMS is independent of the optical path difference \bar{x} . To create a modulation of intensity by \bar{x} , polarizer P_2 is placed after at the interferometer output. The output polarizer P_2 controls the intensity of the beam at the detector. At ZPD, the intensity is at the maximum if P_1 and P_2 are in parallel configuration and intensity is zero if P_1 and P_2 are orthogonal configuration. The intensity of beams after passing through P_2 is given as:

$$I = \frac{a^2}{4} [1 + \cos \delta] = \frac{I_0}{2} [1 + \cos \delta], \quad (55)$$

where a is the light amplitude and $I_0 = a^2/2$ is intensity after the P_1 .

3.3 Spectrometer Vertex 80v

The experimental results of this work were obtained using spectrometer Vertex 80v (Bruker Optics), except for $Ne@C_{60}$ where we used TeslaFIR spectrometer equipped with Martin-Puplett inteferometer SPS200. In this section, we briefly describe the main features and components of Vertex 80v.

The Vertex 80v is based on a well-aligned Ultra Scan interferometer, specifically designed for FTIR spectroscopic measurement. With the combination of optional optical components, it covers the wide spectral range from the THz region at 5 cm^{-1} to the ultraviolet (UV) region at $50\,000 \text{ cm}^{-1}$. The spectrometer allows FTIR measurements in a vacuum environment. The absence of gases in the evacuated spectrometer provides high sensitivity, stability, and reproducibility, especially in the THz region.

The spectrometer has five sections. Three of them, the interferometer, detector, and beam direction control sections, are integrated within the same optical compartment where they share the same environment, so-called optical bench. The sample compartment is completely isolated from the optical bench, where the isolation is maintained with the help of vacuum shutters (flaps). Meanwhile, the electronic compartment works in a standard atmospheric environment. The spectrometer has separate pressure sensors for the sample compartment and the optical bench, which display the current pressure within the sample/optical compartment. Hence, this design enables the evacuation of the optical bench and sample compartment separately. For example, the sample can be changed without breaking the vacuum of the optical bench.

The spectrometer is equipped with a quick lock standard transmission sample mount. The sample mount can be replaced with any other sample holder depending on the measurement. One can measure the spectrum at room temperature (RT) in this configuration.

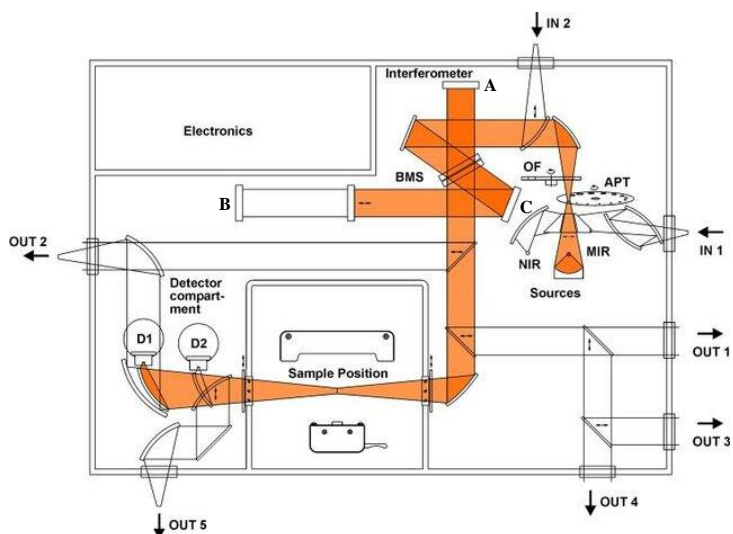


Figure 6: Optical configuration and beam path of Bruker FTIR spectrometer Vertex 80V. Interferometer consist of focusing parabolic mirrors PM, internal sources, fixed mirror A, movable B, an additional mirror C, and a detector compartment (figure is adapted from the Vertex 80v user manual.).

Before inserting the sample into the Konti cryostat to measure the low-temperature spectra, we used the sample mount to check the RT transparency of pressed pellet samples.

Fig. 6 shows layout of the Vertex 80v spectrometer and the beam path. Vertex 80v interferometer is similar to the Michelson Interferometer. It has several radiation sources which depending on the measurement range are selected using movable mirrors. An actively aligned mirror (C) is placed in front of the moving mirror to compensate for the non-linear motion of the moving mirror. To deliver broad operational range the beam guiding and focusing is done with metal-coated mirrors which reflect over broad frequency range.

The interferometer has a helium-neon (HeNe) laser that produces a monochromatic red beam of a wavelength of 632.8 nm. The mirror movement modulates the monochromatic light emitted by the laser, resulting in a sinusoidal signal. This modulated signal is used to keep track of the mirror position and to trigger data sampling.

The spectrometer features five beam exit ports and two beam input ports, which enable the connection of various optional external components, see Fig. 6. All the beam ports are vacuum-tight sealed with covers. For the MIR and NIR configurations all components are in the spectrometer. The input/exit ports are used to add Hg lamp, deuterium lamp and bolometer. The spectral range of Bruker Vertex 80v optical components is given in Fig. 7.

Hence, the spectral range from THz to the ultraviolet region is accessible with the right combination of radiation source, beamsplitter, and detector. The MIR and NIR sources are integrated within the spectrometer's optical compartment, whereas an external source can be employed for the THz spectral range. For the THz study of $A@C_{60}$, we used a water-cooled mercury arc lamp at IN 1. The BMS and detectors are removed and replaced manually by breaking the vacuum of the optical bench. Vertex 80v has, by default, two storage and one operating position for BMS inside the optical bench. The spectrometer's detector compartment is designed to position either MIR or NIR, depending on the type of measurements, for the THz study, the output port is used to focus the beam on the

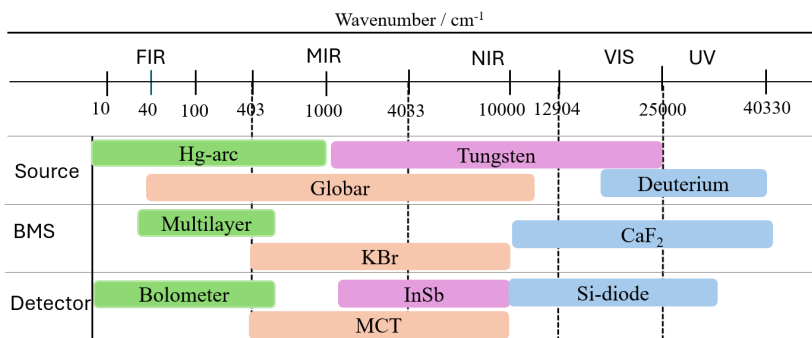


Figure 7: The combinations of light sources, BMS-s, and detectors cover far-IR (THz), mid-IR (MIR), near-IR (NIR), visible (VIS), and ultraviolet (UV) spectral ranges. **Source:** Hg-arc lamp operates within the THz region, SiC-Globar covers both THz and MIR region, SiC globar for MIR and visible range and deuterium source for ultraviolet energy range. **Beamsplitter:** Multilayer BMS operates in the THz region, potassium bromide (KBr) BMS covers MIR and NIR region, and CaF₂ BMS is designed for VIS and UV. **Detector:** 4K bolometer is used to detect THz radiation, mercury cadmium telluride (MCT) and indium antimonide (InSb) detectors are optimized for MIR and NIR spectral range, and GaP and silicon diodes are in VIS and UV range.

bolometer detector. In this case study, we used a liquid-He-cooled bolometer detector at OUT 2. The BMS-s, detectors, and sources are electronically coded so the spectrometer software can immediately identify the replaced component.

The spectrometer electronics send the digital signal to the computer. The output is processed by the OPUS software, which Bruker created to control the spectrometer. It is specifically designed for data acquisition and processing. It provides a wide range of tools for data interpretation, such as baseline correction, peak identification, and spectrum smoothing. This software controls the different components and parameters of the spectrometer. It provides a user-friendly and highly automated approach.

Transmission spectra of He@C₆₀, Ar@C₆₀, Kr@C₆₀ and CH₄@C₆₀ were recorded using the Vertex 80v spectrometer. A standard THz set of optical components covering the range from 10 to 600 cm⁻¹ while using two different cut-off filters optimized for this spectral range (Fig. 8) was used for the measurements: water cooled mercury arc lamp or electrically heated SiC (globar) radiation sources, a Ge coated 6 μm thick Mylar BMS and a liquid He cooled bolometer detector. The spectral resolution used was 0.3 cm⁻¹ or better.

3.4 Preparation of endofullerene samples for THz spectroscopy

Endofullerenes reported in this work were prepared via the synthetic route of cage opening, inserting the endohedral species, and sealing the orifice to reform pristine C₆₀, known as “molecular surgery”. The cage opening involves a series of chemical reactions that break the bonds and create an orifice in the cage. Under controlled conditions, an atom or molecule is inserted in solution in a cavity. The opening should be large enough to accommodate a single guest species and at the same time to prevent it from escaping. The cage is restored to its former state by another set of chemical reactions with an atom or molecule trapped inside. The synthesis of Ar@C₆₀ [72], Kr@C₆₀ [74] and CH₄@C₆₀ [76] were carried out by using the same multi-step chemical reactions as described in Fig 9.

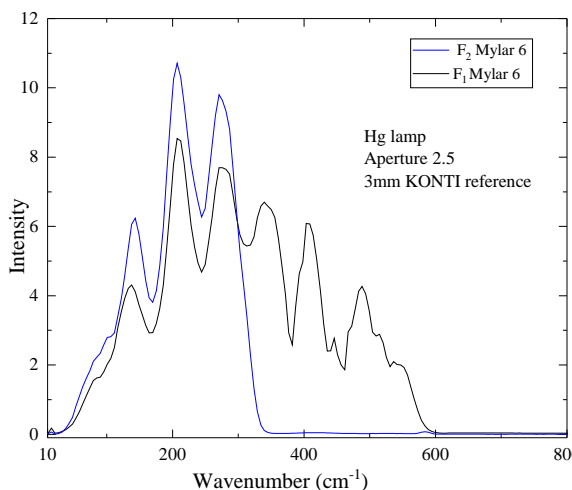


Figure 8: The bolometer signal through the 3 mm diameter reference hole in the Konti cryostat with polypropylene windows. Source is the mercury arc lamp, BMS is 6 μm Mylar and F_1 and F_2 are the 600 cm^{-1} and 300 cm^{-1} cut-off filters on the 4 K bolometer.

For $\text{He}@C_{60}$ [73] and $\text{Ne}@C_{60}$ [73], the open-cage C_{60} was filled with noble gases in the solid state. The orifice of the cage is contracted in situ upon heating to undergo the intramolecular Wittig reaction which leads to the incarceration of Ng atoms inside fullerene. $\text{He}@C_{60}$ and $\text{Ne}@C_{60}$ samples were contaminated by the traces of $\text{H}_2\text{O}@C_{60}$. To remove the impurities of $\text{H}_2\text{O}@C_{60}$ samples were purified by extensive recirculating HPLC (high-performance liquid chromatography).

All studied samples were enriched to 100% filling factor by removing empty C_{60} by recirculating HPLC. The sublimation under vacuum before spectroscopic study removed residues of any solvents.

The sublimed black powder of $A@C_{60}$ was put in brass frame and pressed under vacuum into a cylindrical pellet, see Fig. 10(b). A pressure of $P = 6000\text{Ncm}^{-2}$ was applied with the press. $\text{Ar}@C_{60}$ and $\text{Kr}@C_{60}$ samples were pressed with a piston whose end surface normal was tilted by few degrees from the piston axis. This created a wedge-shaped pellet, where the Fabry-Perot resonances were suppressed. All samples were 3 mm in diameter, but the thickness d varied based on the available amount of sample. The masses and thicknesses of studied $A@C_{60}$ pellets are given in Table 2:

Table 2: The list of samples studied, their masses, filling factor, and thickness of the pellet.

Sample	mass(mg)	Filling factor(%)	Thickness(mm)
$^3\text{He}@C_{60}$	28	97.2	2.16
$^4\text{He}@C_{60}$	21	88	1.72
$^{20}\text{Ne}@C_{60}$	21.5	99	1.61
$^{40}\text{Ar}@C_{60}$	13.2	100	1.61
$^{84}\text{Kr}@C_{60}$	12.3	100	1.00
$\text{CH}_4@C_{60}$	12.7	100	1.1

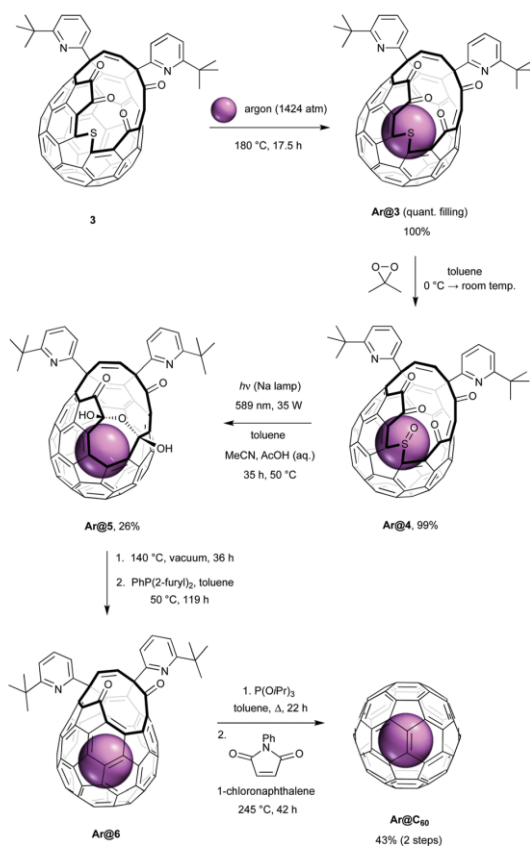


Figure 9: Organic synthesis route of Ar@C₆₀ [72].

3.5 Variable temperature THz and IR spectroscopy from 5 to 300 K using Vertex 80v

KONTI cryostat, see Fig. 10, is a continuous flow type cryostat used to cool the samples to cryogenic temperatures. Liquid helium circulates continuously through the cryostat, effectively absorbing heat from the sample and keeping it at the desired low temperature. KONTI has a bellows and motor-controlled translational stage to move the cold finger inside the cryostat up and down. It is possible with this cryostat to perform measurements from 4 to 400 K.

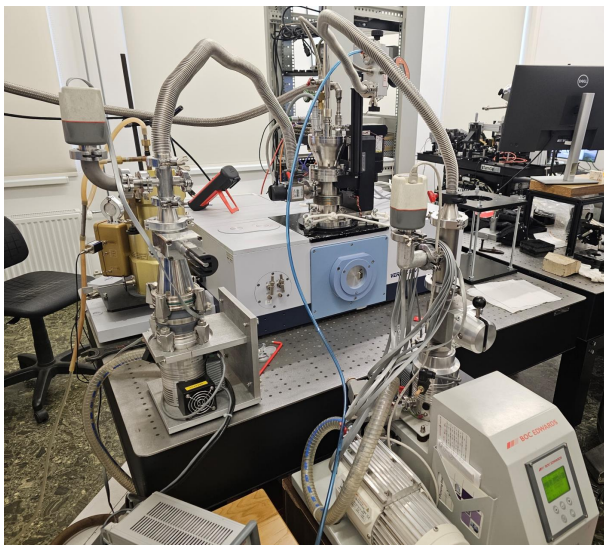
Sample cell and a 3 mm diameter empty reference hole are attached to the cold finger. The brass frame with pellet is placed inside the sample cell sealed with two polypropylene windows using indium wire. The He exchange gas added to the sample cell provides good thermal contact between the pellet and the cold finger. The sample cell is connected to stainless steel gasline which comes from the top of the cryostat. The sample cell is first evacuated and then filled with the He exchange gas to about 120 mbar of He gas at a temperature above 120 K to facilitate the heat transfer between the pellet and the cold finger. The sample cell is surrounded with two radiation shields to reduce the radiative heat load. Both radiation shields have through holes for the passing light through the cryostat.

The lower part of the cryostat is placed inside the spectrometer sample compartment

through a special cover plate what keeps the sample compartment vacuum. Cryostat vacuum is pumped continuously using a turbo pump. Helium is transferred from a He dewar to the cryostat through a CryoVac double-walled evacuated transfer line.

The THz radiation travels through the Vertex 80v Michelson interferometer to the cold-finger cryostats sample cell and finally to the detector. There is no liquid He in the optical path. To measure the radiation transmitted through the sample, the light beam enters through two windows: one on the cryostat at RT and the other on the cryostat sample cell. After passing through the sample, the beam exits the cryostat through a similar pair of windows. A heater and a thermometer are located at the cold finger. The temperature controller TIC-304 (CryoVac) regulates the cold finger heater power and the helium flow to keep the temperature at the set value. To record the transmission, the TwinLine BLV motor controller moves the cold finger up or down allowing the light to pass through the reference or sample respectively. To mount a new sample, first one has to warm up the cryostat and then replace the sample. With this cryostat we can reach 4.5 K. To study the energy structure of encapsulated species we did measurements at different temperatures from 5 to 300 K. Several reference-sample-reference measurement cycles were recorded at each temperature.

a. Vertex 80v spectrometer and cold finger cryostat



b. Brass frame with pellet



c. Cold finger



Figure 10: Low temperature optical transmission spectroscopy set-up: a. Spectrometer Vertex80v and the cold finger cryostat, b. the brass frame which contains the pellet, c. the cold finger with the sample chamber and the reference hole.

3.6 Low temperature THz spectroscopy with TeslaFIR

The Ne@C₆₀ measurements were carried out on the TeslaFIR spectrometer. It is comprised of a Martin-Puplett interferometer and liquid He (LHe) bath cryostat. Inside the cryostat are the sample chamber, the vacuum chamber with ³He cooled Si bolometer at 0.3 K, and a 17 T superconducting magnet. The sample is put inside the vacuum chamber, which is inserted into the bore of 17 T magnet. The magnetic field was not used in this

work. The schematic illustration is shown in Fig. 11. The spectral range of TeslaFIR is from 100 GHz to 6 THz. The sample temperature range is from 2.5 to 400 K.

The THz radiation produced by the Hg lamp travels through the MP interferometer, and the resulting polarized light is guided into a 16 mm light pipe, which leads to the cryostat. A black polyethylene film is placed before the first polarizer to protect the polarizer and the *BMS* from UV and visible radiation. Another black polyethylene film outside the spectrometer further filtered out the high-frequency radiation. As the beam propagates through the light pipe, it loses its state of polarization due to internal reflections. A stepper motor-controlled rotatable wire grid polarizer placed before the sample wheel redefines the light's polarization. After the polarizer, the beam passes through a rotatable sample wheel. A sample wheel has six slots, where up to six samples can be placed. It is controlled by another external stepper motor, which makes it easy to take different sample measurements without warming up the cryostat to room temperature.

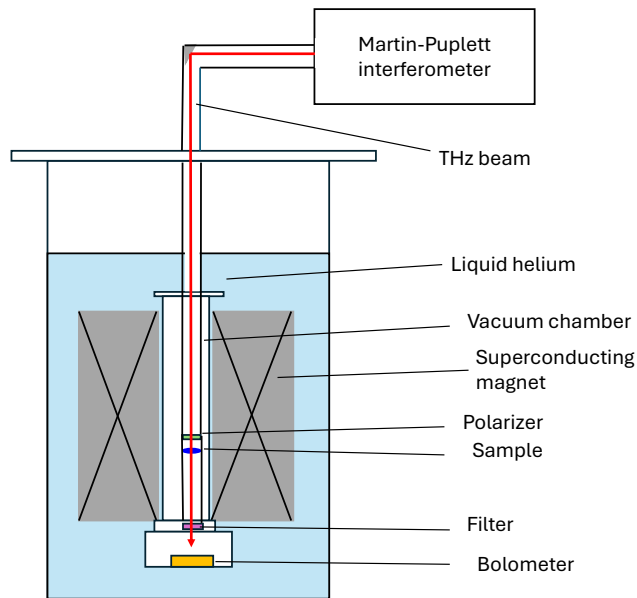


Figure 11: Schematics of TeslaFIR spectrometer. The sample cell, 0.3K bolometer and the 17 tesla magnet, immersed in the same liquid helium. The red arrow shows how the THz beam is directed from spectrometer towards the sample via light pipe.

After the sample, the beam passes through the filter wheel, equipped with eight filter slots. The filter wheel is submerged in the LHe bath to keep the filters at LHe temperature. This ensures that filters will not warm up above the LHe temperature due to the black body radiation absorbed by the filters themselves. Afterward, the light intensity is detected by a 0.3 K bolometer housed in a vacuum chamber, which separates it from LHe. The bolometer 0.3K (working temperature) is obtained using a ^3He closed-cycle cooler. In this system, the boiling temperature of ^3He is lowered to base temperature by reducing its pressure with a charcoal absorber pump, which is kept at around 5 K.

The bolometer's electrical signal is amplified by a preamplifier and converted to a digital signal with an ADC board. Using a temperature controller and an appropriate amount of heat exchange gas the sample temperature is kept at the desired value. The Ne@C₆₀

spectra are recorded at various temperatures between 5 to 100 cm^{-1} . The resolution used in this measurement was 0.3 cm^{-1} , which is less than the width of Ne@C_{60} absorption lines. The determination of absorption spectra of Ne@C_{60} and its baseline correction is discussed in the next section.

3.7 Derivation of absorption spectra from the experimental data

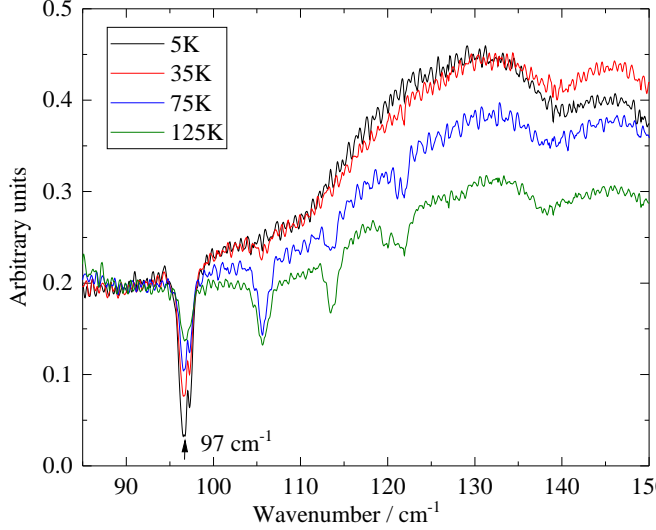


Figure 12: The raw transmission spectra, $I_p(\omega)$, of ${}^3\text{He@C}_{60}$ measured at 5K (black), 35K (red), 75K (blue), and 125K (green). There is one line present around 97 cm^{-1} at 5K shown with the arrow. As the temperature increases more lines appear in the spectrum.

The amount of radiation transmitted through the ${}^3\text{He@C}_{60}$ pellet recorded at different temperatures using the Vertex 80v setup is shown in Fig. 12. These spectra do not provide complete insight into the characteristics of the sample under study as the main features are convoluted by the characteristics of the measurement system. To overcome all the unwanted features we calculate the transmission spectra by dividing the intensity of light transmitted through the sample, $I_p(\omega)$ at frequency ω , by reference intensity $I_r(\omega)$. The transmission is given as:

$$T_{\text{tr}}(\omega) = \frac{I_p(\omega)}{I_r(\omega)}. \quad (56)$$

For the quantitative analysis the transmission spectra of $A@C_{60}$ are converted into absorption spectra. In this case study, two different approaches are used.

In the first approach, the absorption coefficient is calculated using the intensity transmitted through a 3 mm hole as a reference intensity I_r ,

$$\alpha(\omega, T) = -d^{-1} \ln \left[\frac{I_p(\omega, T)}{I_r(\omega, T)R_c} \right], \quad (57)$$

where $\alpha(\omega, T)$ is the absorption coefficient and d is the pellet thickness. R_c is the correction coefficient what takes into account reflections from the pellet surfaces and reflections and absorption by the windows of the sample cell. Usually R_c adds baseline slowly changing in frequency to $\alpha(\omega, T)$ which can be subtracted further. This approach was used for He@C_{60} , Ar@C_{60} , Kr@C_{60} and $\text{CH}_4@C_{60}$.

In the second approach the differential absorption spectra were calculated using intensity transmitted, $I_r(\omega, T_r)$, through the sample at some other temperature T_r as a reference:

$$\Delta\alpha(\omega, T) = \alpha(\omega, T) - \alpha(\omega, T_r) = -d^{-1} \ln \left[\frac{I_p(\omega, T)}{I_r(\omega, T_r)} \right]. \quad (58)$$

This is more accurate method than the first method but still additional corrections are needed because the C_{60} host may have T dependent spectral features in the spectral range of interest. In addition, spectral fringes do not subtract out completely because the index of refraction of C_{60} and the pellet thickness depend on T . This approach was used for $Ne@C_{60}$.

Additional treatment was necessary. A manual baseline correction, except for $Ne@C_{60}$, was performed using baseline correction tool of the OPUS software. With this method baseline features broader than the width of the spectral lines of interest were removed. Further processing, except for $CH_4@C_{60}$, was required for all Ng atoms. For $He@C_{60}$, the baseline of the lowest frequency peak is fitted and then subtracted for all T , see Fig. 13

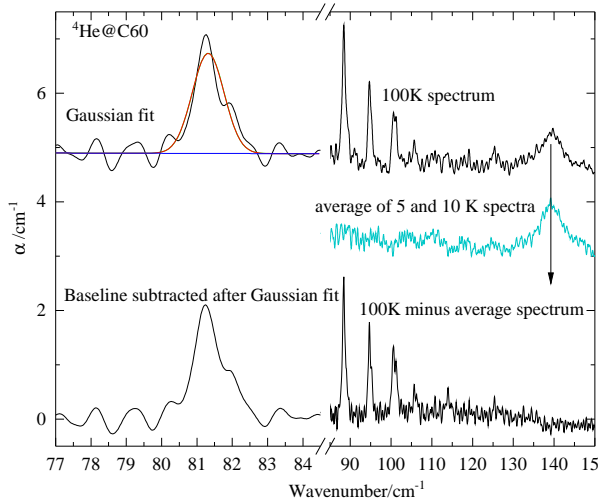


Figure 13: Correction applied to $He@C_{60}$ at 100 K, starting from top to bottom: (a) the baseline of lowest frequency peak is fitted and then subtracted. The Gaussian peak fitting is carried out using Origin software [91]. (b) The average of 5 and 15 K spectra is subtracted for baseline correction.

For the rest of peaks above the fundamental peak, the baseline is corrected by subtracting the average of 5 and 15 K spectra from the high temperature spectrum. The broad absorption at 140 cm^{-1} at 5 K does not correspond to the encapsulated He as it is independent on He atom mass, see Fig.13. This feature may originate from the absorption in the windows of the sample cell.

For the rest of the atoms, Ne, Ar and Kr, the spectral fringes were corrected by subtracting $\sin(\omega\Delta k)$ function from α , eqn. (57), or $\Delta\alpha$, eqn. (58). In case of $Ne@C_{60}$ after the subtraction of sine function, the spectrum of empty C_{60} is subtracted from the Ne spectra, as demonstrated in Fig. 14. There was no need to subtract C_{60} spectrum from $Ar@C_{60}$

and $\text{Kr}@C_{60}$ spectra as there are no visible C_{60} modes at the translational frequency of endohedral atom.

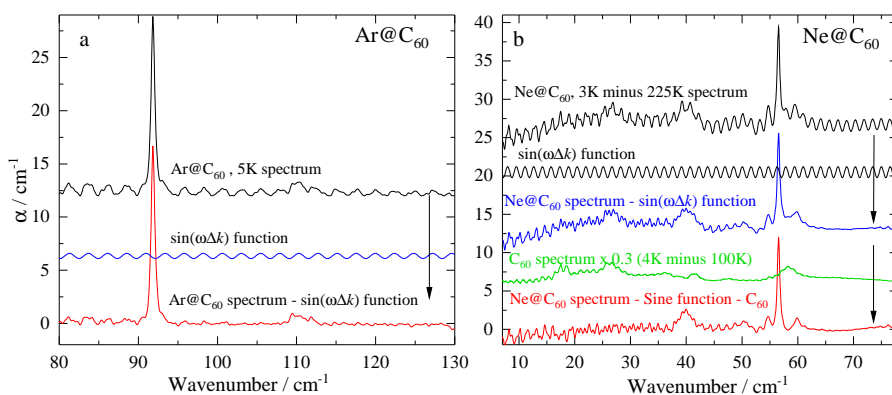


Figure 14: Correction applied to $\text{Ar}@C_{60}$ at 5K and $\text{Ne}@C_{60}$ at 3K, starting from top to bottom: (a) for $\text{Ar}@C_{60}$, sine function is subtracted from the absorption spectrum. The same correction procedure is applied to $\text{Kr}@C_{60}$. (b) For $\text{Ne}@C_{60}$ [87] firstly, the sine function is subtracted and secondly, the empty C_{60} spectrum normalized to 26 cm^{-1} line intensity is subtracted.

4 Results and discussion

In this chapter, the THz spectra of $A@C_{60}$ ($A = {}^3\text{He}, {}^4\text{He}, \text{Ne}, \text{Ar}, \text{Kr}$ and CH_4), are analyzed by studying the T -dependence of the A encapsulated in C_{60} cage. We have shown that the translational energies of A trapped inside C_{60} can be probed by THz spectroscopy despite the fact that A lacks the permanent dipole moment. The experimental results are evaluated using the spherical anharmonic oscillator model. From that model the potential energy function for the non-bonded interaction between the A and the encapsulating C_{60} cage is determined. We discuss the anharmonic behavior of each guest species with respect to their van der Waals size. The chapter concludes with a section where we compare the oscillator parameters and discuss the deviations from the spherical oscillator model. The results of $\text{Ng}@C_{60}$ are published [85, 87], while the $\text{CH}_4@C_{60}$ findings are presented here for the first time.

4.1 Noble gas atoms in C_{60}

4.1.1 He@ C_{60}

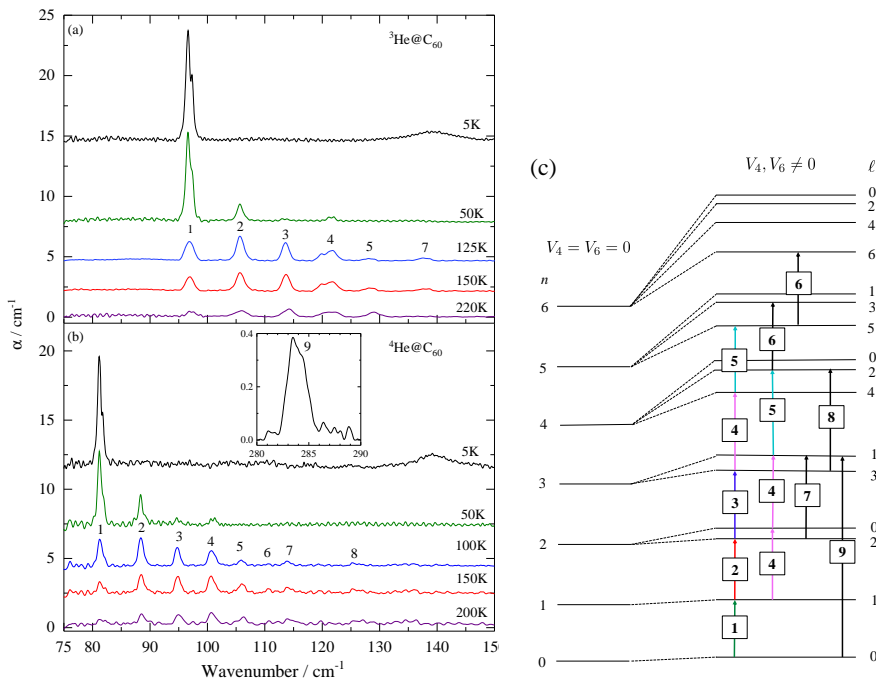


Figure 15: T dependence of THz absorption spectra of (a) ${}^3\text{He}@C_{60}$ and (b) ${}^4\text{He}@C_{60}$. The lines are numbered as shown on the energy level scheme. The inset to (b) is the ${}^4\text{He}@C_{60}$ transition from $n = 0$ to $n = 3$ at 5K. (c) Energy levels and the THz transitions of confined He isotope inside C_{60} , labeled by principle quantum number n and angular momentum quantum number ℓ . The energy levels of the harmonic oscillator are degenerate in ℓ , shown left. The anharmonic potential terms, V_4 and V_6 , lift the degeneracy of ℓ levels, shown right. The mixing of n states due anharmonicity is not show. The transitions observed between different energy levels are marked by numbers in a box. [85]

The T -dependence of the THz absorption spectra of ${}^3\text{He}@C_{60}$ and ${}^4\text{He}@C_{60}$ at different temperatures in a narrow spectral range are shown in Fig.15. Two isotopes display identi-

cal spectra with ^4He absorption lines at lower frequency than ^3He due to the heavier mass of ^4He . The high-temperature spectra reveal several well-resolved THz lines. As discussed below in Sec.4.3, the resolved multi-line spectrum is an indication that the potential energy function $V(r)$ for the encapsulated atoms is anharmonic. For ^3He , we observed seven lines at 97, 106, 114, 120, 122, 128, and 138 cm^{-1} . The line at 97 cm^{-1} shows maximum intensity at low temperatures and decreases with the increase of temperature. This spectral behavior corresponds to the transition from ground state $n = 0$ to the first excited state $n = 1$. The other lines, 106, 114, 120, 122, 128, and 138 cm^{-1} , are not present at 5 K but start to appear at elevated temperatures, thus behave as the transitions from the thermally excited levels. ^4He exhibits two transitions from its ground state: line no. 1

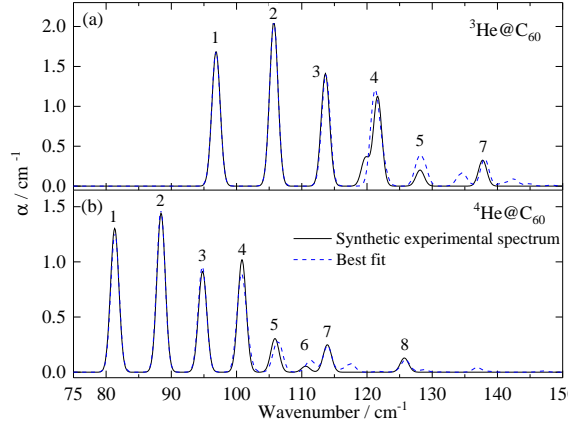


Figure 16: The synthetic experimental THz absorption spectrum of $^3\text{He}@C_{60}$ at 125 K (a) and $^4\text{He}@C_{60}$ at 100 K (b) (black solid line) and theoretical spectrum (blue dotted line) calculated with the best-fit parameters from Table 4. Figure is from Ref. [85].

at 81 cm^{-1} and line no. 9 at 284 cm^{-1} . The assignment of lines to transitions from the ground state is supported by the T -dependence of line area, inset to Fig. 17. Although in $^3\text{He}@C_{60}$ the theoretical model predicts a similar transition at 340.6 cm^{-1} (see [85, Table 4]) it was not observed by THz spectroscopy as this spectral region is obscured by C_{60} absorption. However, this transition has been observed in the INS spectrum, line e in [92]. As for ^4He , additional lines appear at elevated temperatures, at 88, 95, 101, 106, 111, 114, and 126 cm^{-1} .

We fitted the experimental synthetic spectra of two He isotopes independently by the spherical anharmonic oscillator model as described in Sec.2.1.7, and the plot is shown in Fig. 16. The best-fit parameters and their confidence limits from the fits of $^3\text{He}@C_{60}$ 125 K spectrum and $^4\text{He}@C_{60}$ 100 K spectrum are given in Table 4. The energy level diagram, along with the transition numbers, is shown in Fig. 16c. The list of experimental line frequencies and areas along with the theoretical model fit result at 125 K for $^3\text{He}@C_{60}$ and at 100 K for $^4\text{He}@C_{60}$ is given in, Ref [85, Table 4.5]

The two-component structure of line no. 1, see Fig. 23 and [85, Table 4, 5], cannot be explained by our model. The two components are separated by about 0.8 cm^{-1} for ^4He and by 0.7 cm^{-1} for ^3He . This is not possible in the approximation of spherical symmetry, rank $k = 0$. In true icosahedral symmetry of C_{60} the first non-spherical tensor in the potential function expansion has rank $k = 6$. This term splits energy levels with $\ell \geq 3$ while the transition under discussion is $\ell = 0 \rightarrow \ell = 1$ transition. The possible origin of this fine structure is discussed in the next section.

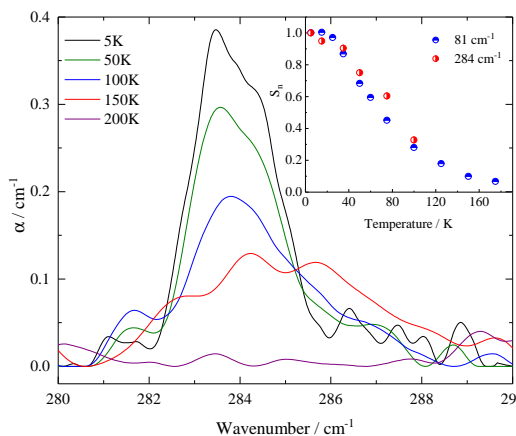


Figure 17: The absorption spectra of line no. 9 in ${}^4\text{He}@C_{60}$ at different temperatures. The inset shows the temperature-dependence of normalized THz absorption line area of line no.1 (blue dots) and line no.9 (red dots) of transition from $\ell = 0$ to $\ell = 1$ state.

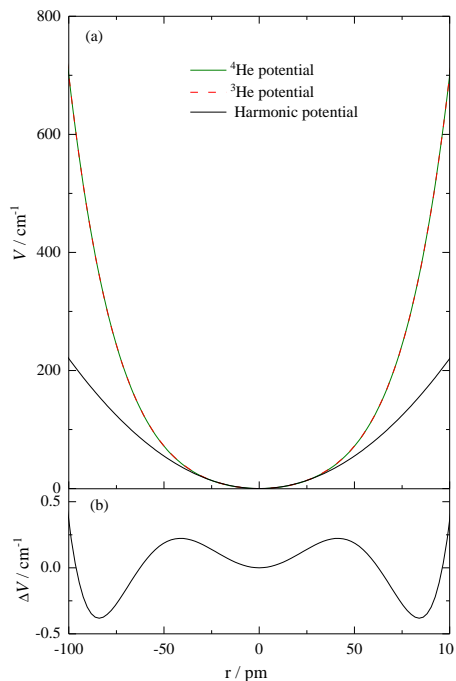


Figure 18: (a) Best fit anharmonic interaction potential $V(r)$ of ${}^3\text{He}$ (red dotted line) and ${}^4\text{He}$ (dark green solid line) calculated with the parameters from Table 4. The harmonic potential term, $V_2 r^2$ of ${}^3\text{He}$ is plotted as black line. The potential curve of ${}^3\text{He}$ superimposed on ${}^4\text{He}$ potential curve gives an indistinguishable pattern. (b) The difference of potential curves between He isotopes, $\Delta V = V_3 - V_4$ is less than $\pm 0.5 \text{ cm}^{-1}$ over the plotted energy range [85].

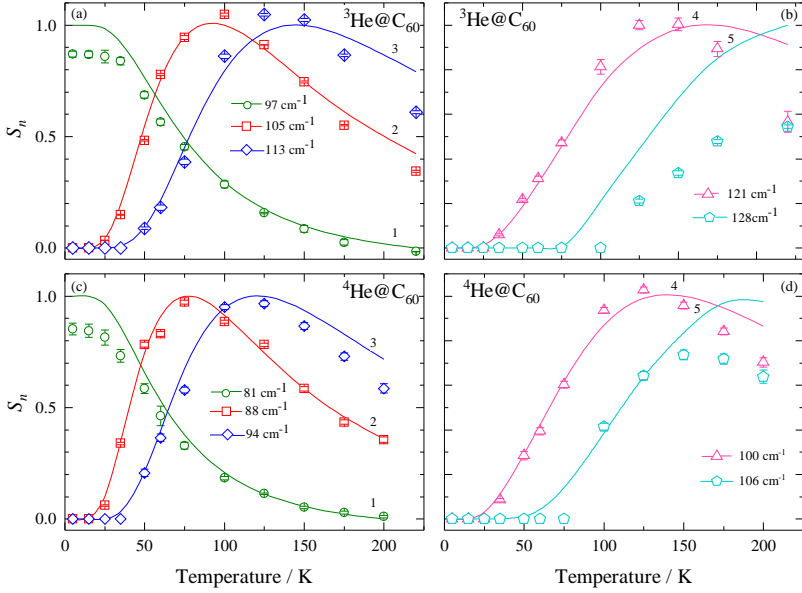


Figure 19: T -dependence of normalized THz line area S_n of $^3\text{He}@C_{60}$ (panels a and c) and $^4\text{He}@C_{60}$ (panels b and d). Symbols represent the experimental line areas with errors calculated from the Gaussian fit of the line, and the solid lines represent the theoretical line area calculated from the best parameters of Table 4. The line area is normalized to the maximum value of the theoretical area for each line. Each line is assigned numbered according to the transitions shown in Fig. 16 [85].

The line no. 9 is a transition from ground state $|n\ell\rangle = |00\rangle$ to the final state $|n\ell\rangle = |31\rangle$, see Fig. 16 panel b. It is an allowed electric dipole transition with selection rules where the angular part is changed by one unit, $\Delta\ell = +1$, but the radial part changes by three units, $\Delta n = +3$. The remaining lines are the regular transitions, $\Delta n = +1$. The induced dipole expansion term r^3 generally allows the transition from $n = 0 \rightarrow n = 3$. However, in this case, the potential function's anharmonicity mixes different n states: $n = 0$ is mixed with $n = 2$, and $n = 3$ is mixed with $n = 1$. Hence, the linear dipole term r can also induce the three-quantum transition in the presence of anharmonicity. Thus, there are two factors, the anharmonicity of the potential and the r^3 dipole moment term, that trigger the $\Delta n = +3$ transition. Fig. 18 compares the experimentally determined radial potential energy function of He isotopes in the molecular cavity of C_{60} . The best-fit potential displays an excellent correspondence between ^3He and ^4He potential curves, despite different line frequencies of two isotope. The potential curves of ^3He and ^4He differ by $\pm 0.5 \text{ cm}^{-1}$ over an energy range probed by THz spectroscopy. It is quite evident from Fig. 22 that the potential curves largely deviate from the parabolic form of a harmonic potential, and for displacement $r \geq 75 \text{ pm}$, the anharmonic terms $V_4 r^4 + V_6 r^6$ starts to dominate over the harmonic term $V_2 r^2$.

To further prove the accuracy of dipole moment parameters obtained at single temperature we compare the T dependence of experimental and theoretical line areas of $^3\text{He}@C_{60}$ and $^4\text{He}@C_{60}$ in Fig. 19. The line areas are reproduced relatively well up to 150 K except for line no. 5. The areas of lines 6, 7, and 8 could not be determined precisely from the experimental spectra because they are relatively weak and are therefore omitted. For both He isotopes, the area of line no. 1 is less than the calculated area below 50 K. This small difference between the observed and calculated T dependence could be due to the temperature dependence of the induced dipole moment not taken into account by

our model.

4.1.2 Ne@C₆₀

The THz absorption spectra of Ne@C₆₀ along with the model spectra are shown in Fig. 20. At 3 K, the strong peak at 56.6 cm⁻¹ is the translational motion peak of Ne. Based on the theoretical model calculations, we assigned this peak to the transition from the ground translational state $n = 0$ to the first excited state $n = 1$. Furthermore, the low-temperature INS study of Ne@C₆₀ shows a peak at 7 meV, being consistent with our observed Ne@C₆₀ THz peak at 56.6 cm⁻¹, and validates our assignment, see [87, Fig. 2].

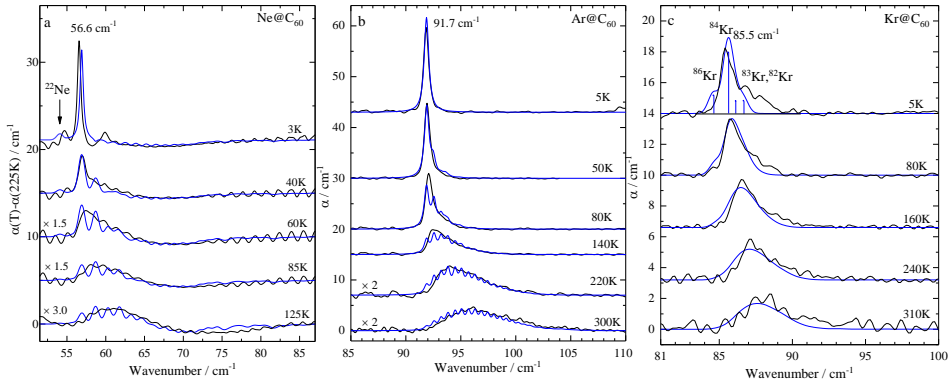


Figure 20: Temperature dependence of THz absorption spectra of Ne (a), Ar (b), and Kr (c) showing the experimental spectrum (black) and the spectrum (blue) calculated with the best fit parameters from Table 4. [85]. The fine structure of calculated spectra comes from individual transitions resolved in the Ne and Ar spectra because of the small FWHM used whereas in the Kr spectra the FWHM is larger than the separation between individual lines in the calculated spectra. (a) Differential absorption spectra of Ne@C₆₀. The line shape of the 3 K spectrum is Lorentzian with FWHM = 0.3 cm⁻¹ and Gaussian for $T \geq 40$ K with FWHM = 1.0 cm⁻¹. The intensities of 60 and 85 K spectra are multiplied by 1.5 and 125 K by three. (b) Spectra of Ar@C₆₀. The line shape is Lorentzian with FWHM = 0.5 cm⁻¹. The intensities of the 220 and 300 K spectra are multiplied by two. (c) Spectra of Kr@C₆₀. The line shape is Gaussian with FWHM = 0.8 cm⁻¹. The blue sticks in the 5 K spectrum mark the positions of four most abundant isotopes included in the fitting. Here 56.6, 97 and 85.5 cm⁻¹ in (a), (b) and (c) are the translational modes of ²⁰Ne, ⁴⁰Ar and Kr respectively. Figure is from Ref. [87].

The shape of this main peak at 3 K is well defined by a Lorentzian function with FWHM = 0.5 cm⁻¹. We noticed that the main peak exhibits unconventional low- T behavior and shows a considerable shift in peak position below 40 K, see Ref [87, Fig 1]. Also, the line gets substantially broader above 30 K and the initial Lorentzian line shape changes to a Gaussian shape with FWHM = 1.0 cm⁻¹.

The main peak of Ne@C₆₀ at 56.6 cm⁻¹ is very close to the intermolecular lattice mode of C₆₀, as can be seen in INS spectrum [87, Fig.S1]. Additionally, Bini et al. [53] observed two translational phonons at 40 and 58 cm⁻¹ detected by IR spectroscopy in crystalline C₆₀. They reported that as the temperature increased to 80 K, the translational phonon at

58 cm^{-1} broadens and shifts to a lower frequency. It is possible that low T position shift is due to the interaction between the translational motion of Ne and the C_{60} intermolecular lattice modes. Such low-temperature shift has not been observed for other studied atoms and could be explained by the energy mismatch of atom and C_{60} modes. The translational modes of other atoms (Fig. 20) are at energies higher than the high-energy cut-off of C_{60} intermolecular modes. There is a clear overlap of Ne peak at $56. \text{ cm}^{-1}$ and C_{60} mode, see Fig. 14b. Because of the line shift and broadening the spectra below 30 K are excluded from the model fit.

The high T Ne@C_{60} absorption peak continues to shift and broadens. This is caused by two factors: the thermal population of higher translational states and the anharmonicity of Ne potential energy function. The thermally excited states of Ne are well above the intermolecular modes of C_{60} and therefore the interaction between Ne and C_{60} motion is substantially reduced. The best-fit potential and dipole parameters are obtained from the simultaneous fit of $\alpha(T) - \alpha(225 \text{ K})$ where both spectra are either calculated or measured and T spanned over 30, 40, 50, 60, 70, 85, 100, 125, 150, and 175 K. The experimental and calculated spectra plotted as difference spectra, $\alpha(T) - \alpha(225 \text{ K})$ are shown in Fig. 20 and fitting parameters are presented in Table 4.

Another interesting feature of Ne@C_{60} is the existence of two more peaks, at 54.7 and 60 cm^{-1} , on the opposite sides of the main peak, see 3 K spectrum in Fig. 20. The model calculation gives the peak of ^{22}Ne (natural abundance 9.3%) on the low-frequency side of the most abundant isotope at 3 K. The low-frequency peak observed at 54.7 cm^{-1} does not precisely coincide with the calculated peak. However, the same peak was observed in Ne@C_{60} sample measured at low filling factor ($f=70\%$), see supplementary material Ref. [87, S6], indicating that the peak belongs to the Ne quantized translational mode. Thus, we attribute the 54.7 cm^{-1} absorption peak to the ^{22}Ne translational transition $n = 0 \rightarrow n = 1$. The translational peaks of the isotopes, ^{22}Ne and ^{20}Ne , slightly differ from the theoretical prediction. As discussed earlier, that ^{20}Ne peak overlaps with the high frequency cut-off of C_{60} lattice vibrations. So, it might be possible that the difference between the model and experimental ^{20}Ne and ^{22}Ne peaks arises due to the interaction of the intermolecular lattice mode of C_{60} with Ne translational peaks. The origin of the peak at 60 cm^{-1} has been discussed in Sec.4.3.

4.1.3 Ar@C₆₀

The THz absorption spectrum of Ar@C_{60} is more simple, see Fig. 20, as Ar is close to monoisotopic, with ^{40}Ar accounts for 99.6% of the natural abundance. At 5 K, a single line at about 91.7 cm^{-1} is visible in the THz absorption spectrum. This peak is well described by the Lorentzian line shape and maintains its shape and $\text{FWHM} = 0.5 \text{ cm}^{-1}$ up to 50 K. Above 50 K the peak broadens and its maximum shifts to higher frequency.

We fitted the experimental spectra at several temperatures using the Lorentzian shape with $\text{FWHM} = 0.5 \text{ cm}^{-1}$. The list of temperatures is: 5, 10, 20, 30, 40, 50, 60, 80, 100, 140, 180, 220, 250, 270 and 300 K. The spectra reproduced with the best parameter in Table 4 are plotted in Fig. 20 shows that the experimental THz line broadening and shifting are well described by the anharmonic potential model.

4.1.4 Kr@C₆₀

The THz absorption line of Kr@C_{60} is asymmetric at 5 K as opposed to Ne and Ar, Fig. 20. At the elevated T , Kr@C_{60} absorption spectra broaden further, and its maximum shifts to higher energy, exhibiting characteristics similar to Ne@C_{60} and Ar@C_{60} . We fit the experimental spectra at multiple temperatures using Gaussian lineshape with $\text{FWHM}=0.8 \text{ cm}^{-1}$

for all isotopes. The experimental spectra are fitted at the following T : 5, 40, 80, 120, 160, 220, 240, 280, 310 K. The theoretical model spectra are plotted in figure Fig. 20 with the parameters from Table 4. Note that the calculated spectra of $\text{Kr}@C_{60}$ are smooth, as compared to Ar and Ne where the calculated spectra shows oscillations because firstly, the separation between the line frequency is narrow at elevated temperatures for Kr due to minimal anharmonicity and secondly the FWHM of the individual line is larger than separation between lines for the model spectra. The asymmetric line shape at 5 K spectrum of $\text{Kr}@C_{60}$ is partially due to the isotropic distribution of Kr four most abundant isotopes: ^{82}Kr , 11.6%; ^{83}Kr , 11.5%; ^{84}Kr , 57%; ^{86}Kr 17.3% [93]. The model reproduces the THz absorption spectrum shape and predicts additional features on either side of the main ^{84}Kr line at 5 K. However, an extra absorption band on the high-frequency side of the most abundant isotope remains unaddressed, as discussed in Sec. 4.3

Our model spectra reproduce the experimental spectra of Ne, Ar and Kr quite well. However, a closer look at Fig. 20 reveals that at the higher temperatures the calculated spectra are slightly shifted to low frequency with respect to the experimental spectra. This is an indication that the potential function changes with T , not taken into account in our spherical oscillator model.

4.2 Methane inside C_{60}

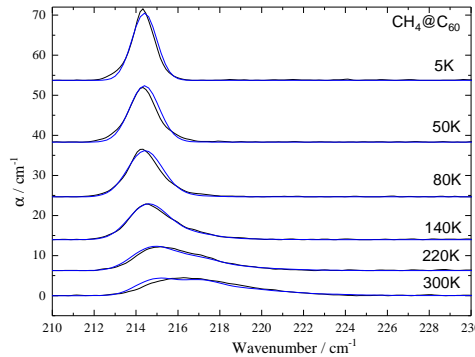


Figure 21: Temperature dependence of THz absorption spectra of $\text{CH}_4@C_{60}$; experimental spectra (black) and the calculated spectra (blue) using best fit parameters given in Table 4. Calculated spectra are plotted using Gaussian line shape and T dependent FWHM, 1.4 cm^{-1} at 5 K, 1.68 cm^{-1} at 50 K, 1.93 cm^{-1} at 80 K and 2 cm^{-1} at 140 K and above.

The temperature dependence of THz absorption spectra of $\text{CH}_4@C_{60}$ ($f = 1.0$) from 5 to 300 K is shown in Fig. 21. At 5 K, we observe one sharp peak at 214 cm^{-1} . This line is unique to $\text{CH}_4@C_{60}$ as it is not present in the THz spectra of $\text{Ng}@C_{60}$ nor C_{60} . This line does not correspond to any vibrational mode of CH_4 , because all vibrational modes of CH_4 are above 1200 cm^{-1} . It is also unlikely that the peak corresponds to the rotational transition because firstly, CH_4 does not have permanent dipole moment and secondly, it has small rotational constant, $B = 5.2\text{ cm}^{-1}$ [94]. We assign this peak to CH_4 centre of mass translational mode. At higher temperatures, $\text{CH}_4@C_{60}$ absorption peak gets weaker and broader and its maximum shifts to higher frequency, similar behavior as for the translational modes of $\text{Ne}@C_{60}$, $\text{Ar}@C_{60}$ and $\text{Kr}@C_{60}$.

To validate our experimental results, we fitted the experimental spectra with a spherical anharmonic oscillator model. The experimental spectra and the fitting process showed

that line shape is Gaussian. However, the linewidth was changing up to 80 K and could not be resolved above 80 K. We used T dependent linewidth, (T/K , FWHM/ cm^{-1}), to calculate the modelled spectra: (5, 1.4), (10, 1.4), (20, 1.52), (30, 1.55), (40, 1.6), (50, 1.68), (60, 1.77), (80, 1.93), (100, 2.0), (140, 2.0), (180, 2.0), (220, 2.0), (250, 2), (280, 2). The spectra calculated with the best-fit potential and dipole parameters from Table 4 and plotted in Fig. 21 show that the anharmonic oscillator model fits experimental THz absorption spectra very well defined. Like in Kr, the individual lines in the calculated high T spectra are not resolved because of the FWHM which is comparable or larger than the separation between the lines.

Table 3: Translational energy levels of $\text{CH}_4@C_{60}$ calculated with the parameters given in Table 4, which provide the best agreement between the THz absorption spectra and the anharmonic oscillator model. E represents the translational energy, n , and ℓ is the principal and angular momentum quantum numbers, respectively, and $|\xi|^2$ is the amplitude squared of the $|n\ell\rangle$ component of the wavefunction. The zero-point energy, 319.47cm^{-1} , has been subtracted from E .

E/cm^{-1}	n	ℓ	$ \xi ^2$
0	0	0	1
214.4	1	1	1
429.9	2	2	1
431.5	2	0	0.999
646.4	3	3	0.999
649.2	3	1	0.998
864.0	4	4	0.998
867.8	4	2	0.997
869.5	4	0	0.996
1082.7	5	5	0.998
1087.6	5	3	0.995
1090.2	5	1	0.994

4.3 Comparison of spherical oscillator parameters and deviations from the model

Table 4: Fitting parameters and uncertainties for the radial potential function $V(r) = V_2r^2 + V_4r^4 + V_6r^6$ and induced dipole function $d_{1q} = (4\pi/3)^{1/2}(A_1r + A_3r^3)Y_{1q}(\theta, \phi)$ of $A@C_{60}$. ω_{01} is the experimental frequency of the absorption line at 5K and corresponds to the transition from the ground state, $\ell = 0$ and predominantly $n = 0$, to the first excited state, $\ell = 1$ and predominantly $n = 1$. $v_{anh} = (\omega_{01} - \omega_0)/\omega_{01}$ represent the fractional contribution of the anharmonic potential to ω_{01} , where $\omega_0 = \sqrt{2V_2/m}$ is the frequency of the harmonic oscillator, d is the dipole moment for transition from the ground state $n = 0$ to first excited state $n = 1$, c_0 is the speed of light in vacuum and m is the mass of the trapped atom or molecule. The $Ng@C_{60}$ data is from [85, 87].

Parameter	${}^3\text{He}$	${}^4\text{He}$	${}^{20}\text{Ne}$	${}^{40}\text{Ar}$	${}^{40}\text{Kr}$	CH_4
$V_2 /$	0.40 ± 0.002	0.39 ± 0.006	1.58 ± 0.04	9.56 ± 0.03	17.81 ± 0.12	21.10 ± 0.04
$V_4 /$	$(0.58 \pm 0.005) \times 10^{20}$	$(0.60 \pm 0.01) \times 10^{20}$	$(2.28 \pm 0.22) \times 10^{20}$	$(8.19 \pm 0.16) \times 10^{20}$	$(13.2 \pm 1.60) \times 10^{20}$	$(11.6 \pm 0.56) \times 10^{20}$
$V_6 /$	$(4.10 \pm 0.03) \times 10^{39}$	$(3.94 \pm 0.09) \times 10^{39}$	0	0	0	0
A_1 / C	$(0.68 \pm 0.04) \times 10^{-21}$	$(1.84 \pm 0.13) \times 10^{-21}$	$(3.31 \pm 0.01) \times 10^{-21}$	$(3.30 \pm 0.21) \times 10^{-21}$	$(2.73 \pm 0.03) \times 10^{-21}$	
A_3 / Cm^{-2}	0.03 ± 0.005	0.04 ± 0.01	0	0	0	0
$\frac{\omega_{01}}{2\pi c_0} / \text{cm}^{-1}$	97.3	81.4	56.6	91.8	85.4	214.1
v_{anh}	0.29	0.29	0.085	0.018	0.007	0.014
d/D	0.016	0.017	0.019	0.020	0.014	0.017

Table 5: Translational energy of ${}^4\text{He}@C_{60}$, ${}^{20}\text{Ne}@C_{60}$, ${}^{40}\text{Ar}@C_{60}$ and ${}^{84}\text{Kr}@C_{60}$ of level $n = 5, \ell = 5$ derived from the parameters given in Table 4. E is the translational energy, n the principal quantum number, ℓ angular momentum quantum number and, $|\xi_n|^2$ the amplitude square, is the contribution of main component of the specific eigenstate.

${}^4\text{He}@C_{60}$				${}^{20}\text{Ne}@C_{60}$				${}^{40}\text{Ar}@C_{60}$				${}^{84}\text{Kr}@C_{60}$			
E/cm^{-1}	n	ℓ	$ \xi ^2$	E/cm^{-1}	n	ℓ	$ \xi ^2$	E/cm^{-1}	n	ℓ	$ \xi ^2$	E/cm^{-1}	n	ℓ	$ \xi ^2$
471.1	5	5	0.47	301.0	5	5	0.92	466.0	5	5	1.0	430.9	0	0	1.0

The model parameters which give the best fit to the observed THz spectra for $A@C_{60}$, and their uncertainties are collected in Table 4. For all cases studied here the anharmonic correction terms are positive: V_4 and V_6 are positive for He and V_4 is positive for the rest of studies species. We observed that individual transitions in the high T spectra cannot be resolved in case of Ne, Ar, Kr and CH_4 endohedral complexes whereas in case of $\text{He}@C_{60}$ the separation between the lines is much larger than the linewidth of individual lines. This indicates that the potential function for He atom is highly anharmonic, which is also consistent with the fractional anharmonicity, v_{anh} , see Table 4. Indeed, in the approximation of spherical symmetry the anharmonic terms mix the states with different n but the same ℓ . The amplitude square of the main component of the harmonic oscillator with principle quantum number n for $\text{CH}_4@C_{60}$ is given in Table 3 and for $\text{Ng}@C_{60}$ is given in Ref. [85, 87]. In the case of He, the $|\xi_n|^2$ term decreases drastically as n increases, implying the high level of anharmonicity of the potential function. For example, we have collected the $|\xi_n|^2$ values of level $n = 5, \ell = 5$ for $\text{Ng}@C_{60}$ Table 3 and $\text{CH}_4@C_{60}$ in Table 5. We see that Ne also experiences significant anharmonicity while the anharmonicity of the potential function of Kr is the smallest.

In this case study, none of the guest species has the permanent dipole moment. Instead, the off-centred A acquires dipole moment through its interaction with the C_{60} molecular cage. We list the induced dipole moments, $|\langle 0|A_1r + A_3r^3|1\rangle|$, for the transition between the ground (mostly $n = 0$ state) and the first excited (mostly $n = 1$) state, in Table 4. It can be seen that the dipole moment induced by the displacement of A is about 100 times smaller than the permanent dipole of the free H_2O molecule (1.85 D). However, inside the C_{60} the dipole moment of H_2O is reduced to $0.51 \pm 0.05\text{D}$ [22, 95] which indicates the shielding of H_2O dipole by the C_{60} cage. This provides an insight into how different encapsulated species are influenced within the constrained environment of fullerene.

In Fig. 22, we compare the experimentally determined potential energy function $V(r)$ of $\text{Ng}@C_{60}$ with the LJ potential function. As mentioned earlier, the LJ interaction potential parameters extracted from the paper of Pang and Brisse [38]. Among He, Ne, Ar and Kr, the LJ potential function for $\text{Ne}@C_{60}$ provides the closest agreement with the experimental potential. Other atoms show minor discrepancies between the experimental and the LJ potential curves. In general, although carbon electrons are delocalized over 60 carbon atoms the LJ potentials with parameters of Pang and Brisse describe the potential function very well. The steeper potential curve of Ar and Kr relative to He and Ne coincide with the larger size of these atoms and their tighter potential. Due to the multi-site nature of CH_4 , one carbon atom and four hydrogen's, we did not calculate the LJ potential function for $\text{CH}_4@C_{60}$.

In Fig. 22 we plot the experimentally derived potential of $A@C_{60}$. We observed that the potential curves of $\text{Ng}@C_{60}$ steepens with an increase in atomic size however, CH_4 besides its smaller van der Waals radius than Kr shows a slightly tighter potential curve. The ob-

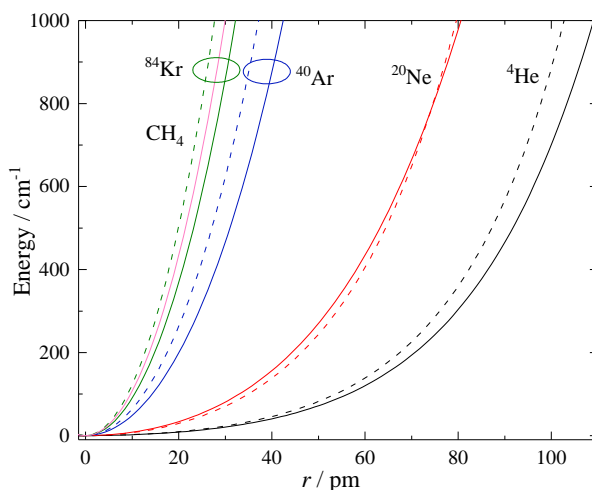


Figure 22: (a) Comparison of the experimentally derived radial potential energy function $V(r)$ and LJ potential function of Ng@C₆₀. Solid lines are the potential curves determined with parameters from Table.4 and the dotted lines are the LJ potential with parameters derived from Pang and Brisse [38]. Experimentally determined potentials are plotted for He, Ne, Ar, Kr and CH₄, while the LJ potential curves are plotted for atoms only. The experimentally determined potential curve of CH₄ (pink solid line) is between the experimental and LJ potential curves of Kr.

served discrepancy might stem from the molecular structure of CH₄. Although the van der Waals diameter is an effective parameter to construct the potential functions of atoms, it might not be adequate for the encapsulated molecules. Unlike Ng-atoms, CH₄ has vibrational degrees of freedom, which also contributes to the potential function and may also explain the tighter confinement of CH₄@C₆₀. Thus, it shows that although CH₄ is highly symmetric, it differs from atoms.

Although the spherical anharmonic oscillator model fits the THz absorption spectra of Ng@C₆₀ quite well, some discrepancies are evident. In the case of He@C₆₀, line no 1 consists of two peaks at 5 K, Fig. 23. Also, there is a 60 cm⁻¹ side peak in Ne@C₆₀ spectra and a broad side wing at about 87 cm⁻¹ in the Kr@C₆₀ spectrum, features not reproduced by the spherical oscillator model. These additional spectral features could be explained by the orientational disorder of C₆₀ molecules at low temperature, discussed in Sec.1.2. Felker et al. showed theoretically that the electric field gradient in the center of C₆₀ depends on whether the neighbouring C₆₀ are p- or h-oriented [16] This electric field gradient couples to the quadrupole moment of an encapsulated molecule and splits its rotational levels. Model explains the splitting of rotational energy levels of H₂@C₆₀ and HF@C₆₀ [16]. Although the Ng atom lacks the rotational degree of freedom and quadrupole moment, it is possible that p- and h-oriented sites have different potential function $V(r)$.

There are couple of experimental findings that reinforce this idea in the case of He@C₆₀ and Ne@C₆₀. Firstly, the temperature behavior of the He and Ne lines correspond to the transition from the ground to the excited state, see Fig. 23 and supplementary material in Ref. [87]. Secondly, the proportion of the line areas of 96.6 and 97.4 cm⁻¹ lines for ³He and the proportion of the line areas of 81.2 and 81.9 cm⁻¹ lines for ⁴He is approximately

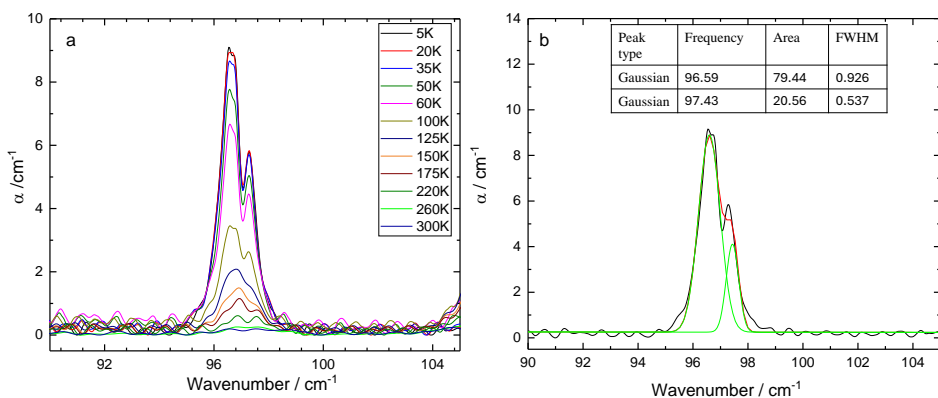


Figure 23: (a) Temperature dependence of THz absorption spectra of ${}^3\text{He}@C_{60}$ from 5 to 300 K. (b) The two-component fit to Gaussian line shape of line no. 1 of ${}^3\text{He}@C_{60}$ at 5 K. The line area of the at 96.59 cm^{-1} is approximately 80% of the total line area, and the area of the line at 97.43 cm^{-1} is about 20% of the total area.

8:2 (see Fig. 23b and Ref. [85]), which is consistent with the relative population of p- and h-orientation in C_{60} at low T . Similarly, $\text{Ne}@C_{60}$ lines at 56.6 and 60 cm^{-1} yield 8:2 ratio of the areas. The T dependence and the spectral weight of the line at 87 cm^{-1} for $\text{Kr}@C_{60}$ cannot be determined reliably due to the overlap of the main peak. We have not observed any additional peak in the case of $\text{Ar}@C_{60}$, which could be associated with the h-oriented minority site, see Fig. 20 b.

The low T spectra of $\text{Ne}@C_{60}$ and $\text{Ar}@C_{60}$ are described by a Lorentzian line with $\text{FWHM} = 0.5\text{ cm}^{-1}$. If one assumes that the width of a peak is determined by the lifetime of the excited state, then the lifetime of the first excited state would be $\tau = (2\pi\text{FWHM})^{-1}$ (FWHM in Hz), would be 10ps. For comparison, the rotational coherence time of a water molecule inside C_{60} is 15ps [96] Interestingly, the shape of the $\text{He}@C_{60}$ and $\text{CH}_4@C_{60}$ absorption line at 5 K refers to inhomogeneous broadening because it is better described by the Gaussian, with FWHM from 0.8 to 0.9 cm^{-1} for He and about 1.3 cm^{-1} for CH_4 . Thus, the homogeneous linewidth of He and CH_4 transition must be less than 0.9 cm^{-1} and 1.3 cm^{-1} respectively. Hence, the excited state lifetime of He is comparable to or longer than of Ne and Ar.

5 Summary

In $A@C_{60}$ we accomplished the goals to investigate the non-bonding interaction between $A \in \{ {}^3\text{He}, {}^4\text{He}, \text{Ne}, \text{Kr}, \text{CH}_4 \}$ and the C_{60} cage using THz spectroscopy. The temperature of the sample was changed between 4 and 300 K.

1. We showed that the noble gas atoms $\text{Ng} \in \{ {}^3\text{He}, {}^4\text{He}, \text{Ne}, \text{Ar} \text{ and } \text{Kr} \}$ encapsulated inside C_{60} acquire translation-induced dipole moment and therefore can be studied by THz spectroscopy. From the temperature dependence of measured $\text{Ng}@C_{60}$ THz absorption spectra we determined the discrete translational energy level structure of confined atoms. For the He isotopes we observed a comb of well-resolved THz absorption peaks when the higher energy translational levels became thermally populated. The high temperature THz absorption spectra of Ne, Ar, and Kr were not resolved into peaks, but instead the absorption line broadened and its maximum shifted to higher energy. The comb of resolved lines and the peak broadening and shift with temperature were explained by the anharmonicity of the confining potential function. Despite considerable mass difference between He, Ar, and Kr the translational energy is similar, about 90 cm^{-1} (2.73 THz). The interplay of atom mass and size puts the $\text{Ne}@C_{60}$ to the lower frequency side with respect to the other studied atoms, 56.6 cm^{-1} . To our knowledge, this is the first time that the quantized translational motion energy spectrum of noble gas atoms trapped inside C_{60} has been determined experimentally.
2. Using a spherical anharmonic oscillator model we derived the parameterized potential energy function for endohedral Ng atoms by fitting the THz absorption spectra. The ${}^3\text{He}$ and ${}^4\text{He}$ potential curves superimpose with high precision showing the accuracy of the model used. We observed that the potential energy increases but the anharmonicity decreases with an increase in atom mass. The parameterized potential energy function is well reproduced by the empirical Lennard-Jones 6-12 pairwise potentials between Ng and 60 carbon atoms and shows that the dominant interaction between atom and the C_{60} cage is van der Waals interaction.
3. The THz absorption spectra show that the translational mode of CH_4 is at 214 cm^{-1} . Similar to Ne, Ar and Kr the peak broadens and shifts to higher energy with increasing temperature. We fitted the temperature dependence of $\text{CH}_4@C_{60}$ THz absorption spectra with a spherical anharmonic oscillator and translational-induced dipole model. Methane shows the tightest confinement as compared to other studied Ng atoms although its van der Waal's diameter is smaller than that of Kr. The distinct potential curve of $\text{CH}_4@C_{60}$ compared to $\text{Ng}@C_{60}$ might arise from the motion of hydrogen atoms in CH_4 . To our knowledge, this is the first time that the quantized translational motion of $\text{CH}_4@C_{60}$ is studied with THz spectroscopy.

List of Figures

- 1 C_{60} molecule formed of sixty carbon atoms, gray spheres, connected by covalent bonds, sticks. The 3D structure of C_{60} is created by Diamond software [44]. 15
- 2 Rotational symmetry operations of C_{60} molecule. C_5 rotation axis connects the centres of two facing pentagons, C_3 rotation axis connects the centers of two facing hexagons and C_2 rotation axis is through the centres of the covalent bonds between the two hexagons. The green dotted line shows the σ_v mirror plane which bisect the C_{60} into two equal halves. 16
- 3 An illustration of the p and h orientation of C_{60} . C_{60} has electron-rich double bonds between two hexagons and electron-poor single bonds between hexagon and pentagon. (a) Pentagon moiety of C_{60} (red) facing electron rich double bond of neighbouring cage. (b) Hexagon moiety of C_{60} (red) facing electron rich double bond of neighbouring cage. 17
- 4 Schematic representation of two-beam Michelson interferometer and interferogram of monochromatic source. S - source, D - detector, SM - stationary mirror, MM - movable mirror, BMS - beamsplitter The distance of mirrors from the BMS is b_1 and b_2 and the distance of the D from the BMS is b_3 . Here, 1 refers to the beams reflected towards SM (blue lines) and 2 refers to the beam transmitted towards MM (red lines). BMS splits the incoming beam into two components. The beams after reflecting from the mirrors are divided by the BMS second time. Two beams travel toward the detector (solid lines) and two beams return to the source (dashed lines). 31
- 5 Martin-Puplett interferometer. S - source, RM_1 - fixed roof mirror, RM_2 - movable roof mirror, P_1 and P_2 - polarizers, D - detector, BMS - beam-splitter. The z axis is defined along the beam travel direction and the y axis vertical (out of the drawing plane). P_1 and P_2 polarizers transmit light with an electric field vector in the y direction, whereas the polarization axis of the BMS is rotated by 45° from the y axis. The beam with polarization along y is divided into two orthogonal polarizations by the BMS. The grey color shows the beam before BMS splits it into two halves: blue and red. The polarization component parallel to the BMS grid is reflected, and the polarization component perpendicular to the BMS is transmitted. The polarization of the two components is rotated by 90° upon reflection from the roof mirror. The previously reflected beam is transmitted through the BMS, while the BMS reflects the previously transmitted beam. The output polarizer transmits the parallel polarization from both beams and directs it towards the D, where they interfere. 34
- 6 Optical configuration and beampath of Bruker FTIR spectrometer Vertex 80V. Interferometer consist of focusing parabolic mirrors PM, internal sources, fixed mirror **A**, movable **B**, an additional mirror **C**, and a detector compartment (figure is adapted from the Vertex 80v user manual.). 36

7	The combinations of light sources, <i>BMS</i> -s, and detectors cover far-IR (THz), mid-IR (MIR), near-IR (NIR), visible (VIS), and ultraviolet (UV) spectral ranges. Source: Hg-arc lamp operates within the THz region, SiC-Globar covers both THz and MIR region, SiC globar for MIR, halogen lamp for NIR and visible range and deuterium source for ultraviolet energy range. Beam-splitter: Multilayer <i>BMS</i> operates in the THz region, potassium bromide (KBr) <i>BMS</i> covers MIR and NIR region, and CaF ₂ <i>BMS</i> is designed for VIS and UV. Detector: 4K bolometer is used to detect THz radiation, mercury cadmium telluride (MCT) and indium antimonide (InSb) detectors are optimized for MIR and NIR spectral range, and GaP and silicon diodes are in VIS and UV range.	37
8	The bolometer signal through the 3 mm diameter reference hole in the Konti cryostat with polypropylene windows. Source is the mercury arc lamp, <i>BMS</i> is 6 μm Mylar and F ₁ and F ₂ are the 600 cm ⁻¹ and 300 cm ⁻¹ cut-off filters on the 4 K bolometer.	38
9	Organic synthesis route of Ar@C ₆₀ [72].	39
10	Low temperature optical transmission spectroscopy set-up: a. Spectrometer Vertex80v and the cold finger cryostat, b. the brass frame which contains the pellet, c. the cold finger with the sample chamber and the reference hole.	40
11	Schematics of TeslaFIR spectrometer. The sample cell, 0.3K bolometer and the 17 tesla magnet, immersed in the same liquid helium. The red arrow shows how the THz beam is directed from spectrometer towards the sample via light pipe.	41
12	The raw transmission spectra, $I_p(\omega)$, of ³ He@C ₆₀ measured at 5 K (black), 35 K (red), 75 K (blue), and 125 K (green). There is one line present around 97 cm ⁻¹ at 5 K shown with the arrow. As the temperature increases more lines appear in the spectrum.	42
13	Correction applied to He@C ₆₀ at 100 K, starting from top to bottom: (a) the baseline of lowest frequency peak is fitted and then subtracted. The Gaussian peak fitting is carried out using Origin software [91]. (b) The average of 5 and 15 K spectra is subtracted for baseline correction.	43
14	Correction applied to Ar@C ₆₀ at 5 K and Ne@C ₆₀ at 3 K, starting from top to bottom: (a) for Ar@C ₆₀ , sine function is subtracted from the absorption spectrum. The same correction procedure is applied to Kr@C ₆₀ . (b) For Ne@C ₆₀ [87] firstly, the sine function is subtracted and secondly, the empty C ₆₀ spectrum normalized to 26 cm ⁻¹ line intensity is subtracted. ...	44
15	<i>T</i> dependence of THz absorption spectra of (a) ³ He@C ₆₀ and (b) ⁴ He@C ₆₀ . The lines are numbered as shown on the energy level scheme. The inset to (b) is the ⁴ He@C ₆₀ transition from <i>n</i> = 0 to <i>n</i> = 3 at 5 K. (c) Energy levels and the THz transitions of confined He isotope inside C ₆₀ , labeled by principle quantum number <i>n</i> and angular momentum quantum number <i>ℓ</i> . The energy levels of the harmonic oscillator are degenerate in <i>ℓ</i> , shown left. The anharmonic potential terms, <i>V</i> ₄ and <i>V</i> ₆ , lift the degeneracy of <i>ℓ</i> levels, shown right. The mixing of <i>n</i> states due anharmonicity is not show. The transitions observed between different energy levels are marked by numbers in a box. [85]	45

- 16 The synthetic experimental THz absorption spectrum of $^3\text{He@C}_{60}$ at 125 K (a) and $^4\text{He@C}_{60}$ at 100 K (b) (black solid line) and theoretical spectrum (blue dotted line) calculated with the best-fit parameters from Table 4. Figure is from Ref. [85]. 46
- 17 The absorption spectra of line no. 9 in $^4\text{He@C}_{60}$ at different temperatures. The inset shows the temperature-dependence of normalized THz absorption line area of line no.1 (blue dots) and line no.9 (red dots) of transition from $\ell = 0$ to $\ell = 1$ state..... 47
- 18 (a) Best fit anharmonic interaction potential $V(r)$ of ^3He (red dotted line) and ^4He (dark green solid line) calculated with the parameters from Table 4. The harmonic potential term, V_2r^2 of ^3He is plotted as black line. The potential curve of ^3He superimposed on ^4He potential curve gives an indistinguishable pattern. (b) The difference of potential curves between He isotopes, $\Delta V = V_3 - V_4$ is less than $\pm 0.5 \text{ cm}^{-1}$ over the plotted energy range [85]. 47
- 19 T-dependence of normalized THz line area S_n of $^3\text{He@C}_{60}$ (panels a and c) and $^4\text{He@C}_{60}$ (panels b and d). Symbols represent the experimental line areas with errors calculated from the Gaussian fit of the line, and the solid lines represent the theoretical line area calculated from the best parameters of Table 4. The line area is normalized to the maximum value of the theoretical area for each line. Each line is assigned numbered according to the transitions shown in Fig. 16 [85]. 48
- 20 Temperature dependence of THz absorption spectra of Ne (a), Ar (b), and Kr (c) showing the experimental spectrum (black) and the spectrum (blue) calculated with the best fit parameters from Table 4. [85]. The fine structure of calculated spectra comes from individual transitions resolved in the Ne and Ar spectra because of the small FWHM used whereas in the Kr spectra the FWHM is larger than the separation between individual lines in the calculated spectra. (a) Differential absorption spectra of Ne@C_{60} . The line shape of the 3 K spectrum is Lorentzian with $\text{FWHM} = 0.3 \text{ cm}^{-1}$ and Gaussian for $T \geq 40 \text{ K}$ with $\text{FWHM} = 1.0 \text{ cm}^{-1}$. The intensities of 60 and 85 K spectra are multiplied by 1.5 and 125 K by three. (b) Spectra of Ar@C_{60} . The line shape is Lorentzian with $\text{FWHM} = 0.5 \text{ cm}^{-1}$. The intensities of the 220 and 300 K spectra are multiplied by two. (c) Spectra of Kr@C_{60} . The line shape is Gaussian with $\text{FWHM} = 0.8 \text{ cm}^{-1}$. The blue sticks in the 5 K spectrum mark the positions of four most abundant isotopes included in the fitting. Here 56.6, 97 and 85.5 cm^{-1} in (a), (b) and (c) are the translational modes of ^{20}Ne , ^{40}Ar and Kr respectively. Figure is from Ref. [87]. 49
- 21 Temperature dependence of THz absorption spectra of $\text{CH}_4\text{@C}_{60}$; experimental spectra (black) and the calculated spectra (blue) using best fit parameters given in Table 4. Calculated spectra are plotted using Gaussian line shape and T dependent FWHM, 1.4 cm^{-1} at 5 K, 1.68 cm^{-1} at 50 K, 1.93 cm^{-1} at 80 K and 2 cm^{-1} at 140 K and above. 51

22	(a)	Comparison of the experimentally derived radial potential energy function $V(r)$ and LJ potential function of Ng@C ₆₀ . Solid lines are the potential curves determined with parameters from Table.4 and the dotted lines are the LJ potential with parameters derived from Pang and Brisse [38]. Experimentally determined potentials are plotted for He, Ne, Ar, Kr and CH ₄ , while the LJ potential curves are plotted for atoms only. The experimentally determined potential curve of CH ₄ (pink solid line) is between the experimental and LJ potential curves of Kr.	55
23	(a)	Temperature dependence of THz absorption spectra of ³ He@C ₆₀ from 5 to 300 K. (b) The two-component fit to Gaussian line shape of line no. 1 of ³ He@C ₆₀ at 5 K. The line area of the at 96.59 cm ⁻¹ is approximately 80% of the total line area, and the area of the line at 97.43 cm ⁻¹ is about 20% of the total area.	56

References

- [1] T. Wakahara, Y. Matsunaga, A. Katayama, Y. Maeda, M. Kako, T. Akasaka, M. Okamura, T. Kato, Y.-K. Choe, K. Kobayashi, S. Nagase, H. Huang, and M. Ata, "A comparison of the photochemical reactivity of N@C₆₀ and C₆₀: photolysis with disilirane," *Chem. Commun.*, no. 23, p. 2940, 2003.
- [2] M. Frunzi, R. J. Cross, and M. Saunders, "Effect of xenon on fullerene reactions," *J. Am. Chem. Soc.*, vol. 129, no. 43, p. 13343, 2007.
- [3] C. Cui, Z. Zhang, L. Zhu, L. Qu, Y. P. Zhang, and Y. Lan, "Reactivity and regioselectivity in diels-alder reactions of anion encapsulated fullerenes," *Phys Chem Chem Phys*, vol. 19, no. 45, pp. 30393–30401, 2017.
- [4] S. Vidal, M. Izquierdo, S. Alom, M. Garcia-Borràs, S. Filippone, S. Osuna, M. Solà, R. J. Whitby, and N. Martín, "Effect of incarcerated hf on the exohedral chemical reactivity of HF@C₆₀," *Chemical Communications*, vol. 53, no. 80, pp. 10993–10996, 2017.
- [5] M. Carravetta, O. G. Johannessen, M. H. Levitt, I. Heinmaa, R. Stern, A. Samoson, A. J. Horsewill, Y. Murata, and K. Komatsu, "Cryogenic NMR spectroscopy of endohedral hydrogen-fullerene complexes," *J. Chem. Phys.*, vol. 124, p. 104507, 2006.
- [6] M. Xu, F. Sebastianelli, Z. Bačić, R. Lawler, and N. J. Turro, "Quantum dynamics of coupled translational and rotational motions of H₂ inside C₆₀," *J. Chem. Phys.*, vol. 128, no. 1, p. 011101, 2008.
- [7] M. Xu, F. Sebastianelli, Z. Bačić, R. Lawler, and N. J. Turro, "H₂, HD, and D₂ inside C₆₀: Coupled translation-rotation eigenstates of the endohedral molecules from quantum five-dimensional calculations," *J. Chem. Phys.*, vol. 129, no. 6, p. 064313, 2008.
- [8] M. Xu, F. Sebastianelli, B. R. Gibbons, Z. Bačić, R. Lawler, and N. J. Turro, "Coupled translation-rotation eigenstates of H₂ in C₆₀ and C₇₀ on the spectroscopically optimized interaction potential: Effects of cage anisotropy on the energy level structure and assignments," *J. Chem. Phys.*, vol. 130, no. 22, p. 224306, 2009.
- [9] A. J. Horsewill, S. Rols, M. R. Johnson, Y. Murata, M. Murata, K. Komatsu, M. Carravetta, S. Mamone, M. H. Levitt, J. Y.-C. Chen, J. A. Johnson, X. Lei, and N. J. Turro, "Inelastic neutron scattering of a quantum translator-rotator encapsulated in a closed fullerene cage: Isotope effects and translation-rotation coupling in H₂@C₆₀ and HD@C₆₀," *Phys. Rev. B*, vol. 82, no. 8, p. 081410, 2010.
- [10] A. J. Horsewill, K. S. Panesar, S. Rols, J. Ollivier, M. R. Johnson, M. Carravetta, S. Mamone, M. H. Levitt, Y. Murata, K. Komatsu, J. Y.-C. Chen, J. A. Johnson, X. Lei, and N. J. Turro, "Inelastic neutron scattering investigations of the quantum molecular dynamics of a H₂ molecule entrapped inside a fullerene cage," *Phys. Rev. B*, vol. 85, p. 205440, 2012.
- [11] S. Mamone, J. Y.-C. Chen, R. Bhattacharyya, M. H. Levitt, R. G. Lawler, A. J. Horsewill, T. Rõõm, Z. Bačić, and N. J. Turro, "Theory and spectroscopy of an incarcerated quantum rotor: The infrared spectroscopy, inelastic neutron scattering and nuclear magnetic resonance of H₂@C₆₀ at cryogenic temperature," *Coord. Chem. Rev.*, vol. 255, pp. 938–948, 2011.

- [12] M. Ge, U. Nagel, D. Huvonen, T. Rom, S. Mamone, M. H. Levitt, M. Carravetta, Y. Murata, K. Komatsu, J. Y.-C. Chen, and N. J. Turro, "Interaction potential and infrared absorption of endohedral H₂ in C₆₀," *J. Chem. Phys.*, vol. 134, p. 054507, 2011.
- [13] M. Ge, U. Nagel, D. Huvonen, T. Rom, S. Mamone, M. H. Levitt, M. Carravetta, Y. Murata, K. Komatsu, X. Lei, and N. J. Turro, "Infrared spectroscopy of endohedral HD and D₂ in C₆₀," *J. Chem. Phys.*, vol. 135, no. 11, p. 114511, 2011.
- [14] T. Rom, L. Peedu, M. Ge, D. Huvonen, U. Nagel, S. Ye, M. Xu, Z. Baii, S. Mamone, M. H. Levitt, M. Carravetta, J. Chen, X. Lei, N. J. Turro, Y. Murata, and K. Komatsu, "Infrared spectroscopy of small-molecule endofullerenes," *Phil. Trans. R. Soc. A*, vol. 371, no. 1998, p. 20110631, 2013.
- [15] S. Mamone, M. Jimenez-Ruiz, M. R. Johnson, S. Rols, and A. J. Horsewill, "Experimental, theoretical and computational investigation of the inelastic neutron scattering spectrum of a homonuclear diatomic molecule in a nearly spherical trap: H₂@C₆₀," *Phys. Chem. Chem. Phys.*, vol. 18, no. 42, pp. 29369–29380, 2016.
- [16] P. M. Felker, V. Vlek, I. Hietanen, S. FitzGerald, D. Neuhauser, and Z. Baii, "Explaining the symmetry breaking observed in the endofullerenes H₂@C₆₀, HF@C₆₀, and H₂O@C₆₀," *Phys. Chem. Chem. Phys.*, vol. 19, pp. 31274–31283, 2017.
- [17] S. Mamone, M. Concistre, E. Carignani, B. Meier, A. Krachmalnicoff, O. G. Johannessen, X. Lei, Y. Li, M. Denning, M. Carravetta, K. Goh, A. J. Horsewill, R. J. Whitby, and M. H. Levitt, "Nuclear spin conversion of water inside fullerene cages detected by low-temperature nuclear magnetic resonance," *J. Chem. Phys.*, vol. 140, no. 19, p. 194306, 2014.
- [18] K. S. K. Goh, M. Jimenez-Ruiz, M. R. Johnson, S. Rols, J. Ollivier, M. S. Denning, S. Mamone, M. H. Levitt, X. Lei, Y. Li, N. J. Turro, Y. Murata, and A. J. Horsewill, "Symmetry-breaking in the endofullerene H₂O@C₆₀ revealed in the quantum dynamics of ortho and para-water: a neutron scattering investigation," *Phys. Chem. Chem. Phys.*, vol. 16, pp. 21330–21339, 2014.
- [19] P. Felker and Z. Baii, "Electric-dipole-coupled H₂O@C₆₀ dimer: Translation-rotation eigenstates from twelve-dimensional quantum calculations," *Journal of Chemical Physics*, vol. 146, 2 2017.
- [20] B. Meier, K. Kouil, C. Bengs, H. Kouilova, T. C. Barker, S. J. Elliott, S. Alom, R. J. Whitby, and M. H. Levitt, "Spin-isomer conversion of water at room temperature and quantum-rotor-induced nuclear polarization in the water-endofullerene H₂O@C₆₀," *Phys. Rev. Lett.*, vol. 120, p. 266001, Jun 2018.
- [21] E. Rashed and J. L. Dunn, "Interactions between a water molecule and C₆₀ in the endohedral fullerene H₂O@C₆₀," *Phys. Chem. Chem. Phys.*, vol. 21, pp. 3347–3359, 2019.
- [22] A. Shugai, U. Nagel, Y. Murata, Y. Li, S. Mamone, A. Krachmalnicoff, S. Alom, R. J. Whitby, M. H. Levitt, and T. Rom, "Infrared spectroscopy of an endohedral water in fullerene," *J. Chem. Phys.*, vol. 154, no. 12, p. 124311, 2021.
- [23] M. Xu, P. M. Felker, and Z. Baii, "H₂O@C₆₀ inside the fullerene C₆₀: Inelastic neutron scattering spectrum from rigorous quantum calculations," *J. Chem. Phys.*, vol. 156, no. 12, p. 124101, 2022.

- [24] A. Krachmalnicoff, R. Bounds, S. Mamone, S. Alom, M. Concistrè, B. Meier, K. Kouřil, M. E. Light, M. R. Johnson, S. Rols, A. J. Horsewill, A. Shugai, U. Nagel, T. Rößm, M. Carravetta, M. H. Levitt, and R. J. Whitby, "The dipolar endofullerene HF@C₆₀," *Nat. Chem.*, vol. 8, no. 10, pp. 953–957, 2016.
- [25] Z. Bačić, V. Vlček, D. Neuhauser, and P. M. Felker, "Effects of symmetry breaking on the translation-rotation eigenstates of H₂, HF, and H₂O inside the fullerene c₆₀," *Discuss. Faraday Soc.*, vol. 212, pp. 547–567, 2018.
- [26] E. H. T. Olthof, A. van der Avoird, and P. E. S. Wormer, "Vibration and rotation of CO in C₆₀ and predicted infrared spectrum," *J. Chem. Phys.*, vol. 104, no. 3, pp. 832–847, 1996.
- [27] S. Mamone, M. Ge, D. Hüvonen, U. Nagel, A. Danquigny, F. Cuda, M. C. Grossel, Y. Murata, K. Komatsu, M. H. Levitt, T. Rößm, and M. Carravetta, "Rotor in a cage: Infrared spectroscopy of an endohedral hydrogen-fullerene complex," *J. Chem. Phys.*, vol. 130, no. 8, p. 081103, 2009.
- [28] P. M. Felker and Z. Bačić, "Communication: Quantum six-dimensional calculations of the coupled translation-rotation eigenstates of H₂O@C₆₀," *J. Chem. Phys.*, vol. 144, no. 20, 2016.
- [29] M. Krause, M. Hulman, H. Kuzmany, T. J. S. Dennis, M. Inakuma, and H. Shinohara, "Diatomically metal encapsulates in fullerene cages: A Raman and infrared analysis of C₈₄ and Sc₂@C₈₄ with D_{2d} symmetry," *J. Chem. Phys.*, vol. 111, no. 17, pp. 7976–7984, 1999.
- [30] M. Krause, H. Kuzmany, P. Georgi, L. Dunsch, K. Vietze, and G. Seifert, "Structure and stability of endohedral fullerene Sc₃N@C₈₀: A Raman, infrared, and theoretical analysis," *J. Chem. Phys.*, vol. 115, no. 14, pp. 6596–6605, 2001.
- [31] M. Krause, M. Hulman, H. Kuzmany, O. Dubay, G. Kresse, K. Vietze, G. Seifert, C. Wang, and H. Shinohara, "Fullerene quantum gyroscope," *Phys. Rev. Lett.*, vol. 93, no. 13, p. 137403, 2004.
- [32] F. Cimpoesu, S. Ito, H. Shimotani, H. Takagi, and N. Dragoe, "Vibrational properties of noble gas endohedral fullerenes," *Phys. Chem. Chem. Phys.*, vol. 13, pp. 9609–9615, May 2011.
- [33] M. Xu, S. Ye, A. Powers, R. Lawler, N. J. Turro, and Z. Bačić, "Inelastic neutron scattering spectrum of H₂@C₆₀ and its temperature dependence decoded using rigorous quantum calculations and a new selection rule," *J. Chem. Phys.*, vol. 139, no. 6, pp. –, 2013.
- [34] B. Poirier, "Communication: The H₂@C₆₀ inelastic neutron scattering selection rule: Expanded and explained," *J. Chem. Phys.*, vol. 143, p. 101104, sep 2015.
- [35] S. Bloodworth and R. J. Whitby, "Synthesis of endohedral fullerenes by molecular surgery," *Commun. Chem.*, vol. 5, oct 2022.
- [36] J. Dawidowski, J. R. Granada, J. R. Santisteban, F. Cantargi, and L. A. R. Palomino, *Neutron Scattering Lengths and Cross Sections*, pp. 471–528. Elsevier, 2013.
- [37] A. L. R. Bug, A. Wilson, and G. A. Voth, "Nonlinear vibrational dynamics of a neon atom in fullerene C₆₀," *J. Phys. Chem.*, vol. 96, pp. 7864–7869, oct 1992.

- [38] L. Pang and F. Brisse, "Endohedral energies and translation of fullerene-noble gas clusters $G@C_n$ ($g = \text{helium, neon, argon, krypton and xenon; } n = 60 \text{ and } 70$)," *J. Phys. Chem.*, vol. 97, pp. 8562–8563, aug 1993.
- [39] B. Frecus, C. M. Buta, C. I. Oprea, A. Stroppa, M. V. Putz, and F. Cimpoesu, "Noble gas endohedral fullerenes, $Ng@C_{60}$ ($Ng=\text{Ar, Kr}$): a particular benchmark for assessing the account of non-covalent interactions by density functional theory calculations," *Theor. Chem. Acc.*, vol. 135, p. 133, apr 2016.
- [40] H. Kroto, J. Heath, S. O'Brian, R. F. Curl, and R. E. Smalley, " C_{60} : Buckminsterfullerene," *Nature*, vol. 318, pp. 162–163, 1985.
- [41] M. Garcia-Borràs, S. Osuna, J. M. Luis, M. Swart, and M. Solà, "The role of aromaticity in determining the molecular structure and reactivity of (endohedral metallo)fullerenes," *Chem. Soc. Rev.*, vol. 43, pp. 5089–5105, 2014.
- [42] J. R. Heath, S. C. O'Brien, Q. Zhang, Y. Liu, R. F. Curl, F. K. Tittel, and R. E. Smalley, "Lanthanum complexes of spheroidal carbon shells," *J. Am. Chem. Soc.*, vol. 107, no. 25, pp. 7779–7780, 1985.
- [43] R. D. Johnson, G. Meijer, and D. S. Bethune, " C_{60} has icosahedral symmetry," *J. Am. Chem. Soc.*, vol. 112, no. 24, pp. 8983–8984, 1990.
- [44] Diamond, version 3.2, Crystal Impact.
- [45] F. Leclercq, P. Damay, M. Foukani, P. Chieux, M. C. Bellissent-Funel, A. Rassat, and C. Fabre, "Precise determination of the molecular geometry in fullerene C_{60} powder: A study of the structure factor by neutron scattering in a large momentum-transfer range," *Phys. Rev. B*, vol. 48, pp. 2748–2758, jul 1993.
- [46] M. S. Dresselhaus, G. Dresselhaus, and A. Jorio, *Group Theory: Applications to the Physics of Condensed Matter*. Berlin Heidelberg: Springer-Verlag, 2008.
- [47] R. Tycko, G. Dabbagh, R. M. Fleming, R. C. Haddon, A. V. Makhija, and S. M. Zahurak, "Molecular dynamics and the phase transition in solid C_{60} ," *Phys. Rev. Lett.*, vol. 67, pp. 1886–1889, 1991.
- [48] D. A. Neumann, J. R. D. Copley, R. L. Cappelletti, W. A. Kamitakahara, R. M. Lindstrom, K. M. Creegan, D. M. Cox, W. J. Romanow, N. Coustel, J. P. McCauley, N. C. Maliszewskyj, J. E. Fischer, and A. B. Smith, "Coherent quasielastic neutron scattering study of the rotational dynamics of C_{60} in the orientationally disordered phase," *Phys. Rev. Lett.*, vol. 67, no. 27, pp. 3808–3811, 1991-12.
- [49] P. Launois, S. Ravy, and R. Moret, "Diffuse scattering and orientational correlations in solid C_{60} ," *Phys. Rev. B.*, vol. 52, no. 7, pp. 5414–5425, 1995-08.
- [50] M. e. a. Dresselhaus, *Science of Fullerenes and Carbon Nanotubes*. Academic Press, 1996.
- [51] W. I. F. David, R. M. Ibberson, J. C. Matthewman, K. Prassides, T. J. S. Dennis, J. P. Hare, R. Kroto, Harold W. nd Taylor, and D. R. M. Walton, "Crystal structure and bonding of ordered C_{60} ," *Nature*, vol. 353, pp. 147–149, 1991. paper copy.

- [52] S. Huant, J. B. Robert, G. Chouteau, P. Bernier, C. Fabre, and A. Rassat, "Lattice phonon modes in solid C_{60} studied by far-infrared spectroscopy," *Phys. Rev. Lett.*, vol. 69, no. 18, pp. 2666–2669, 1992-11.
- [53] R. Bini, P. Procacci, P. R. Salvi, and V. Schettino, "The far-infrared spectrum of crystalline fullerene C_{60} ," *J. P. Chem.*, vol. 97, pp. 10580–10584, oct 1993.
- [54] Y. Chai, T. Guo, C. Jin, R. E. Haufler, L. P. F. Chibante, J. Fure, L. Wang, J. M. Alford, and R. E. Smalley, "Fullerenes with metals inside," *J. Phys. Chem.*, vol. 95, no. 20, pp. 7564–7568, 1991-10.
- [55] T. Weiske, D. K. Böhme, J. Hrušák, W. Krätschmer, and H. Schwarz, "Endohedral cluster compounds: Inclusion of helium within C_{60}^{\oplus} and C_{70}^{\oplus} through collision experiments," *Angew. Chem. Int. Ed.*, vol. 30, pp. 884–886, jul 1991.
- [56] K. A. Caldwell, D. E. Giblin, C. S. Hsu, D. Cox, and M. L. Gross, "Endohedral complexes of fullerene radical cations," *J. Am. Chem. Soc.*, vol. 113, no. 22, pp. 8519–8521, 1991-10.
- [57] M. M. Ross and J. H. Callahan, *Formation and Characterization of $C_{60}He^+$* , pp. 1359–1364. Springer Netherlands, 1992.
- [58] T. Weiske, T. Wong, W. Krätschmer, J. K. Terlouw, and H. Schwarz, "The Neutralization of HeC_{60}^+ in the Gas Phase: Compelling Evidence for the Existence of an Endohedral Structure for $He@C_{60}$," *Angew. Chem. Int. Ed.*, vol. 31, pp. 183–185, feb 1992.
- [59] M. Saunders, R. J. Cross, H. A. Jiménez-Vázquez, R. Shimshi, and A. Khong, "Noble gas atoms inside fullerenes," *Science*, vol. 271, pp. 1693–1697, mar 1996.
- [60] M. Saunders, H. A. Jiménez-Vázquez, R. J. Cross, S. Mroczkowski, M. L. Gross, D. E. Giblin, and R. J. Poreda, "Incorporation of helium, neon, argon, krypton, and xenon into fullerenes using high pressure," *J. Am. Chem. Soc.*, vol. 116, no. 5, pp. 2193–2194, 1994.
- [61] M. S. Syamala, R. J. Cross, and M. Saunders, " ^{129}Xe NMR Spectrum of Xenon Inside C_{60} ," *J. Am. Chem. Soc.*, vol. 124, no. 21, pp. 6216–6219, 2002.
- [62] R. J. Cross, A. Khong, and M. Saunders, "Using cyanide to put noble gases inside C_{60} ," *J. Org. Chem.*, vol. 68, no. 21, pp. 8281–8283, 2003.
- [63] A. Takeda, Y. Yokoyama, S. Ito, T. Miyazaki, H. Shimotani, K. Yakigaya, T. Kakiuchi, H. Sawa, H. Takagi, K. Kitazawa, and N. Dragoie, "Superconductivity of doped $Ar@C_{60}$," *Chem. Commun.*, pp. 912–914, 2006.
- [64] T. Peres, B. Cao, W. Cui, A. Khong, R. J. Cross, M. Saunders, and C. Lifshitz, "Some new diatomic molecule containing endohedral fullerenes," *Int. J. Mass. Spectrom.*, vol. 210-211, pp. 241–247, 2001.
- [65] T. A. Murphy, T. Pawlik, A. Weidinger, M. Höhne, R. Alcalá, and J.-M. Spaeth, "Observation of atomlike nitrogen in nitrogen-implanted Solid C_{60} ," *Phys. Rev. Lett.*, vol. 77, pp. 1075–1078, aug 1996.
- [66] C. Knapp, N. Weiden, H. Kass, K.-P. Dinse, B. Pietzak, M. Waiblinger, and A. Weidinger, "Electron paramagnetic resonance study of atomic phosphorus encapsulated in [60]fullerene," *Mol. Phys.*, vol. 95, pp. 999–1004, dec 1998.

- [67] S. Ito, H. Shimotani, H. Takagi, and N. Dragoe, "On the synthesis conditions of N and N₂ endohedral fullerenes," *Fullerenes, Nanotubes and Carbon Nanostructures*, vol. 16, pp. 206–213, may 2008.
- [68] Y. Rubin, T. Jarrosson, G.-W. Wang, M. D. Bartberger, K. N. Houk, G. Schick, M. Saunders, and R. J. Cross, "Insertion of helium and molecular hydrogen through the orifice of an open fullerene," *Angew. Chem. Int. Ed.*, vol. 40, p. 1543, 2001.
- [69] Y. Murata, M. Murata, and K. Komatsu, "100% encapsulation of a hydrogen molecule into an open-cage fullerene derivative and gas-phase generation of H₂@C₆₀," *J. Am. Chem. Soc.*, vol. 125, pp. 7152–7153, 2003.
- [70] K. Komatsu, M. Murata, and Y. Murata, "Encapsulation of Molecular Hydrogen in Fullerene C₆₀ by Organic synthesis," *Science*, vol. 307, pp. 238–240, 2005.
- [71] K. Kurotobi and Y. Murata, "A Single Molecule of Water Encapsulated in Fullerene C₆₀," *Science*, vol. 333, no. 6042, pp. 613–616, 2011.
- [72] S. Bloodworth, G. Hoffman, M. C. Walkey, G. R. Bacanu, J. M. Herniman, M. H. Levitt, and R. J. Whitby, "Synthesis of Ar@C₆₀ using molecular surgery," *Chem. Commun.*, vol. 56, pp. 10521–10524, 2020.
- [73] G. Hoffman, M. C. Walkey, J. Gräsvik, G. R. Bacanu, S. Alom, S. Bloodworth, M. E. Light, M. H. Levitt, and R. J. Whitby, "A Solid-State Intramolecular Wittig Reaction Enables Efficient Synthesis of Endofullerenes Including Ne@C₆₀, ³He@C₆₀, and HD@C₆₀," *Angew. Chem. Int. Ed.*, vol. 60, no. 16, pp. 8960–8966, 2021.
- [74] G. Hoffman, G. R. Bacanu, E. S. Marsden, M. C. Walkey, M. Sabba, S. Bloodworth, G. J. Tizzard, M. H. Levitt, and R. J. Whitby, "Synthesis and ⁸³Kr NMR spectroscopy of Kr@C₆₀," *Chem. Commun.*, vol. 58, no. 80, pp. 11284–11287, 2022.
- [75] A. Krachmalnicoff, M. H. Levitt, and R. J. Whitby, "An optimised scalable synthesis of H₂O@C₆₀ and a new synthesis of H₂@C₆₀," *Chem. Commun.*, vol. 50, pp. 13037–13040, 2014.
- [76] S. Bloodworth, G. Sotinova, S. Alom, S. Vidal, G. R. Bacanu, S. J. Elliott, M. E. Light, J. M. Herniman, G. J. Langley, M. H. Levitt, and R. J. Whitby, "First synthesis and characterization of CH₄@C₆₀," *Angew. Chem. Int. Ed.*, vol. 58, pp. 5038–5043, apr 2019.
- [77] M. Murata, S. Maeda, Y. Morinaka, Y. Murata, and K. Komatsu, "Synthesis and reaction of fullerene C₇₀ encapsulating two molecules of H₂," *J. Am. Chem. Soc.*, vol. 130, no. 47, pp. 15800–15801, 2008.
- [78] V. K. Vyas, G. R. Bacanu, M. Soundararajan, E. S. Marsden, T. Jafari, A. Shugai, M. E. Light, U. Nagel, T. Rõõm, M. H. Levitt, and R. J. Whitby, "Squeezing formaldehyde into C₆₀ fullerene," *Nat Commun*, vol. 15, no. 2515, 2024.
- [79] D. J. Griffiths and D. F. Schroeter, *Introduction to Quantum Mechanics*. Cambridge University Press, aug 2018.
- [80] R. N. Zare, *Angular Momentum*. Baker lecture series, John Wiley & Sons, Inc., 1988.
- [81] D. A. Varshalovich, A. N. Moskalev, and V. K. Khersonskii, *Quantum Theory of Angular Momentum*. World Scientific, 1988.

- [82] W. H. Shaffer, "Degenerate modes of vibration and perturbations in polyatomic molecules," *Rev. Mod. Phys.*, vol. 16, pp. 245–259, Jul 1944.
- [83] D. L. Dexter, "Absorption of light by atoms in solids," *Phys. Rev.*, vol. 101, pp. 48–55, Jan 1956.
- [84] C. C. Homes, P. J. Horoyski, M. L. W. Thewalt, and B. P. Clayman, "Anomalous splitting of the $F_{1u}(\rightarrow 3F_u)$ vibrations in single-crystal C_{60} below the orientational-ordering transition," *Phys. Rev. B*, vol. 49, pp. 7052–7055, Mar 1994.
- [85] T. Jafari, G. R. Bacanu, A. Shugai, U. Nagel, M. Walkey, G. Hoffman, M. H. Levitt, R. J. Whitby, and T. Rõõm, "Terahertz spectroscopy of the helium endofullerene $He@C_{60}$," *Phys. Chem. Chem. Phys.*, vol. 24, no. 17, pp. 9943–9952, 2022.
- [86] Mathematica version 14.0, Wolfram Research Inc.
- [87] T. Jafari, A. Shugai, U. Nagel, G. R. Bacanu, M. Aouane, M. Jiménez-Ruiz, S. Rols, S. Bloodworth, M. Walkey, G. Hoffman, R. J. Whitby, M. H. Levitt, and T. Rõõm, "Ne, Ar, and Kr oscillators in the molecular cavity of fullerene C_{60} ," *J. Chem. Phys.*, vol. 158, 06 2023.
- [88] H. A. Jiménez-Vázquez and R. J. Cross, "Equilibrium constants for noble-gas fullerene compounds," *J. Chem. Phys.*, vol. 104, pp. 5589–5593, apr 1996.
- [89] M. Born and E. Wolf, *Principles of Optics*. Cambridge University Press, 1999.
- [90] C. D. Porter and D. B. Tanner, "Correction of phase errors in fourier spectroscopy," *International Journal of Infrared and Millimeter Waves*, vol. 4, no. 2, pp. 273–298, 1983-03.
- [91] Origin 2017, OriginLab Corporation.
- [92] G. R. Bacanu, T. Jafari, M. Aouane, J. Rantaharju, M. Walkey, G. Hoffman, A. Shugai, U. Nagel, M. Jiménez-Ruiz, A. J. Horsewill, S. Rols, T. Rõõm, R. J. Whitby, and M. H. Levitt, "Experimental determination of the interaction potential between a helium atom and the interior surface of a C_{60} fullerene molecule," *J. Chem. Phys.*, vol. 155, no. 14, p. 144302, 2021.
- [93] J. Meija, T. B. Coplen, M. Berglund, W. A. Brand, P. D. Bièvre, M. Gröning, N. E. Holden, J. Irrgeher, R. D. Loss, T. Walczyk, and T. Prohaska, "Isotopic compositions of the elements 2013 (IUPAC technical report)," *Pure Appl. Chem.*, vol. 88, pp. 293–306, feb 2016.
- [94] G. Herzberg, *Infrared and Raman Spectra of Polyatomic Molecules*, vol. II of *Molecular Spectra and Molecular Structure*. D. Van Nostrand Company, Inc., 1 ed., 1954.
- [95] B. Meier, S. Mamone, M. Concistrè, J. Alonso-Valdesueiro, A. Krachmalnicoff, R. J. Whitby, and M. H. Levitt, "Electrical detection of ortho-para conversion in fullerene-encapsulated water," *Nat. Commun.*, vol. 6, p. 8112, 2015.
- [96] S. S. Zhukov, V. Balos, G. Hoffman, S. Alom, M. Belyanchikov, M. Nebioglu, S. Roh, A. Pronin, G. R. Bacanu, P. Abramov, M. Wolf, M. Dressel, M. H. Levitt, R. J. Whitby, B. Gorshunov, and M. Sajadi, "Rotational coherence of encapsulated ortho and para water in fullerene- C_{60} revealed by time-domain terahertz spectroscopy," *Sci. Rep.*, vol. 10, no. 1, p. 18329, 2020.

Acknowledgements

Pursuing for this Ph.D degree has been among the most challenging yet exciting experiences of my life. However, this could not have been possible without the understanding, support, love and encouragement of those who stood by my side throughout this period.

First of all I would like to express my sincere gratitude to my son M.Qasim Abbas who accompanied me on this road when he was hardly a year old. His unlimited love, tolerance and resilience have been my constant source of motivation. Watching him grow over the past five years while pursuing my degree has truly been one of life's challenges, and I will always cherish it. I am also extremely thankful to my friends Aeman Mehmood and M. Usman Sarwar, whose kindness and support made this journey possible. They stepped in as my son's guardians rather than a babysitter. Their care, understanding, and willingness to help anytime I needed it enabled me to easily concentrate on my work, knowing my son was in good hands.

I am extremely grateful to my Supervisor Toomas Rõõm for his indispensable guidance, encouragement and constant support throughout this journey. From the beginning, he understood the difficulties of achieving academic excellence while raising a child as a single parent. His expertise, kindness, and patience played a pivotal role in framing my research and helping me grow as a researcher. I would also like to thank my co-supervisor, Urmas Nagel, for his support and valuable contribution throughout this journey. I could not imagine achieving my goal without the support of my former groupmate Anna Shugai, who was more than a friend. The scientific discoveries we made together combined with long chitchats during experiment were some of the highlights of this journey. I want to thank Laur Peedu, who always offered assistance whenever I faced technical challenges. I would also like to thank my former group members, Krill Amelin and Johan Viirok, for their support during the early stages of my research. Although I am not talkative, I am a good listener, and listening to all you guys during coffee breaks was always informative and enjoyable. I miss that time the most, and could not have asked for a better research group during the early stages of my research.

I am also thankful to my collaborators, especially Richard Whitby, for preparing the samples. My special thanks to Malcolm Levitt, who started this collaboration and led to the result of this work.

I am also thankful to my friend Ghulam Aisha who was always by my side during my rough days. I remember those difficult days when I moved to Estonia with a toddler, I was all alone and scared. During this time, I met numerous people who assisted me; I'd like to thank them all, many of whom are now friends.

I want to express my gratitude to my parents for their unconditional love, prayer, and emotional support throughout this journey. I would not have imagined coming to Estonia alone with a child if it hadn't been for my father, who stood firm, supported my decision, and handled all of the visa paperwork. I am grateful to my husband for his support, who allowed me to bring my child with me. I am deeply grateful to my lovely sisters, who were there for me whenever I was down and out; their encouragement and emotional support helped me in achieving my goal.

Last, I acknowledge financial support for this research from the Estonian Ministry of Education and Research with institutional research funding IUT23-3, the European Regional Development Fund Project No. TK134 and by EPSRC-UK, grant numbers EP/P009980/1 and EP/T004320/1.

Abstract

Quantum dynamics of noble gas atoms and methane in the molecular cavity of fullerene: terahertz spectroscopy study

For the past several years, many fascinating endohedral complexes, atoms or molecules trapped in the molecular cage of a fullerene molecule, have been prepared by the “molecular surgery” method. Endofullerene is a remarkable example of non-covalent interactions. The encapsulated atom or molecule interacts with the C_{60} wall through dispersion forces. However, it cannot escape due to the large activation energy required to penetrate through the cage. The trapped species acquire new physical properties inside the molecular cage of C_{60} . The most highlighting feature is the dominance of the quantum behavior of the encapsulated species, usually evident at cryogenic temperatures. The C_{60} cage protects the encapsulated species from interacting with the neighboring atoms or molecules, thus preventing them from condensing into liquid or solid even at very low temperatures. These endohedral complexes constitute a remarkable nano-laboratory facilitating the spectroscopic study of the nonbonding interaction potential. THz spectroscopy (0.1 – 10 THz, $3.3 - 330 \text{ cm}^{-1}$) is a powerful technique to study the dynamics of such systems.

In this study, we use two THz spectrometers at the National Institute of Chemical Physics and Biophysics in Tallinn, Estonia, to study the quantized center of mass translational movement energies of noble gas atoms and methane, encapsulated in the C_{60} cage. These samples were prepared using the molecular surgery method at the University of Southampton, UK. Our setup consists of either a Michelson-Interferometer with continuous flow cold-finger cryostat or a Martin-Puplett interferometer with a liquid He bath cryostat. The temperature-dependence of the powdered $A@C_{60}$ samples ($A = {}^3\text{He}, {}^4\text{He}, \text{Ne}, \text{Ar}, \text{Kr}, \text{CH}_4$) is studied in the energy range 50 to 240 cm^{-1} between 5 and 300 K .

The incarcerated A moves inside the cage in a spherically symmetric potential and thus its translational degrees of freedom are quantized. At the lowest temperatures the THz absorption spectra display one peak between 56 and 97 cm^{-1} for noble gas atoms and at 214 cm^{-1} for CH_4 . The absorption spectra of He isotopes exhibit well-resolved peaks at elevated temperatures, implying that the potential function of the trapped He is anharmonic. For other studied species, Ne, Ar, Kr and, CH_4 , the peaks are not resolved in the spectrum, but rather the anharmonicity causes the line broadening and shift of the line to higher frequency with an increase in temperature.

We analyzed our experimental results by fitting the THz spectra of $A@C_{60}$ to a spherical anharmonic oscillator model and translation-induced dipole moment. The dipole moment is induced by the center of mass translational motion of encapsulated A . Our spherical anharmonic oscillator model reproduces experimentally observed spectra of $A@C_{60}$ very well. We observed an excellent agreement between the potential energy function of ${}^3\text{He}$ and ${}^4\text{He}$. An additional line in the low-temperature spectrum of $\text{He}@C_{60}$ and $\text{Ne}@C_{60}$ and some extra features observed in $\text{Kr}@C_{60}$ spectrum were not explained by the model.

For $A@C_{60}$, the anharmonic part of the potential energy curve is positive, i.e. the separation of energy levels increases with an increase in energy. Helium has the most anharmonic potential and the degree of anharmonicity weakens with the increase of mass of A . The comparison of the experimentally derived potential curves of $A@C_{60}$ shows steeper potential energy curve for Ar and Kr relative to He and Ne. As expected, the confinement is tighter for a larger atom. However, the CH_4 has the steepest potential despite smaller van der Waals diameter than Kr. This could be caused by the vibrational degree of freedom of CH_4 .

We compare the experimentally derived potential parameters of noble gas atoms with

the Lennard-Jones 6-12 potential parameters taken from the work of Pang and Brisse. The empirical two-body Lennard-Jones potential shows good agreement with the experimental potential curve.

To summarize, in this work we provided experimental evidence for a nonbonding interaction between A and fullerene C_{60} in $A@C_{60}$ and determined the model that accurately describes the quantized translational motion of confined A . Our results are beneficial for the quantum chemistry calculations of non-covalent intermolecular interactions.

Kokkuvõte

Vääriskaasi aatomite ja metaani kvantdünaamika fullereeni molekulaarses õõnsuses: terahertsspektroskoopia uurimus

Viimase mitme aasta jooksul on "molekulaarse kirurgia" meetodil valmistatud palju põnevaid endoedriliisi komplekse, fullereeni molekuli molekulaarsesse puuri lõksustatud aatomeid või molekule. Endofullereen on mittekovalentsete interaktsioonide märkimisväärne näide, kus lõksustatud aatom või molekul interakteerub C_{60} seinaga dispersioonijõudude kaudu ja omandab C_{60} molekulaarses puuris uued füüsikalised omadused, kuid ei saa sealt lahkuda tänu suurele aktiveerimisenergiale, mis on vajalik läbi puuri tungimiseks. Kõige olulisem omadus on lõksustatud aatomite ja molekulide kvantkäitumise domineerimine, mis ilmneb tavaliselt madalatel temperatuuridel. C_{60} puur kaitseb kapseldatud aatomeid ja molekule naaberaatomite või molekulide mõjude eest, takistades seega nende kondenseerumist vedelikuks või tahkeks aineks isegi väga madalatel temperatuuridel. Nii moodustavad endoedriliised kompleksid tähelepanuväärse nanolabori, mis võimaldab mittesiduva interaktsioonipotentsiaali spektroskoopilist uurimist. THz spektroskoopia (0.1 – 10 THz, 3.3 – 330 cm^{-1}) on võimas tehnika selliste süsteemide dünaamika uurimiseks.

Töös kasutame Tallinnas KBFIs kahte THz spektromeetrit, et uurida C_{60} puuri kapseldatud vääriskaasi aatomite ja metaani molekuli massikeskme kvantiseeritud liikumise energiaspektreid. Uurimisobjektid valmistati Ühendkuningriigis Southamptoni üliloolis molekulaarkirurgia meetodil. Meie üks katseseade koosneb külma sõrmega läbivoolukrüostaadist, mis on ühendatud Michelsoni interferomeetriga ja teine on vedela heeliumi krüostaadiga ühendatud Martin-Puplett'i interferomeeter. Pulbristatud $A@C_{60}$ objektide ($A = {}^3He, {}^4He, Ne, Ar, Kr, CH_4$) energiaspektreite sõltuvust vahemikus 50 kuni 240 cm^{-1} uuritakse temperatuuride vahemikus 5 kuni 300 K.

Lõksustatud A liigub puuri sees sfääriliselt sümmeetrilises potentsiaalis ja seega on tema translatoorsed vabadusastmed kvantiseeritud. Madalaimatel temperatuuridel on THz neeldumisspektritel üks piigi väärtus vahemikus 56–97 cm^{-1} vääriskaasi aatomite puhul ja 214 cm^{-1} juures CH_4 puhul. He isotoopide neeldumisspektritel on kõrgematel temperatuuridel hästi eraldunud spektrijooned, mis tähendab, et He liigub anharmoonilises potentsiaalis. Teiste uuritud liikide Ne, Ar, Kr ja CH_4 jooned spektrites ei ole eraldatavad, kuna anharmoonilisus põhjustab temperatuuri tõusuga joonte laienemist ja nihkumist kõrgemale sagedusele. Analüüsime oma katsetulemusi, sobitades $A@C_{60}$ THz spektreid sfäärilise anharmoonilise ostsillaatori mudeli ja fullereeni sees toimuvast A massikeskme translatoorsest liikumisest indutseeritud dipoolmomendiga. Sfäärilise anharmoonilise ostsillaatori mudel reprodutseerib väga hästi eksperimentaalseid $A@C_{60}$ spektreid. Täheleandavalt 3He ja 4He potentsiaalse energia funktsioonide suurt sarnasust. Mudeliga ei ole võimalik selgitada täiendavat joont $He@C_{60}$ ja $Ne@C_{60}$ madala temperatuuri spektrites ning mõningaid $Kr@C_{60}$ spektris täheldatud iseärasusi.

$A@C_{60}$ puhul on potentsiaalse energia kõvera anharmooniline osa positiivne, st energiatasemete vahed suurenevad energia kasvades. Heeliumil on kõige anharmoonilisem potentsiaal ja anharmoonsuse aste väheneb A massi kasvades. Eksperimentaalselt tuletatud $A@C_{60}$ potentsiaalsete kõverate võrdlus näitab Ar ja Kr järsemat potentsiaalse energia kõverat He ja Ne suhtes. Ootuspäraselt on suurema aatomi puhul lõksustava potentsiaali kasv fullereeni kera sisepinna lähedal järsem. CH_4 korral on aga potentsiaal kõige järsem hoolimata väiksemast van der Waalsi läbimõõdust kui Kr; selle põhjuseks võib olla CH_4 vonkevabadusaste.

Võrreldes vääriskaasi aatomite eksperimentaalselt tuletatud potentsiaali parameetreid Pang'i ja Brisse tööst võetud Lennard-Jones 6-12 potentsiaalsete parameetritega, näitab

empiriiline kahe keha Lennard-Jonesi potentsiaal head vastavust eksperimentaalse potentsiaali kõveraga.

Üldistades tulmusi, esitasime eksperimentaalsed tõendid A ja fullereeni C_{60} vahelise mittesiduva interaktsiooni kohta $A@C_{60}$ -s ning määrasime kindlaks mudeli, mis kirjeldab täpselt piiratud A kvantiseeritud translatsioonilist liikumist. Meie tulemused on kasulikud mittekovalentsete molekulidevaheliste interaktsioonide kvantkeemiliste arvutuste jaoks.

Appendix 1

I

G. R. Bacanu, T. Jafari, M. Aouane, J. Rantaharju, M. Walkey, G. Hoffman, A. Shugai, U. Nagel, M. Jiménez-Ruiz, A. J. Horsewill, S. Rols, T. Rõõm, R. J. Whitby, and M. H. Levitt, "Experimental determination of the interaction potential between a helium atom and the interior surface of the C₆₀ fullerene molecule," *J. Chem. Phys.*, vol. 155, p. 144302, Oct 2021

Experimental determination of the interaction potential between a helium atom and the interior surface of a C₆₀ fullerene molecule

Cite as: J. Chem. Phys. 155, 144302 (2021); <https://doi.org/10.1063/5.0066817>

Submitted: 12 August 2021 . Accepted: 17 September 2021 . Published Online: 11 October 2021

 George Razvan Bacanu,  Tanzeeha Jafari, Mohamed Aouane, et al.



View Online



Export Citation

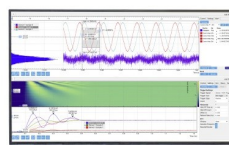


CrossMark



Challenge us.

What are your needs for
periodic signal detection?



Zurich
Instruments


Experimental determination of the interaction potential between a helium atom and the interior surface of a C₆₀ fullerene molecule

Cite as: J. Chem. Phys. 155, 144302 (2021); doi: 10.1063/5.0066817

Submitted: 12 August 2021 • Accepted: 17 September 2021 •

Published Online: 11 October 2021



George Razvan Bacanu,¹  Tanzeeha Jafari,²  Mohamed Aouane,³ Jyrki Rantaharju,¹ Mark Walkey,¹ Gabriela Hoffman,¹ Anna Shugai,²  Urmas Nagel,²  Monica Jiménez-Ruiz,³ Anthony J. Horsewill,⁴  Stéphane Rols,³  Toomas Rõõm,²  Richard J. Whitby,¹  and Malcolm H. Levitt^{1,a)} 

AFFILIATIONS

¹School of Chemistry, University of Southampton, Southampton SO17 1BJ, United Kingdom

²National Institute of Chemical Physics and Biophysics, Tallinn 12618, Estonia

³Institut Laue-Langevin, BP 156, 38042 Grenoble, France

⁴School of Physics and Astronomy, University of Nottingham, Nottingham NG7 2RD, United Kingdom

^{a)}Author to whom correspondence should be addressed: mhl@soton.ac.uk

ABSTRACT

The interactions between atoms and molecules may be described by a potential energy function of the nuclear coordinates. Nonbonded interactions between neutral atoms or molecules are dominated by repulsive forces at a short range and attractive dispersion forces at a medium range. Experimental data on the detailed interaction potentials for nonbonded interatomic and intermolecular forces are scarce. Here, we use terahertz spectroscopy and inelastic neutron scattering to determine the potential energy function for the nonbonded interaction between single He atoms and encapsulating C₆₀ fullerene cages in the helium endofullerenes ³He@C₆₀ and ⁴He@C₆₀, synthesized by molecular surgery techniques. The experimentally derived potential is compared to estimates from quantum chemistry calculations and from sums of empirical two-body potentials.

© 2021 Author(s). All article content, except where otherwise noted, is licensed under a Creative Commons Attribution (CC BY) license (<http://creativecommons.org/licenses/by/4.0/>). <https://doi.org/10.1063/5.0066817>

I. INTRODUCTION

Nonbonded intermolecular interactions determine the structure and properties of most forms of matter. The *potential energy function* specifies the dependence of the potential energy on the nuclear coordinates of the interacting moieties within the Born–Oppenheimer approximation.¹ The estimation of potential functions for nonbonded interactions remains an active research area of computational chemistry.^{2–4} *Ab initio* methods are capable of high accuracy but are usually too computationally expensive to be applied to anything but very small molecular systems. Computational techniques with good scaling properties, such as density functional theory (DFT), are generally imprecise for nonbonded interactions, unless customized adjustments are made.^{3–5} The accuracy of quantum chemistry algorithms is often assessed by seeking convergence with respect to the calculation level or number of basis functions.²

Advances in all fields of science require comparison with experiment. Unfortunately, detailed experimental data on intermolecular potential energy surfaces are scarce. Some information may be gained by comparing crystal structures and energetics with those derived from model potentials.⁶ The equilibrium structures, dissociation energies, and vibrational frequencies of intermolecular complexes and clusters may be studied in the gas phase and molecular beams.^{7–12} However, these measurements encounter difficulties with control of the local sample temperature and only provide information on potential minima and their local properties close to potential minima (unless tunneling splittings are resolved). Atomic beam diffraction may also provide information.^{13–15}

An ideal set of systems for the study of intermolecular interactions is provided by atomic and molecular endofullerenes, in which single atoms or small molecules are encapsulated in closed carbon cages.^{16–19} A range of small-molecule endofullerenes is available in macroscopic quantities through the multistep synthetic route

known as “molecular surgery,”²⁰ including $\text{H}_2@C_{60}$,¹⁸ $\text{H}_2@C_{70}$,²¹ $\text{H}_2\text{O}@C_{60}$,¹⁹ $\text{HF}@C_{60}$,²² $\text{CH}_4@C_{60}$,²³ and their isotopologues. Endofullerenes containing noble gas atoms and containing two encapsulated species may also be produced.^{21,24–30} Endofullerenes are chemically very stable, may be prepared in a pure and homogeneous solid form, and may be studied at almost any desired temperature.

At low temperatures, the translational modes (and for nonmonatomic species, the internal degrees of freedom) of the endohedral species are quantized. The quantum levels may be probed by a wide range of spectroscopic techniques,³¹ including infrared spectroscopy,^{22,32–36} pulsed terahertz spectroscopy,³⁷ nuclear magnetic resonance (NMR),^{22,29,34,38–40} and inelastic neutron scattering.^{22,34,41,42} When performed at cryogenic temperatures, these techniques reveal a rich energy level structure for the quantized modes of the encapsulated systems.^{22,32,34,41,43} The quantum structure has been studied in detail using models of the confining potential, sometimes combined with cage-induced modifications of the rotational and vibrational characteristics of the guest molecule.^{32,33,35,36,43–56}

There are two main ways to describe the interaction potential between the encapsulated species and the cage. One approach describes the interaction potential as a sum over many two-body Lennard-Jones (LJ) functions involving each endohedral atom and all 60 carbon atoms of the cage,^{44–46,49,50,52,53,55,56} sometimes introducing “additional sites” on the endohedral species as well.^{46,52,53} One disadvantage of this approach is that the summed potential has an undesirable dependence on the precise radius of the encapsulating fullerene cage. An alternative approach, which we call “model-free,” describes the interaction potential as a sum of orthogonal spatial functions.^{32,33,35,36,43,47,48} The latter approach makes no assumptions about the cage geometry and is better suited for a comparison with computational chemistry methods.

In this report, we “go back to basics” by studying the simplest atomic endofullerene, $\text{He}@C_{60}$, consisting of C_{60} fullerene cages, each encapsulating a single helium atom [Fig. 1(a)]. Terahertz and neutron scattering data are acquired and fitted by a simple quantum mechanical model consisting of a particle confined by a three-dimensional potential well. This allows us to define a “model-free” atom–fullerene potential with no assumptions about whether it may be expressed as the sum of many two-body interactions.

Although $\text{He}@C_{60}$ was first made in trace amounts by gas phase methods,^{16,17,57} molecular surgery techniques now provide both

isotopologues $^3\text{He}@C_{60}$ and $^4\text{He}@C_{60}$ in high purity and macroscopic quantities.^{25,30} These synthetic advances have made it feasible to perform terahertz spectroscopy and inelastic neutron scattering experiments on solid polycrystalline samples of $\text{He}@C_{60}$ at low temperatures with a good signal-to-noise ratio.

At first sight, $\text{He}@C_{60}$ is an unpromising object of study by both terahertz spectroscopy and neutron scattering. Since He atoms are neutral, their translational motion is not expected to interact with electromagnetic radiation. Furthermore, both ^3He and ^4He isotopes have small neutron scattering cross sections, and ^3He is a strong neutron absorber. Fortunately, although these concerns are valid, they are not fatal. An off-center He atom acquires a small induced electric dipole through its interactions with the encapsulating C_{60} cage, as is known for $\text{H}_2@C_{60}$.³² The induced dipole is approximately linearly dependent on the displacement from the cage center, allowing the He atom to interact weakly with THz irradiation. The feeble neutron scattering of both He isotopes may be compensated by a sufficiently large sample quantity.

We compare the experimentally determined potential to estimates from empirical two-body interaction potentials and from quantum chemistry calculations. Empirical two-body potentials give widely divergent results, even when those potentials are based on experimental helium–graphite scattering data. Møller–Plesset perturbation (MP2) theory techniques and density functional theory (DFT) methods, which explicitly include, or are empirically corrected to account for, dispersive interactions, are shown to provide good estimates for the interaction potential.

II. MATERIALS AND METHODS

A. Sample preparation

$^3\text{He}@C_{60}$ and $^4\text{He}@C_{60}$ were synthesized using a solid-state process for the critical step, as described in Ref. 30. The initial filling factors were 30%–50%. The samples were further purified by recirculating high-performance liquid chromatography (HPLC) on Cosmosil Buckyprep columns to remove trace impurities of $\text{H}_2\text{O}@C_{60}$. Without this precaution, strong neutron scattering by the hydrogen nuclei interferes strongly with the INS measurements. For THz spectroscopy, samples of high filling factor were required to get sufficient signal and were prepared by further recirculating HPLC. All samples were sublimed under vacuum before spectroscopic measurements.

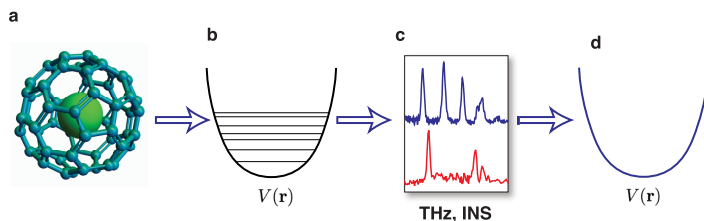


FIG. 1. (a) A C_{60} cage encapsulates a single noble gas atom. (b) The confinement potential of the encapsulated atom is described by the function $V(r)$. The quantum energy levels and wavefunctions of the encapsulated atom depend on $V(r)$. (c) Transitions between the energy levels are detected in the bulk solid state at low temperatures by terahertz spectroscopy and inelastic neutron scattering. (d) Analysis of the spectroscopic and neutron scattering data allows determination of the potential energy function, which may be compared with computational chemistry estimates.

B. Terahertz spectroscopy

THz absorption spectra were measured with an interferometer using a mercury arc light source and a 4 K bolometer as an intensity detector. The typical instrumental resolution was 0.3 cm^{-1} , which is below the width of the measured THz absorption lines. The $^4\text{He}@C_{60}$ sample had a filling factor of $f = 88.2\% \pm 0.5\%$, while the $^3\text{He}@C_{60}$ had a filling factor of $f = 97.2\% \pm 0.5\%$, as determined by ^{13}C NMR. The sample pellets were pressed from fine powders of solid $\text{He}@C_{60}$. The temperature dependence of the absorption spectra was measured by using a variable-temperature optical cryostat. More information is in the [supplementary material](#).

C. Inelastic neutron scattering

INS experiments were conducted using the IN1-Lagrange spectrometer at the Institut Laue-Langevin (ILL) in Grenoble. Incident neutrons are provided by the “hot source” moderator of the reactor, resulting in a high flux neutron beam. A choice of three different single crystal monochromators, namely, Si(111), Si(311), and Cu(220), are used to define the incident energy of the monochromatic neutron beam arriving at the sample using Bragg reflection. The neutrons scattered by the interaction with the sample enter a secondary spectrometer comprising a large area array of pyrolytic graphite analyzer crystals. The focusing geometry of the secondary spectrometer ensures that only neutrons with a fixed kinetic energy of 4.5 meV are detected by the ^3He detector. INS spectra were recorded in the energy transfer range of [5, 200] meV for the $^3\text{He}@C_{60}$ sample, while it was reduced to [5, 60] meV for $^4\text{He}@C_{60}$ as the time allowed for performing the latter experiment was reduced.

The powdered samples with respective masses of 1067 mg for $^3\text{He}@C_{60}$ ($f = 45\%$) and 294 mg for $^4\text{He}@C_{60}$ ($f = 40\%$) were loaded inside an Al foil and further inserted inside a cylindrical annulus before they were mounted at the tip of an orange cryostat and placed inside the IN1 spectrometer beam. The sample temperature was kept around 2.7 K. In order to subtract background and scattering from Al and from the C_{60} cage, a blank mass matching sample of C_{60} was measured using the same setup and an empty cell was also measured. In order to account for the strong absorption of $^3\text{He}@C_{60}$, a Cd sample was also measured, enabling one to correct from the incident energy dependent absorption of the sample. The neutron counts in [Fig. 3](#) were normalized to the incident neutron flux.

III. EXPERIMENTAL RESULTS

A. Terahertz spectroscopy

Terahertz absorption spectra for $^3\text{He}@C_{60}$ and $^4\text{He}@C_{60}$ at two different temperatures are shown in [Fig. 2](#). For both isotopologues, the high-temperature spectrum displays a comb of several clearly resolved THz peaks, with the ^3He peaks having higher frequencies than those of ^4He . As discussed below, the combs of THz peaks indicate that the potential energy function $V(r)$ for the encapsulated He does not have a purely quadratic dependence on the displacement r of the He atom from the cage center. This indicates that the He dynamics is not well-described as a harmonic three-dimensional oscillator.

The 5 K spectra in [Fig. 2](#) display a single peak with a partially resolved fine structure for both $^3\text{He}@C_{60}$ and $^4\text{He}@C_{60}$. These fundamental peaks correspond to transitions from the quantum ground

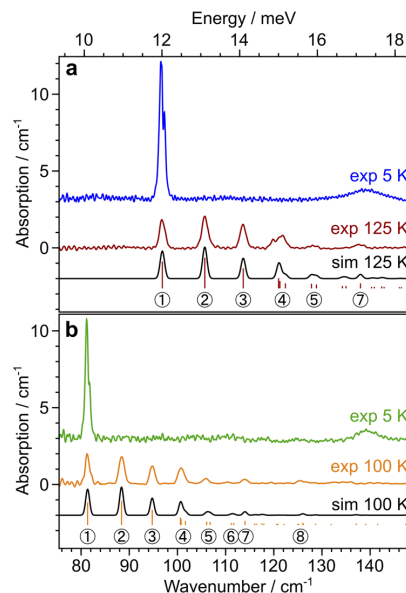


FIG. 2. THz spectroscopy of He endofullerenes. (a) THz absorption spectra of $^3\text{He}@C_{60}$ at temperatures of 5 K (blue) and 125 K (red). (b) THz absorption spectra of $^4\text{He}@C_{60}$ at temperatures of 5 K (green) and 100 K (orange). In both cases, the short vertical bars indicate the predicted positions of the terahertz absorption peaks for the radial potential energy function specified in [Table I](#), and their height is proportional to the absorption area. In both cases, the black curve is the sum of Gaussian peaks with the position and area defined by the vertical bars. The THz peaks are numbered according to the transition assignments in [Fig. 4\(b\)](#).

states of He in the two isotopologues. The fine structure requires further investigation but may be associated with a small perturbation of the confining potential by the merohedral disorder in the crystal lattice, meaning the inhomogeneous orientations of neighboring C_{60} cages with respect to each other. Similar effects have been identified for $\text{H}_2@C_{60}$.⁴²

B. Inelastic neutron scattering

Inelastic neutron scattering spectra for $^3\text{He}@C_{60}$ and $^4\text{He}@C_{60}$ are shown in [Fig. 3](#). The figure shows the difference between the INS of the He endofullerenes and that of the pure C_{60} . The INS spectra before subtraction are shown in the [supplementary material](#). Since C_{60} has no vibrational modes below $\sim 250\text{ cm}^{-1}$, and the low-energy phonon spectrum cancels precisely for the empty and filled fullerenes, the peaks below this energy threshold are clearly attributable to the quantized modes of the confined He atoms. As in the case of THz spectroscopy, the ^3He INS peaks are at higher energies than for ^4He .

The strong features above $\sim 250\text{ cm}^{-1}$ are attributed to the known vibrational modes of C_{60} molecules.⁵⁸ Raman studies have shown that the radial vibrational modes of the C_{60} cages are slightly blue-shifted by the presence of an endohedral noble gas atom.⁵⁹

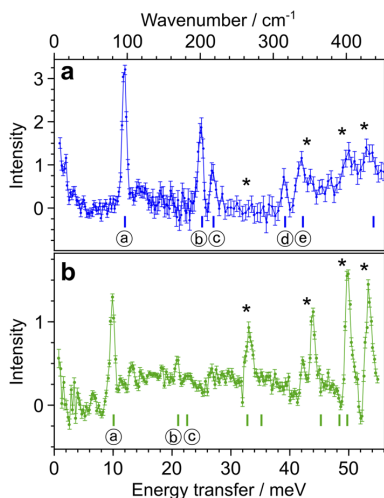


FIG. 3. Inelastic neutron scattering of He endofullerenes. (a) Inelastic neutron scattering spectra of $^3\text{He}@C_{60}$ at a temperature of 2.7 K (blue). (b) Inelastic neutron scattering spectra of $^4\text{He}@C_{60}$ at a temperature of 2.7 K (green). In both cases, a weighted difference between the scattering of $\text{He}@C_{60}$ and pure C_{60} is shown, with the weighting factors adjusted for best subtraction of the C_{60} background. The short vertical bars indicate the predicted positions of the INS peaks for the quantized He motion under the radial potential energy function specified in Table I. The INS peaks are labeled according to the transition assignments in Fig. 4(b). The peaks above $\sim 250\text{ cm}^{-1}$ and marked by asterisks are due to scattering from the C_{60} cages, whose modes are slightly modified in frequency by the presence of endohedral He.

These shifts lead to imperfect cancellation in the INS difference spectra, causing the dispersion-like features shown in Fig. 3, which are marked by asterisks. These subtraction artifacts are much stronger for ^4He than for ^3He for two reasons: (i) the C_{60} vibrational modes are slightly more shifted for ^4He than for ^3He due to its larger mass and (ii) ^4He has a much lower scattering cross section than ^3He . The poor signal-to-noise ratio for ^4He causes some of the expected peaks to be barely visible, an example being the peak marked “c” in Fig. 3(b).

IV. ANALYSIS

A. Energy levels and transitions

The Schrödinger equation for the confined atom (within the Born–Oppenheimer approximation) is given by

$$\hat{H}(\mathbf{r})\psi_{\mathbf{q}}(\mathbf{r}) = E_{\mathbf{q}}\psi_{\mathbf{q}}(\mathbf{r}), \quad (1)$$

where \mathbf{q} describes a set of quantum numbers, $\mathbf{q} = \{q_1, q_2, \dots\}$, and $E_{\mathbf{q}}$ is the energy of the stationary quantum state. The Hamiltonian operator \hat{H} is given by

$$\hat{H}(\mathbf{r}) = -\frac{\hat{p}^2}{2M} + V(\mathbf{r}), \quad (2)$$

where \hat{p} is the momentum operator and M is the atomic mass. In general, the energy levels $E_{\mathbf{q}}$ and stationary state wavefunctions $\psi_{\mathbf{q}}$ depend strongly on the potential energy function $V(\mathbf{r})$, where \mathbf{r} represents the nuclear coordinates of the encapsulated atom [Fig. 1(b)].

Equations (1) and (2) assume that the cage coordinates are fixed and neglect environmental effects from beyond the cage—although the treatment may readily be extended to include the electrostatic influence of the lattice environment, as has been carried out for studies of $\text{H}_2\text{O}@C_{60}$.^{36,51,55,56}

The potential energy of the He atom inside the cage may be described by a potential function $V(r, \theta, \phi)$, where r is the displacement of the He nucleus from the cage center and (θ, ϕ) are the polar angles. The C_{60} cage has icosahedral symmetry but may be treated as spherical to a good approximation at low excitation energies of the endohedral atom. The angular dependence may be dropped by assuming approximate spherical symmetry, $V(r, \theta, \phi) \simeq V(r)$. We assume a radial potential energy function of the form $V(r) = V_2r^2 + V_4r^4 + V_6r^6$, where $\{V_2, V_4, V_6\}$ are the polynomial coefficients.

The energy eigenvalues and eigenstates are given by $E_{n\ell m}$ and $\psi_{n\ell m}(r, \theta, \phi)$, respectively. The principal quantum number n takes values $n \in \{0, 1, \dots\}$ with the angular momentum quantum number ℓ given by $\ell \in \{0, 2, \dots, n\}$ (for even n) and $\ell \in \{1, 3, \dots, n\}$ (for odd n).⁶⁰ The azimuthal quantum number takes values $m \in \{-\ell, -\ell + 1, \dots, +\ell\}$. For spherical symmetry, the energies are independent of m , so the energy level $E_{n\ell}$ is $(2\ell + 1)$ -fold degenerate. The icosahedral cage symmetry introduces perturbation terms of spherical rank 6 and higher and only breaks the degeneracies of spherical states with large angular momentum quantum numbers. Within the spherical approximation, the stationary quantum states $\psi_{n\ell m}(r, \theta, \phi)$ are given by products of radial functions $R_{n\ell}(r)$ and spherical harmonics $Y_{\ell m}(\theta, \phi)$, just as for the electronic orbitals of a hydrogen atom.⁶⁰

The eigenvalues and eigenstates depend on the potential coefficients $\{V_2, V_4, V_6\}$ and the mass of the He atom. The electric-dipole-allowed transitions, which are observed in THz spectroscopy and described by the induced dipole moment coefficient A_1 , have the selection rule $\Delta\ell = \pm 1$; see the supplementary material. There are no relevant selection rules for the neutron scattering peaks.

B. Fitting of the potential

We treat the V_4 and V_6 terms as perturbations of the quadratic V_2 term, which corresponds to an isotropic three-dimensional harmonic oscillator. The solutions of the Schrödinger equation for the isotropic 3D harmonic oscillator are well-known^{60,61} and are given by

$$|n\ell m\rangle(r, \theta, \phi) = R_{n\ell}(r)Y_{\ell m}(\theta, \phi), \quad (3)$$

where the principal quantum number is given by $n \in \{0, 1, 2, \dots\}$ and the angular momentum quantum number ℓ takes values $\{0, 2, \dots, n\}$ for even n and $\{1, 3, \dots, n\}$ for odd n . The radial wavefunctions $R_{n\ell}(r)$ are proportional to generalized Laguerre polynomials,^{62,63} while the angular parts $Y_{\ell m}$ are spherical harmonics. The energy eigenvalues are given by

$$E_{n\ell m} = \hbar\omega_0\left(n + \frac{3}{2}\right) \quad (4)$$

TABLE I. Best-fit polynomial coefficients and confidence limits for the radial potential function $V(r) = V_2 r^2 + V_4 r^4 + V_6 r^6$ and induced dipole function $d_{1q} = \sqrt{4\pi/3} A_1 r Y_{1q}(\theta, \phi)$ experienced by the confined He isotopes; see the [supplementary material](#).

Parameter	^3He	^4He
V_2 (meV pm $^{-2}$)	$(2.58 \pm 0.06) \times 10^{-3}$	$(2.50 \pm 0.05) \times 10^{-3}$
V_4 (meV pm $^{-4}$)	$(3.37 \pm 0.15) \times 10^{-7}$	$(3.61 \pm 0.11) \times 10^{-7}$
V_6 (meV pm $^{-6}$)	$(2.79 \pm 0.12) \times 10^{-11}$	$(2.63 \pm 0.09) \times 10^{-11}$
A_1 (D pm $^{-1}$)	$(4.38 \pm 0.09) \times 10^{-4}$	$(4.58 \pm 0.06) \times 10^{-4}$

with the fundamental vibrational frequency $\omega_0 = (2V_2/\mu)^{1/2}$, where μ is the reduced mass (assumed here to be equal to the mass of the ^3He or ^4He atoms, since each C_{60} molecule is more than two orders of magnitude more massive than the encapsulated atom and is also coupled to the lattice).

The Schrödinger equation was solved approximately for finite V_4 and V_6 by numerically diagonalizing a matrix with elements given by $\langle n\ell m | V_4 r^4 + V_6 r^6 | n'\ell' m' \rangle$. Since the assumed Hamiltonian retains isotropic symmetry, all matrix elements are independent of the quantum number m and vanish for $\ell \neq \ell'$ and $m \neq m'$. In practice, the matrix was bounded by the quantum numbers $n \leq 18$ after checking for convergence. The THz peak intensities and peak positions were fitted, as described in the [supplementary material](#), allowing numerical estimation of the potential parameters V_2 (or ω_0), V_4 , and V_6 and the induced dipole moment amplitude A_1 . The derived eigenvalues were used to estimate the INS peak positions.

The fitting of the potential was performed independently for the two He isotopes. The best-fit solutions for the potential coefficients and their confidence limits are given in [Table I](#).

[Figure 4\(a\)](#) shows the best-fit potential functions for ^3He and ^4He inside the interior cavity of C_{60} . The best-fit potential has a distinct U-shape, which deviates strongly from the parabolic form of a harmonic oscillator. The best-fit potential curves for ^3He and ^4He differ by not more than $\pm 1 \text{ cm}^{-1}$ over the plotted energy range.

An energy level diagram for the confined He atoms, marked with the observed transitions, is shown in [Fig. 4\(b\)](#). The predicted positions of the relevant THz and INS transitions are shown by the vertical bars in [Figs. 2](#) and [3](#). Although some of the higher-energy transitions in the INS data are partially obscured by C_{60} features, the agreement with the spectroscopic results is gratifying. The remaining discrepancies between the experiment and theory are minor, such as the form of the peak labeled 4 in [Fig. 2\(a\)](#), and are currently unexplained. The close correspondence of the derived potential curves for ^3He and ^4He , despite the different masses of the isotopes and the very different observed frequencies, attests to the validity of the determination of $V(r)$.

C. Comparison with empirical potentials

There have been numerous attempts to model the nonbonded interactions between atoms using empirical two-body potential functions, such as the Lennard-Jones (LJ) 6-12 potential, or by more complex functional forms. Suitable functions and parameters have been proposed for the He- $\cdot\cdot\text{C}$ interaction.^{14,15,64,65,67} Some of the proposed two-body potentials were developed for modeling the scattering of He atoms from a graphite surface.^{14,15}

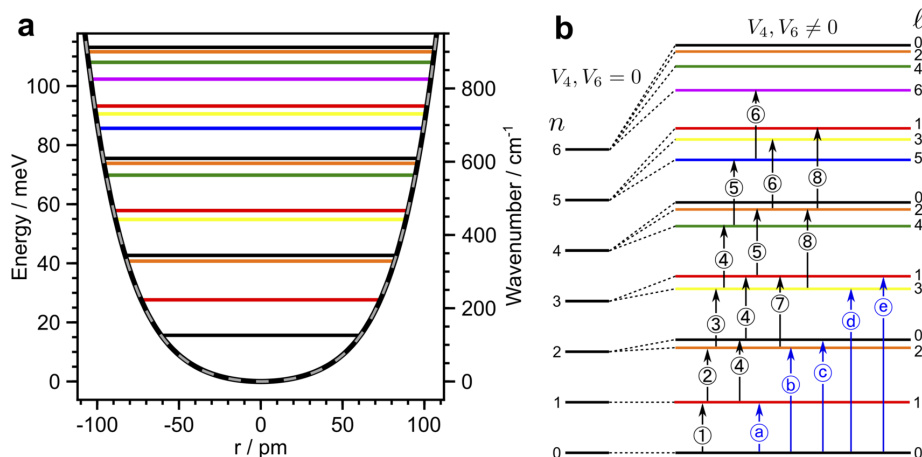


FIG. 4. (a) Radial potential energy functions $V(r)$ for ^3He in C_{60} (black solid curve) and for ^4He in C_{60} (gray dashed curve) together with the quantized energy levels for ^3He . The ^3He and ^4He potential curves are superposed within this energy range, leading to a “railway track” appearance of the plotted curve. The best-fit polynomial coefficients are given in [Table I](#). (b) Energy levels of the confined ^3He atoms, labeled by the quantum numbers $n\ell$. The energy levels for a harmonic oscillator are shown on the left. The finite V_4 and V_6 terms break the degeneracies between terms with different ℓ . All levels are $(2\ell + 1)$ -fold degenerate. The transitions observed in THz spectroscopy are labeled by circled numbers in black and correspond to the peaks in [Fig. 3](#). Colors are used to indicate the ℓ values of the energy levels. The transitions observed in INS are labeled by circled letters in blue and correspond to the peaks in [Fig. 3](#).

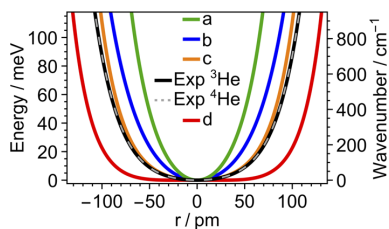


FIG. 5. Comparison of the experimentally determined radial potentials $V(r)$ (^3He : black solid curve; ^4He : gray dashed curve, superposed on the ^3He curve to give a “train track” appearance) with sums of reported He \cdots C interaction potentials: [(a) green] Lennard-Jones 6-8-12 potential with parameters from Carlos and Cole;¹⁴ [(b) blue] modified Buckingham potential (implemented in the MM3 program, as reported by Jiménez-Vázquez and Cross⁶⁴); [(c) orange] Lennard-Jones 6-12 potential with parameters from Pang and Brisse;⁶⁵ [(d) red] Lennard-Jones 6-12 potential with parameters from Carlos and Cole.¹⁴ The potentials used in (a) and (d) were used for the fitting of He \cdots C scattering data.¹⁴ The functional forms of the potentials and their associated parameters are given in the [supplementary material](#). In all cases, the He atom was displaced from the cage center toward the nucleus of a carbon atom. The confidence limits in the structural data for C_{60} ⁶⁶ lead to error margins on the empirical curves, which are smaller than the plotted linewidths.

Figure 5 compares the experimental $V(r)$ curve with predictions from published He \cdots C two-body interaction functions. In each case, the total potential energy $V(r)$ was estimated by locating the He atom at a distance r along a line from the center of the cage toward a C atom and summing the contributions from all 60 two-body He \cdots C potentials. The direction of the He displacement has a negligible effect on the calculated potential curves over the relevant energy range (see the [supplementary material](#)). The derived potentials are very sensitive to the geometry of the C_{60} cage, especially its radius R . We fixed the locations of all C nuclei to the best current estimates from neutron diffraction⁶⁶ as follows: bond lengths $h = 138.14 \pm 0.27$ pm for C–C bonds shared by two hexagons, $p = 145.97 \pm 0.18$ pm for C–C bonds shared by a hexagon and a pentagon, and distance of all carbon atoms from the cage center $R = 354.7 \pm 0.5$ pm. The width of the curves in Fig. 5 is greater than their confidence limits, which are dominated by the uncertainties in the structural parameters. Explicit functional forms and parameters for the empirical two-body potentials are given in the [supplementary material](#).

The most striking feature of Fig. 5 is the wide variation in derived potentials for different two-body interaction models. Of all the proposed two-body potentials, the Lennard-Jones 6-12 potential with parameters given by Pang and Brisse⁶⁵ [curve (c)] provides the best agreement with the experiment. The isotropic two-body potentials derived by fitting the experimental He/graphite scattering data^{14,15} [curves (a) and (d)] give poor fits to the experimental He@ C_{60} potential.

D. Comparison with quantum chemistry

The He@ C_{60} system is too large to be treated at the full *ab initio* level of quantum chemistry. The availability of an experimental radial potential function $V(r)$ allows the direct evaluation of approximate computational chemistry techniques—not only at

the equilibrium geometry but also for displacements of the He atom from the center of the C_{60} cage.

The radial potential $V(r)$ was evaluated by estimating the energy of a He@ C_{60} system using a range of computational chemistry algorithms with the He atom displaced by r from the center of the C_{60} cage. In all cases, the locations of the carbon atoms were fixed to the C_{60} geometry as determined by neutron diffraction⁶⁶ with the same parameters as used for the evaluation of the empirical potentials. The He atom was moved on the line connecting the cage center to a carbon nucleus. The direction of the He displacement has a negligible effect on the predicted potential curves over the relevant energy range (see the [supplementary material](#)). The potentials were calculated using the Psi4 program.⁶⁸ The functionals used for DFT were (i) the B3LYP functional, which is one of the most popular semi-empirical hybrid functionals;^{69–73} (ii) the B3LYP functional, including the Grimme D3 empirical dispersion correction with Beck–Johnson damping;^{5,74} (iii) the $\omega\text{B97X-V}$ functional, which includes a contribution from the nonlocal VV10 correlation functional and is designed to handle non-covalent interactions.⁶⁹ The potential was also calculated using second-order Møller–Plesset perturbation (MP2) theory,² including empirical spin-component-scaling (SCS) factors.⁷⁵ All potential calculations employed a counterpoise basis-set-superposition-error correction and converged to a good approximation with the correlation-consistent cc-pVXZ ($X = \text{D, T, Q, 5}$) basis sets.^{76,77} The calculations with $X = \text{Q}$ and $X = 5$ were found to agree within 1% in the case of MP2 theory and within 7% for the two DFT-functionals. More details on the quantum chemistry calculations are given in the [supplementary material](#).

Some comparisons are shown in Fig. 6. Density functional theory with the popular B3LYP functional^{69–73} overestimates the steepness of the confining potential, although the correspondence with the experiment is improved by including the empirical D3

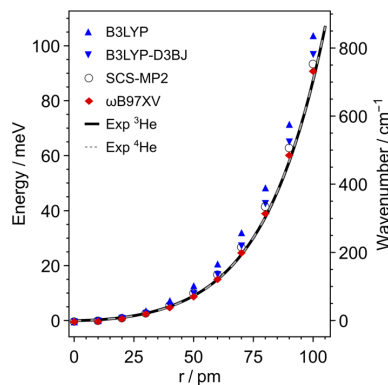


FIG. 6. Comparison of the experimentally determined He@ C_{60} radial potentials $V(r)$ (^3He : black solid curve; ^4He : gray dashed curve, superposed on the ^3He curve) with quantum chemical calculations using density functional and Møller–Plesset perturbation theories² as follows: (blue upper triangle) DFT using the B3LYP functional;^{70–73} (blue lower triangle) DFT using the B3LYP functional with D3BJ correction;^{3,74} (red diamond) DFT using the ωB97XV functional;^{69,78} and (open circle) spin-component-scaled Møller–Plesset perturbation theory (SCS-MP2).⁷⁵

correction with Beck–Johnson damping,^{5,74} DFT with the ω B97X-V functional⁶⁹ and Møller–Plesset perturbation (MP2) theory with spin-component-scaling (SCS) factors⁷⁵ give an acceptable correspondence between the calculated and experimentally determined potentials.

V. DISCUSSION

We have showed that the quantized energy levels of helium atoms encapsulated in C_{60} cages may be probed by THz spectroscopy and INS, despite the weak interactions of the He atoms with the electromagnetic field and with neutrons. The spectroscopic features were analyzed to obtain a detailed potential energy function for the interaction between the encapsulated species and the surrounding cage—an interaction dominated by nonbonded dispersion forces, which are hard to estimate experimentally. An excellent correspondence was obtained between the interaction potentials derived from independent $^3\text{He}@C_{60}$ and $^4\text{He}@C_{60}$ measurements, despite the different peak positions for the two samples.

The experimental $V(r)$ curve was compared with sums of published two-body He–C interactions. With a few exceptions, the summed two-body potentials have a poor correspondence with the experimental result. It is not a great surprise that the interaction of a He atom with a highly delocalized electronic structure such as C_{60} is hard to model as the sum of individual atom–atom interactions.

We also compared the experimentally derived interaction potential with those derived by quantum chemistry techniques. This allowed the validation of DFT methods that have been developed to deal with dispersive interactions, including the popular B3LYP functional with the D3 empirical dispersion correction^{5,74} and the ω B97X-V functional, which incorporates the nonlocal VV10 correlation functional and has been parameterized using a training set rich in nonbonding interactions.⁶⁹ Møller–Plesset perturbation theory with spin-component-scaling factors⁷⁵ also provides a good description of the confining potential of the encapsulated He atoms.

There are small discrepancies between the calculated and observed potentials. However, it is not yet known whether the remaining discrepancies reflect the limitations in the quantum chemistry algorithms or the limitations in the assumptions made when interpreting the experimental data—for example, the neglect of the influence exerted by the encapsulated He atoms on the cage radius. Precise measurements of the He@ C_{60} cage geometry by neutron scattering or x-ray diffraction are planned.

He atoms are small, have no static dipole moment, and have low polarizability. This makes He@ C_{60} a relatively easy case for computational chemistry. A stiffer challenge for computational chemistry is likely to be presented by compounds in which the endohedral species is polar, such as $\text{H}_2\text{O}@C_{60}$ ²⁴ and $\text{HF}@C_{60}$,²² and by endofullerenes such as $\text{CH}_4@C_{60}$,²³ where the fit with the cage is much tighter. Furthermore, the study of the systems with multiple atoms or molecules encapsulated in the same fullerene cage^{24,26,27} should allow the study of nonbonded molecule–molecule and molecule–atom interactions.

SUPPLEMENTARY MATERIAL

The [supplementary material](#) includes technical details of the terahertz spectroscopy; technical details of the inelastic neutron scattering measurements; quantum theory of a confined atom in a

spherical potential, including fitting procedures for the confining potential; details of the two-body potentials; and technical details of the computational chemistry calculations.

ACKNOWLEDGMENTS

This research was supported by EPSRC-UK (Grant Nos. EP/P009980/1, EP/T004320/1, and EP/P030491/1), the Estonian Ministry of Education and Research institutional research funding IUT23-3 and personal research funding PRG736, European Regional Development Fund Project No. TK134, and the European Union’s Horizon 2020 research and innovation program under Marie Skłodowska-Curie Grant Agreement No. 891400. The Institut Laue-Langevin is acknowledged for providing neutron beam time and support for M.A. through the ILL Ph.D. program. The authors acknowledge the use of the IRIDIS High Performance Computing Facility and associated support services at the University of Southampton in the completion of this work.

AUTHOR DECLARATIONS

Conflict of Interest

The authors have no conflicts to disclose.

Author Contributions

G.R.B. conceived the THz experiments. M.W., G.H., and R.J.W. synthesized and purified the compounds. G.R.B., T.J., A.S., U.N., and T.R. performed the THz experiments and processed the THz data. A.J.H. and S.R. designed the INS experiments. G.R.B., M.A., and S.R. performed the INS experiments and processed the INS data. G.R.B., M.A., and T.R. derived the potential function. J.R. and R.J.W. performed the quantum chemistry calculations. G.R.B., M.A., J.R., A.J.H., S.R., T.R., R.J.W., and M.H.L. developed the concept and drafted this paper. All authors reviewed the manuscript.

DATA AVAILABILITY

The data that support the findings of this study are available from the corresponding author upon reasonable request.

REFERENCES

- ¹D. Wales, *Energy Landscapes: Applications to Clusters, Biomolecules and Glasses*, Cambridge Molecular Science (Cambridge University Press, Cambridge, 2004).
- ²F. Jensen, *Introduction to Computational Chemistry*, 3rd ed. (Wiley, Chichester, 2017).
- ³M. Waller and S. Grimme, “Weak intermolecular interactions: A supermolecular approach,” in *Handbook of Computational Chemistry*, edited by J. Leszczynski (Springer Netherlands, Dordrecht, 2016), pp. 1–27.
- ⁴Y. Shao, Z. Gan, E. Epifanovsky, A. T. B. Gilbert, M. Wormit, J. Kussmann, A. W. Lange, A. Behn, J. Deng, X. Feng, D. Ghosh, M. Goldey, P. R. Horn, L. D. Jacobson, I. Kaliman, R. Z. Khaliullin, T. Kus, A. Landau, J. Liu, E. I. Proynov, Y. M. Rhee, R. M. Richard, M. A. Rohrdanz, R. P. Steele, E. J. Sundstrom, H. Lee Woodcock III, P. M. Zimmerman, D. Zuev, B. Albrecht, E. Alguire, B. Austin, G. J. O. Beran, Y. A. Bernard, E. Berquist, K. Brandhorst, K. B. Bravaya, S. T. Brown, D. Casanova, C.-M. Chang, Y. Chen, S. H. Chien, K. D. Closser, D. L. Crittenden, M. Diedenhofen, R. A. DiStasio, Jr., H. Do, A. D. Dutoi, R. G. Edgar, S. Fatehi, L. Fusti-Molnar, A. Ghysels, A. Golubeva-Zadorozhnaya, J. Gomes, M. W. D. Hanson-Heine, P. H. P. Harbach, A. W. Hauser, E. G. Hohenstein, Z. C. Holden, T.-C. Jagau, H. Ji, B. Kaduk, K. Khistyayev, J. Kim, J. Kim, R. A. King,

- P. Klunzinger, D. Kosenkov, T. Kowalczyk, C. M. Krauter, K. U. Lao, A. D. Laurer, K. V. Lawler, S. V. Levchenko, C. Y. Lin, F. Liu, E. Livshits, R. C. Lochan, A. Luenser, P. Manohar, S. F. Manzer, S.-P. Mao, N. Mardirossian, A. V. Marenich, S. A. Maurer, N. J. Mayhall, E. Neuscamman, C. M. Oana, R. Olivares-Amaya, D. P. O'Neill, J. A. Parkhill, T. M. Perrine, R. Peverati, A. Prociuk, D. R. Rehn, E. Rosta, N. J. Russ, S. M. Sharada, S. Sharma, D. W. Small, A. Sodt, T. Stein, D. Stück, Y.-C. Su, A. J. W. Thom, T. Tsuchimochi, V. Vanovschi, L. Vogt, O. Vydrov, T. Wang, M. A. Watson, J. Wenzel, A. White, C. F. Williams, J. Yang, S. Yeganeh, S. R. Yost, Z.-Q. You, I. Y. Zhang, X. Zhang, Y. Zhao, B. R. Brooks, G. K. L. Chan, D. M. Chipman, C. J. Cramer, W. A. Goddard III, M. S. Goddard, W. J. Hehre, A. Klamt, H. F. Schaefer III, M. W. Schmidt, C. D. Sherrill, D. G. Truhlar, A. Warshel, X. Xu, A. Aspuru-Guzik, R. Baer, A. T. Bell, N. A. Besley, J.-D. Chai, A. Dreuw, B. D. Dunietz, T. R. Furlani, S. R. Gwaltney, C.-P. Hsu, Y. Jung, J. Kong, D. S. Lambrecht, W. Liang, C. Ochsenfeld, V. A. Rassolov, L. V. Slipchenko, J. E. Subotnik, T. Van Voorhis, J. M. Herbert, A. I. Krylov, P. M. W. Gill, and M. Head-Gordon, "Advances in molecular quantum chemistry contained in the Q-Chem 4 program package," *Mol. Phys.* **113**, 184–215 (2015).
- ⁵S. Grimme, J. Antony, S. Ehrlich, and H. Krieg, "A consistent and accurate *ab initio* parametrization of density functional dispersion correction (DFT-D) for the 94 elements H-Pu," *J. Chem. Phys.* **132**, 154104 (2010).
- ⁶F. A. Momany, L. M. Carruthers, R. F. McGuire, and H. A. Scheraga, "Intermolecular potentials from crystal data. III. Determination of empirical potentials and application to the packing configurations and lattice energies in crystals of hydrocarbons, carboxylic acids, amines, and amides," *J. Phys. Chem.* **78**, 1595–1620 (1974).
- ⁷F. N. Keutsch and R. J. Saykally, "Water clusters: Untangling the mysteries of the liquid, one molecule at a time," *Proc. Natl. Acad. Sci. U. S. A.* **98**, 10533–10540 (2001).
- ⁸P. Hobza and K. Müller-Dethlefs, *Non-Covalent Interactions: Theory and Experiment* (The Royal Society of Chemistry, 2009).
- ⁹L. Zhu and P. Johnson, "Mass analyzed threshold ionization spectroscopy," *J. Chem. Phys.* **94**, 5769–5771 (1991).
- ¹⁰H. Krause and H. J. Neusser, "Dissociation energy of neutral and ionic benzene-noble gas dimers by pulsed field threshold ionization spectroscopy," *J. Chem. Phys.* **99**, 6278–6286 (1993).
- ¹¹A. Van Orden and R. J. Saykally, "Small carbon clusters: Spectroscopy, structure, and energetics," *Chem. Rev.* **98**, 2313–2358 (1998).
- ¹²T. P. Softley, "Applications of molecular Rydberg states in chemical dynamics and spectroscopy," *Int. Rev. Phys. Chem.* **23**, 1–78 (2004).
- ¹³D. Farias and K.-H. Rieder, "Atomic beam diffraction from solid surfaces," *Rep. Prog. Phys.* **61**, 1575–1664 (1998).
- ¹⁴W. E. Carlos and M. W. Cole, "Interaction between a He atom and a graphite surface," *Surf. Sci.* **91**, 339–357 (1980).
- ¹⁵M. W. Cole, D. R. Frankl, and D. L. Goodstein, "Probing the helium-graphite interaction," *Rev. Mod. Phys.* **53**, 199–210 (1981).
- ¹⁶M. Saunders, H. A. Jimenez-Vazquez, R. J. Cross, and R. J. Poreda, "Stable compounds of helium and neon: He@C₆₀ and Ne@C₆₀," *Science* **259**, 1428–1430 (1993).
- ¹⁷M. Saunders, R. J. Cross, H. A. Jimenez-Vazquez, R. Shimshi, and A. Khong, "Noble gas atoms inside fullerenes," *Science* **271**, 1693–1697 (1996).
- ¹⁸K. Komatsu, M. Murata, and Y. Murata, "Encapsulation of molecular hydrogen in fullerene C₆₀ by organic synthesis," *Science* **307**, 238–240 (2005).
- ¹⁹K. Kurotobi and Y. Murata, "A single molecule of water encapsulated in fullerene C₆₀," *Science* **333**, 613–616 (2011).
- ²⁰Y. Rubin, T. Jarrosson, G.-W. Wang, M. D. Bartberger, K. N. Houk, G. Schick, M. Saunders, and R. J. Cross, "Insertion of helium and molecular hydrogen through the orifice of an open fullerene," *Angew. Chem., Int. Ed.* **40**, 1543–1546 (2001).
- ²¹M. Murata, S. Maeda, Y. Morinaka, Y. Murata, and K. Komatsu, "Synthesis and reaction of fullerene C₇₀ encapsulating two molecules of H₂," *J. Am. Chem. Soc.* **130**, 15800–15801 (2008).
- ²²A. Krachmalnicoff, R. Bounds, S. Mamone, S. Alom, M. Concistrè, B. Meier, K. Kouřil, M. E. Light, M. R. Johnson, S. Rols, A. J. Horsewill, A. Shugai, U. Nagel, T. Rööm, M. Carravetta, M. H. Levitt, and R. J. Whitby, "The dipolar endofullerene HF@C₆₀," *Nat. Chem.* **8**, 953–957 (2016).
- ²³S. Bloodworth, G. S. Itinova, S. Alom, S. Vidal, G. R. Bacanu, S. J. Elliott, M. E. Light, J. M. Herniman, G. J. Langley, M. H. Levitt, and R. J. Whitby, "First synthesis and characterization of CH₄@C₆₀," *Angew. Chem., Int. Ed.* **58**, 5038–5043 (2019).
- ²⁴Y. Murata, S. Maeda, M. Murata, and K. Komatsu, "Encapsulation and dynamic behavior of two H₂ molecules in an open-cage C₇₀," *J. Am. Chem. Soc.* **130**, 6702–6703 (2008).
- ²⁵Y. Morinaka, F. Tanabe, M. Murata, Y. Murata, and K. Komatsu, "Rational synthesis, enrichment, and ¹³C NMR spectra of endohedral C₆₀ and C₇₀ encapsulating a helium atom," *Chem. Commun.* **46**, 4532–4534 (2010).
- ²⁶R. Zhang, M. Murata, T. Aharen, A. Wakamiya, T. Shimoaka, T. Hasegawa, and Y. Murata, "Synthesis of a distinct water dimer inside fullerene C₇₀," *Nat. Chem.* **8**, 435–441 (2016).
- ²⁷R. Zhang, M. Murata, A. Wakamiya, T. Shimoaka, T. Hasegawa, and Y. Murata, "Isolation of the simplest hydrated acid," *Sci. Adv.* **3**, e1602833 (2017).
- ²⁸S. Bloodworth, G. Hoffman, M. C. Walkey, G. R. Bacanu, J. M. Herniman, M. H. Levitt, and R. J. Whitby, "Synthesis of Ar@C₆₀ using molecular surgery," *Chem. Commun.* **56**, 10521–10524 (2020).
- ²⁹G. R. Bacanu, J. Rantaharju, G. Hoffman, M. C. Walkey, S. Bloodworth, M. Concistrè, R. J. Whitby, and M. H. Levitt, "An internuclear *J*-coupling of ³He induced by molecular confinement," *J. Am. Chem. Soc.* **142**, 16926–16929 (2020).
- ³⁰G. Hoffman, M. C. Walkey, J. Gräsvik, G. R. Bacanu, S. Alom, S. Bloodworth, M. E. Light, M. H. Levitt, and R. J. Whitby, "A solid state intramolecular Wittig reaction enables efficient synthesis of endofullerenes including Ne@C₆₀, ³He@C₆₀ and HD@C₆₀," *Angew. Chem., Int. Ed.* **60**, 8960–8966 (2021).
- ³¹M. H. Levitt, "Spectroscopy of light-molecule endofullerenes," *Philos. Trans. R. Soc., A* **371**, 20120429 (2013).
- ³²S. Mamone, M. Ge, D. Huvonen, U. Nagel, A. Danquigny, F. Cuda, M. C. Gossel, Y. Murata, K. Komatsu, M. H. Levitt, T. Rööm, and M. Carravetta, "Rotor in a cage: Infrared spectroscopy of an endohedral hydrogen-fullerene complex," *J. Chem. Phys.* **130**, 081103–081104 (2009).
- ³³M. Ge, U. Nagel, D. Huvonen, T. Rööm, S. Mamone, M. H. Levitt, M. Carravetta, Y. Murata, K. Komatsu, X. Lei, and N. J. Turro, "Infrared spectroscopy of endohedral HD and D₂ in C₆₀," *J. Chem. Phys.* **135**, 114511 (2011).
- ³⁴C. Beduz, M. Carravetta, J. Y. C. Chen, M. Concistrè, M. Denning, M. Frunzi, A. J. Horsewill, O. G. Johannessen, R. Lawler, X. Lei, M. H. Levitt, Y. Li, S. Mamone, Y. Murata, U. Nagel, T. Nishida, J. Ollivier, S. Rols, T. Rööm, R. Sarkar, N. J. Turro, and Y. Yang, "Quantum rotation of *ortho* and *para*-water encapsulated in a fullerene cage," *Proc. Natl. Acad. Sci. U. S. A.* **109**, 12894–12898 (2012).
- ³⁵T. Rööm, L. Peedu, M. Ge, D. Huvonen, U. Nagel, S. Ye, M. Xu, Z. Bačić, S. Mamone, M. H. Levitt, M. Carravetta, J. Y.-C. Chen, X. Lei, N. J. Turro, Y. Murata, and K. Komatsu, "Infrared spectroscopy of small-molecule endofullerenes," *Philos. Trans. R. Soc., A* **371**, 20110631 (2013).
- ³⁶A. Shugai, U. Nagel, Y. Murata, Y. Li, S. Mamone, A. Krachmalnicoff, S. Alom, R. J. Whitby, M. H. Levitt, and T. Rööm, "Infrared spectroscopy of an endohedral water in fullerene," *J. Chem. Phys.* **154**, 124311 (2021).
- ³⁷S. S. Zhukov, V. Balos, G. Hoffman, S. Alom, M. Belyanchikov, M. Nebiogu, S. Roh, A. Pronin, G. R. Bacanu, P. Abramov, M. Wolf, M. Dressel, M. H. Levitt, R. J. Whitby, B. Gorshunov, and M. Sajadi, "Rotational coherence of encapsulated *ortho* and *para* water in fullerene-C₆₀ revealed by time-domain terahertz spectroscopy," *Sci. Rep.* **10**, 18329 (2020).
- ³⁸N. J. Turro, J. Y. C. Chen, E. Sartori, M. Ruzzi, A. Marti, R. Lawler, S. Jockusch, J. López-Gejo, K. Komatsu, and Y. Murata, "The spin chemistry and magnetic resonance of H₂@C₆₀. From the Pauli principle to trapping a long lived nuclear excited spin state inside a buckyball," *Acc. Chem. Res.* **43**, 335 (2009).
- ³⁹S. Mamone, M. Concistrè, I. Heinmaa, M. Carravetta, I. Kuprov, G. Wall, M. Denning, X. Lei, J. Y.-C. Chen, Y. Li, Y. Murata, N. J. Turro, and M. H. Levitt, "Nuclear magnetic resonance of hydrogen molecules trapped inside C₇₀ fullerene cages," *ChemPhysChem* **14**, 3121–3130 (2013).
- ⁴⁰G. R. Bacanu, G. Hoffman, M. Amponsah, M. Concistrè, R. J. Whitby, and M. H. Levitt, "Fine structure in the solution state ¹³C-NMR spectrum of C₆₀ and its endofullerene derivatives," *Phys. Chem. Chem. Phys.* **22**, 11850–11860 (2020).
- ⁴¹A. J. Horsewill, K. S. Panesar, S. Rols, J. Ollivier, M. R. Johnson, M. Carravetta, S. Mamone, M. H. Levitt, Y. Murata, K. Komatsu, J. Y.-C. Chen, J. A. Johnson, X. Lei, and N. J. Turro, "Inelastic neutron scattering investigations of the quantum

- molecular dynamics of a H₂ molecule entrapped inside a fullerene cage,” *Phys. Rev. B* **85**, 205440 (2012).
- ⁴²S. Mamone, M. R. Johnson, J. Ollivier, S. Rols, M. H. Levitt, and A. J. Horsewill, “Symmetry-breaking in the H₂@C₆₀ endofullerene revealed by inelastic neutron scattering at low temperature,” *Phys. Chem. Chem. Phys.* **18**, 1998–2005 (2016).
- ⁴³S. Mamone, M. Jiménez-Ruiz, M. R. Johnson, S. Rols, and A. J. Horsewill, “Experimental, theoretical and computational investigation of the inelastic neutron scattering spectrum of a homonuclear diatomic molecule in a nearly spherical trap: H₂@C₆₀,” *Phys. Chem. Chem. Phys.* **18**, 29369–29380 (2016).
- ⁴⁴M. Xu, F. Sebastianelli, Z. Bačić, R. Lawler, and N. J. Turro, “H₂, HD, and D₂ inside C₆₀: Coupled translation-rotation eigenstates of the endohedral molecules from quantum five-dimensional calculations,” *J. Chem. Phys.* **129**, 064313 (2008).
- ⁴⁵M. Xu, F. Sebastianelli, Z. Bačić, R. Lawler, and N. J. Turro, “Quantum dynamics of coupled translational and rotational motions of H₂ inside C₆₀,” *J. Chem. Phys.* **128**, 011101–011104 (2008).
- ⁴⁶M. Xu, F. Sebastianelli, B. R. Gibbons, Z. Bačić, R. Lawler, and N. J. Turro, “Coupled translation-rotation eigenstates of H₂ in C₆₀ and C₇₀ on the spectroscopically optimized interaction potential: Effects of cage anisotropy on the energy level structure and assignments,” *J. Chem. Phys.* **130**, 224306 (2009).
- ⁴⁷M. Ge, U. Nagel, D. Huvonen, T. Rööm, S. Mamone, M. H. Levitt, M. Caravatta, Y. Murata, K. Komatsu, J. Y.-C. Chen, and N. J. Turro, “Interaction potential and infrared absorption of endohedral H₂ in C₆₀,” *J. Chem. Phys.* **134**, 054507 (2011).
- ⁴⁸S. Mamone, J. Y.-C. Chen, R. Bhattacharyya, M. H. Levitt, R. G. Lawler, A. J. Horsewill, T. Rööm, Z. Bačić, and N. J. Turro, “Theory and spectroscopy of an incarcerated quantum rotor: The infrared spectroscopy, inelastic neutron scattering and nuclear magnetic resonance of H₂@C₆₀ at cryogenic temperature,” *Coord. Chem. Rev.* **255**, 938–948 (2011).
- ⁴⁹M. Xu, S. Ye, A. Powers, R. Lawler, N. J. Turro, and Z. Bačić, “Inelastic neutron scattering spectrum of H₂@C₆₀ and its temperature dependence decoded using rigorous quantum calculations and a new selection rule,” *J. Chem. Phys.* **139**, 064309 (2013).
- ⁵⁰P. M. Felker and Z. Bačić, “Communication: Quantum six-dimensional calculations of the coupled translation-rotation eigenstates of H₂O@C₆₀,” *J. Chem. Phys.* **144**, 201101 (2016).
- ⁵¹P. M. Felker, V. Vlček, I. Hietanen, S. FitzGerald, D. Neuhauser, and Z. Bačić, “Explaining the symmetry breaking observed in the endofullerenes H₂@C₆₀, HF@C₆₀, and H₂O@C₆₀,” *Phys. Chem. Chem. Phys.* **19**, 31274–31283 (2017).
- ⁵²Z. Bačić, “Perspective: Accurate treatment of the quantum dynamics of light molecules inside fullerene cages: Translation-rotation states, spectroscopy, and symmetry breaking,” *J. Chem. Phys.* **149**, 100901 (2018).
- ⁵³Z. Bačić, M. Xu, and P. M. Felker, “Coupled translation-rotation dynamics of H₂ and H₂O inside C₆₀: Rigorous quantum treatment,” in *Advances in Chemical Physics* (Wiley-Blackwell, 2018), pp. 195–216.
- ⁵⁴M. Xu, P. M. Felker, S. Mamone, A. J. Horsewill, S. Rols, R. J. Whitby, and Z. Bačić, “The endofullerene HF@C₆₀: Inelastic neutron scattering spectra from quantum simulations and experiment, validity of the selection rule, and symmetry breaking,” *J. Phys. Chem. Lett.* **10**, 5365–5371 (2019).
- ⁵⁵P. M. Felker and Z. Bačić, “Flexible water molecule in C₆₀: Intramolecular vibrational frequencies and translation-rotation eigenstates from fully coupled nine-dimensional quantum calculations with small basis sets,” *J. Chem. Phys.* **152**, 014108 (2020).
- ⁵⁶M. Xu, P. M. Felker, and Z. Bačić, “Light molecules inside the nanocavities of fullerenes and clathrate hydrates: Inelastic neutron scattering spectra and the unexpected selection rule from rigorous quantum simulations,” *Int. Rev. Phys. Chem.* **39**, 425–463 (2020).
- ⁵⁷D. E. Giblin, M. L. Gross, M. Saunders, H. Jimenez-Vazquez, and R. J. Cross, “Incorporation of helium into endohedral complexes of C₆₀ and C₇₀ containing noble-gas atoms: A tandem mass spectrometry study,” *J. Am. Chem. Soc.* **119**, 9883–9890 (1997).
- ⁵⁸S. Rols, C. Bousige, J. Cambedouzo, P. Launois, J.-L. Sauvajol, H. Schober, V. N. Agafonov, V. A. Davydov, and J. Ollivier, “Unravelling low lying phonons and vibrations of carbon nanostructures: The contribution of inelastic and quasi-elastic neutron scattering,” *Eur. Phys. J.: Spec. Top.* **213**, 77–102 (2012).
- ⁵⁹F. Cimpoesu, S. Ito, H. Shimotani, H. Takagi, and N. Drago, “Vibrational properties of noble gas endohedral fullerenes,” *Phys. Chem. Chem. Phys.* **13**, 9609–9615 (2011).
- ⁶⁰C. Cohen-Tannoudji, B. Diu, and F. Laloë, *Quantum Mechanics*, 2nd ed. (Wiley-VCH, 2020).
- ⁶¹W. H. Shaffer, “Degenerate modes of vibration and perturbations in polyatomic molecules,” *Rev. Mod. Phys.* **16**, 245–259 (1944).
- ⁶²S. Flügge, *Practical Quantum Mechanics*, Classics in Mathematics (Springer-Verlag, Berlin, Heidelberg, 1999).
- ⁶³B. H. Bransden and C. J. Joachain, *Quantum Mechanics*, 2nd ed. (Pearson Prentice Hall, 2000).
- ⁶⁴H. A. Jiménez-Vázquez and R. J. Cross, “Equilibrium constants for noble-gas fullerene compounds,” *J. Chem. Phys.* **104**, 5589–5593 (1996).
- ⁶⁵L. Pang and F. Brisse, “Endohedral energies and translation of fullerene-noble gas clusters G@C_n (G = helium, neon, argon, krypton and xenon; n = 60 and 70),” *J. Phys. Chem.* **97**, 8562–8563 (1993).
- ⁶⁶F. Leclercq, P. Damay, M. Foukani, P. Chieux, M. C. Bellissent-Funel, A. Rasat, and C. Fabre, “Precise determination of the molecular geometry in fullerene C₆₀ powder: A study of the structure factor by neutron scattering in a large momentum-transfer range,” *Phys. Rev. B* **48**, 2748–2758 (1993).
- ⁶⁷A. Terry Amos, T. Frank Palmer, A. Walters, and B. L. Burrows, “Atom-atom potential parameters for van der Waals complexes of aromatics and rare-gas atoms,” *Chem. Phys. Lett.* **172**, 503–508 (1990).
- ⁶⁸R. M. Parrish, L. A. Burns, D. G. A. Smith, A. C. Simmonett, A. E. DePrince III, E. G. Hohenstein, U. Bozkaya, A. Y. Sokolov, R. Di Remigio, R. M. Richard *et al.*, “Psi4 1.1: An open-source electronic structure program emphasizing automation, advanced libraries, and interoperability,” *J. Chem. Theory Comput.* **13**, 3185–3197 (2017).
- ⁶⁹N. Mardirossian and M. Head-Gordon, “Thirty years of density functional theory in computational chemistry: An overview and extensive assessment of 200 density functionals,” *Mol. Phys.* **115**, 2315–2372 (2017).
- ⁷⁰C. Lee, W. Yang, and R. G. Parr, “Development of the Colle-Salvetti correlation-energy formula into a functional of the electron density,” *Phys. Rev. B* **37**, 785–789 (1988).
- ⁷¹S. H. Vosko, L. Wilk, and M. Nusair, “Accurate spin-dependent electron liquid correlation energies for local spin density calculations: A critical analysis,” *Can. J. Phys.* **58**, 1200–1211 (1980).
- ⁷²A. D. Becke, “Density-functional thermochemistry. III. The role of exact exchange,” *J. Chem. Phys.* **98**, 5648–5652 (1993).
- ⁷³P. J. Stephens, F. J. Devlin, C. F. Chabalowski, and M. J. Frisch, “Ab initio calculation of vibrational absorption and circular dichroism spectra using density functional force fields,” *J. Phys. Chem.* **98**, 11623–11627 (1994).
- ⁷⁴S. Grimme, S. Ehrlich, and L. Goerigk, “Effect of the damping function in dispersion corrected density functional theory,” *J. Comput. Chem.* **32**, 1456–1465 (2011).
- ⁷⁵S. Grimme, “Improved second-order Møller-Plesset perturbation theory by separate scaling of parallel- and antiparallel-spin pair correlation energies,” *J. Chem. Phys.* **118**, 9095–9102 (2003).
- ⁷⁶T. H. Dunning, Jr., “Gaussian basis sets for use in correlated molecular calculations. I. The atoms boron through neon and hydrogen,” *J. Chem. Phys.* **90**, 1007–1023 (1989).
- ⁷⁷D. E. Woon and T. H. Dunning, Jr., “Gaussian basis sets for use in correlated molecular calculations. IV. Calculation of static electrical response properties,” *J. Chem. Phys.* **100**, 2975–2988 (1994).
- ⁷⁸N. Mardirossian and M. Head-Gordon, “ωB97X-V: A 10-parameter, range-separated hybrid, generalized gradient approximation density functional with nonlocal correlation, designed by a survival-of-the-fittest strategy,” *Phys. Chem. Chem. Phys.* **16**, 9904–9924 (2014).

Appendix 2

2

T. Jafari, G. R. Bacanu, A. Shugai, U. Nagel, M. Walkey, G. Hoffman, M. H. Levitt, R. J. Whitby, and T. Rõõm, "Terahertz spectroscopy of the helium endo-fullerene He@C₆₀," *Phys. Chem. Chem. Phys.*, vol. 24, p. 9943, April 2022


 Cite this: *Phys. Chem. Chem. Phys.*,
 2022, 24, 9943

Terahertz spectroscopy of the helium endofullerene He@C₆₀

 Tanzeeha Jafari,^a George Razvan Bacanu,^b Anna Shugai,^a Urmas Nagel,^a Mark Walkey,^b Gabriela Hoffman,^b Malcolm H. Levitt,^b Richard J. Whitby^b and Toomas Rõõm^{*a}

We studied the quantized translational motion of single He atoms encapsulated in molecular cages by terahertz absorption. The temperature dependence of the THz absorption spectra of ³He@C₆₀ and ⁴He@C₆₀ crystal powder samples was measured between 5 and 220 K. At 5 K there is an absorption line at 96.8 cm⁻¹ (2.90 THz) in ³He@C₆₀ and at 81.4 cm⁻¹ (2.44 THz) in ⁴He@C₆₀, while additional absorption lines appear at higher temperature. An anharmonic spherical oscillator model with a displacement-induced dipole moment was used to model the absorption spectra. Potential energy terms with powers of two, four and six and induced dipole moment terms with powers one and three in the helium atom displacement from the fullerene cage center were sufficient to describe the experimental results. Excellent agreement is found between potential energy functions derived from measurements on the ³He and ⁴He isotopes. One absorption line corresponds to a three-quantum transition in ⁴He@C₆₀, allowed by the anharmonicity of the potential function and by the non-linearity of the dipole moment in He atom displacement. The potential energy function of icosahedral symmetry does not explain the fine structure observed in the low temperature spectra.

 Received 31st January 2022,
 Accepted 3rd April 2022

DOI: 10.1039/d2cp00515h

rsc.li/pccp

1 Introduction

The highly symmetric fullerene, C₆₀, has attracted considerable attention since its discovery in 1985.¹ One of the fascinating features is its ability to hold an atom or small molecule within a hollow molecular cavity, forming a complex known as an endofullerene. The discovery of the first endofullerene, La@C₆₀, occurred soon after by the same group of researchers, when they were able to capture lanthanum by a laser ablation technique.² Endofullerenes provide a rare opportunity to examine the behavior of guest species under conditions that have never been studied before such as the confinement of guest species inside a nano-scale cage which is non-polar, homogeneous and in the case of C₆₀, highly symmetric.^{3,4}

Different methods have been used to synthesize endofullerenes. Endofullerenes may be synthesized by the arc discharge method in which carbon is evaporated at high temperature in the presence of a metal⁵ or an inert gas.^{6,7} Insertion of atoms into the fullerene cage is possible by exposing the fullerene to high temperatures and high pressures of inert gas⁸ or by ion bombardment.^{9–11} However, these methods are not suited to capture small molecules and the production yield is small. In a

major development, the group of Komatsu¹² synthesized H₂@C₆₀ endofullerenes by a process known as molecular surgery.¹³ Following in the footsteps of Komatsu, the group of Murata successfully encapsulated a water molecule inside C₆₀.¹⁴ Molecular surgery has been the most successful process to produce high-yield endofullerenes until today. A large number of endofullerenes are now available in macroscopic quantities, such as¹² and its isotopologues,¹⁵ H₂O@C₆₀,¹⁴ HF@C₆₀,¹⁶ and CH₄,¹⁷ and atoms like Ar,¹⁸ He^{19,20} and Ne.²⁰

Endofullerenes are of great interest due to quantum effects which are more evident at cryogenic temperatures. The encapsulation isolates atoms and molecules from each other preventing them from forming liquid or solid condensates even at the lowest temperatures. This provides a unique opportunity to study their internal degrees of freedom at the lowest temperatures. The translational motion becomes quantized due to the confining potential. The confinement also prompts the coupling of translational and rotational motions of the encapsulated molecule. The combination of small molecular mass and tight confinement inside the nano cage gives rise to a discrete and well separated translation-rotational energy level structure. The most studied endohedral complex is H₂@C₆₀, which laid the basis for understanding the quantum dynamics of the isolated systems.^{4,21} Different spectroscopic techniques have been used to demonstrate the effect of the highly symmetric trapping potential on the quantum dynamics of the hydrogen

^a National Institute of Chemical Physics and Biophysics, Akadeemia tee 23, Tallinn 12618, Estonia. E-mail: toomas.room@kbfi.ee

^b School of Chemistry, University of Southampton, SO17 1BJ Southampton, UK



molecule, including infrared spectroscopy (IR)^{22–24} and inelastic neutron scattering (INS).^{25–28}

There is a growing interest in extending spectroscopic studies to noble gas endofullerenes. The research interest in noble gas endofullerenes is evident from the theoretical studies that have been done so far.^{29–36} The incarceration of large noble gas atoms results in the structural and electronic distortion of which has been examined by IR and Raman,³⁴ NMR,³⁷ X-ray³⁸ and electronic spectroscopy.³⁹

The first experimental evidence of a noble gas endofullerene was He@C₆₀. It was spotted by mass spectrometry when the 4 atom was incorporated in C₆₀ as the highly accelerated C₆₀⁺ ions struck with helium gas⁹ and later found in fullerenes produced by arc discharge in the He gas.⁶ Despite that, and the 2010 synthesis of He@C₆₀ by molecular surgery,¹⁹ the He endofullerene potential energy function study was restricted to theoretical explanations^{31,33,40} and the experimental data were inadequate for supporting the available information. Recently, the translational energies of He@C₆₀ were determined by inelastic neutron scattering and THz spectroscopy studies and the experimentally derived potential was compared to estimates from quantum chemistry calculations and from sums of empirical two-body potentials.⁴¹

Here, as compared to ref. 41, we present a more detailed temperature-dependence study of THz absorption by endohedral 3 and 4 isotopes between 5 and 220 K. Also, we obtained a better fit of line intensities by including an r^3 term in the expansion of the dipole moment in the helium atom displacement r . The temperature dependence and the new fit of line intensities confirms the assignment of the He atom translational energy levels and the accuracy of the derived potential energy surface reported in our previous paper.⁴¹

2 Theory

The potential energy surface of the He atom stems from its interaction with the interior of the C₆₀ molecule. Although the molecule has icosahedral symmetry we approximate it by spherical symmetry. Within this approximation we may ignore the coupling of the C₆₀ rotations and librations to the He motion. Since the masses of and C₆₀ He are different by two orders of magnitude, $M_{C_{60}} \gg M_{He}$, we assume that the C₆₀ center of the mass position is not affected by the motion of C₆₀ the He atom. Also, we ignore the effect of translational motion of in the crystal lattice and its molecular vibrations. Thus, in this model the He atom moves in a spherically symmetric rigid potential well. This motion can be described by the harmonic spherical oscillator model^{42–44} where the coordinate \mathbf{r} is the displacement of He center of mass from the C₆₀ center of mass. To obtain agreement with the observed THz spectra, we add anharmonic corrections to the harmonic potential function. This makes the separation of energy levels non-equidistant.

In general, a free He atom does not absorb electromagnetic radiation at THz frequencies due to the lack of an electric dipole moment. However, similar to the encapsulated hydrogen

molecule,^{15,22,23} He atoms acquire a dipole moment from the interaction with the inner surface of C₆₀. This interaction is modulated by the translational motion of the He atom causing the translational modes to become THz-active.

2.1 Anharmonic spherical oscillator

The Hamiltonian \hat{H} for one helium trapped in a spherical potential well is given as

$$\hat{H} = \hat{H}_0 + \hat{V}', \quad (1)$$

where

$$\hat{V}' = V_4 r^4 + V_6 r^6 \quad (2)$$

is the perturbation (anharmonic term) added to the harmonic spherical oscillator Hamiltonian⁴⁴

$$\hat{H}_0 = \frac{p^2}{2M_{He}} + V_2 r^2. \quad (3)$$

The harmonic Hamiltonian has eigenstates

$$|n, \ell, m\rangle = R_{n\ell}(r) Y_{\ell m}(\theta, \phi), \quad (4)$$

where $r \in \{0, \infty\}$, $\theta \in \{0, \pi\}$ and $\phi \in \{0, 2\pi\}$. The angular part of each wavefunction m is an ortho-normalized spherical harmonic,

$$\int_0^{2\pi} d\phi \int_0^\pi \sin\theta d\theta [Y_{\ell m'}(\theta, \phi)]^* Y_{\ell m}(\theta, \phi) = \delta_{\ell\ell'} \delta_{mm'}, \quad (5)$$

with the Condon and Shortley phase convention⁴⁵

$$Y_{\ell m}^*(\theta, \phi) = Y_{\ell m}(\theta, -\phi) = (-1)^m Y_{\ell, -m}(\theta, \phi). \quad (6)$$

The radial wavefunction is⁴²

$$R_{n\ell}(r) = C(n, \ell, \zeta) e^{-\frac{\zeta r^2}{2}} (\zeta r^2)^{\frac{\ell}{2}} L_{\frac{n-\ell}{2}}^{\ell+\frac{1}{2}}[\zeta r^2], \quad (7)$$

where $L_n^{\alpha}[x]$ is generalised Laguerre polynomial and $\zeta = M_{He} \omega_T \hbar^{-1}$. The radial part of the wavefunction is normalized by the constant

$$C(n, \ell, \zeta) = \sqrt{\frac{2 \left(\frac{n-\ell}{2}\right)!}{\left(\frac{n+\ell+1}{2}\right)!}} \zeta^{\frac{3}{4}}. \quad (8)$$

The eigenenergies of the harmonic Hamiltonian (3) are

$$E_n = \hbar \omega_T \left(n + \frac{3}{2} \right), \quad (9)$$

where the angular frequency is

$$\omega_T = \sqrt{\frac{2V_2}{M_{He}}}. \quad (10)$$

The problem can be solved by diagonalizing the Hamiltonian (1) using the basis set of functions (4) where $n \in \{0, 1, \dots, n_{\max}\}$. The angular momentum quantum number ℓ is given by $\ell \in \{0, 2, \dots, n\}$ for even n and $\ell \in \{1, 3, \dots, n\}$ for odd n .



It is practical to use the reduced matrix elements, $\langle \ell_f \| T_k \| \ell_i \rangle$, of the spherical tensor operator T_{kq} of rank k , $q \in \{-k, -k+1, \dots, k\}$, which are independent of m and q .⁴⁶ The matrix element of T_{kq} is

$$\langle \tau_f, \ell_f, m_f | T_{kq} | \tau_i, \ell_i, m_i \rangle = (-1)^{\ell_f - m_f} \begin{pmatrix} \ell_f & k & \ell_i \\ -m_f & q & m_i \end{pmatrix} \langle \tau_f, \ell_f \| T_k \| \tau_i, \ell_i \rangle, \quad (11)$$

where the angular part of the reduced matrix element is

$$\langle \ell_f \| T_k \| \ell_i \rangle = (-1)^{\ell_f} \sqrt{\frac{(2\ell_f + 1)(2k + 1)(2\ell_i + 1)}{4\pi}} \begin{pmatrix} \ell_f & k & \ell_i \\ 0 & 0 & 0 \end{pmatrix}. \quad (12)$$

The six symbols in the brackets denote the Wigner $3j$ -symbol. The $3j$ -symbol is zero if conditions $|\ell_f - \ell_i| \leq k \leq \ell_f + \ell_i$ and $m_f + q + m_i = 0$ are not satisfied; if $m_f = q = m_i = 0$, then the $3j$ -symbol is not zero if the sum $\ell_f + k + \ell_i$ is an even number.⁴⁶

For the isotropic spherical potential, eqn (2), the rank of potential spherical operator is $k = 0$. Therefore, the states with different ℓ and m are not mixed. Perturbation V_{N^N} mixes states with different n and the eigenstate of Hamiltonian (1), $|\tau, \ell, m\rangle$, is a linear superposition of states $|n, \ell, m\rangle$, eqn (4). Evaluation of matrix elements of the radial part of harmonic oscillator wavefunction, $\langle R_{n_f, \ell_f} | r^N | R_{n_i, \ell_i} \rangle$ with $\ell_f = \ell_i$, shows that non-zero elements are $|n_f - n_i| \leq N$ where n_i and n_f must have the same parity. Because each energy level of the anharmonic Hamiltonian (1) is $(2\ell + 1)$ -fold degenerate in m , it is sufficient to include only the $|n, \ell, 0\rangle$ functions in the basis set. This reduces the number of states by a factor $2\ell + 1$ for each ℓ .

2.2 THz absorption line strengths of the spherical oscillator

We write the dipole moment in spherical harmonics $Y_{1q}(\theta, \phi)$ as a function of He displacement keeping the first two terms, linear and cubic in r ,

$$d_{1q} = \sqrt{\frac{4\pi}{3}} (A_{1,1q}r + A_{3,1q}r^3) Y_{1q}(\theta, \phi), \quad q \in \{-1, 0, +1\}. \quad (13)$$

Only the odd powers of r are present because the dipole moment is a polar vector. $A_{1,1q}$ and $A_{3,1q}$ are the amplitude coefficients. In the spherical symmetry the amplitudes do not depend on q , and we use a simplified notation, $A_{1,1q} \equiv A_1$ and

$A_{3,1q} \equiv A_3$. The length of the dipole moment vector is $|\mathbf{d}| =$

$$\sqrt{\sum_{q=-1}^{+1} (d_{1q})^* d_{1q}} = A_1 r + A_3 r^3, \text{ as follows from the normaliza-}$$

tion of spherical harmonics, $\sum_{m=-\ell}^{\ell} Y_{\ell m}^*(\theta, \phi) Y_{\ell m}(\theta, \phi) = \frac{2\ell + 1}{4\pi}$.

Using the Fermi golden rule we write the THz absorption line area for the radiation polarized linearly in the z direction, which couples to the dipole moment z component, $d_z = d_{10}$. Since the energy E of Hamiltonian (1) is degenerate in initial and final state quantum numbers m we perform the summation over m_i and m_f for a given transition frequency,

$\omega_{\bar{n}} = (E_f - E_i)/hc_0$. The absorption line area $S_{\bar{n}}$ is

$$S_{\bar{n}} = \int_{\omega_{\bar{n}}} \alpha_{\bar{n}}(\omega) d\omega = \mathcal{N}_s f_0 \frac{2\pi^2}{\hbar \epsilon_0 c_0 \eta} \left(\frac{\eta^2 + 2}{3} \right)^2 \omega_{\bar{n}} (p_i - p_f) \times \sum_{m_i, m_f} |\langle \tau_f, \ell_f, m_f | d_{10} | \tau_i, \ell_i, m_i \rangle|^2, \quad (14)$$

where the integral is taken over the frequency range $\omega_{\bar{n}}$ spanning the transition $|i\rangle \rightarrow |f\rangle$. c_0 is the speed of light in a vacuum, ϵ_0 is the permittivity of vacuum, h is the Planck and k_B is the Boltzmann constant. Factor $(\eta^2 + 2)/3$ is the enhancement of radiation electric field at the molecule embedded in dielectric⁴⁷ and η is the index of refraction (for $\eta = 2$, ref. 48). $\mathcal{N} = 1.48 \times 10^{27} \text{ m}^{-3}$ is the number density of molecules in the solid and $f_0 = \mathcal{N}_s / \mathcal{N}$ is the filling factor; $\mathcal{N}_s = \mathcal{N}_\bullet + \mathcal{N}_\circ$ where \mathcal{N}_\bullet is the number density of filled and \mathcal{N}_\circ is the number density of empty cages. All units are SI and the transition frequency, $\omega_{\bar{n}}$, is measured in wavenumbers, number of waves in one meter, $[\omega_{\bar{n}}] = \text{m}^{-1}$. p_i and p_f are the thermal Boltzmann populations of the initial and final states:

$$p_i = \frac{e^{-E_i/k_B T}}{\sum_j (2\ell_j + 1) e^{-E_j/k_B T}}, \quad (15)$$

where $2\ell_j + 1$ is the degeneracy of state $|\tau_j, \ell_j, m_j\rangle$ in quantum number m_j .

The sum over m_i and m_f in eqn (14) is

$$\sum_{m_i, m_f} |\langle \tau_f, \ell_f, m_f | d_{10} | \tau_i, \ell_i, m_i \rangle|^2 = \frac{1}{3} |\langle \tau_f, \ell_f \| d_1 \| \tau_i, \ell_i \rangle|^2, \quad (16)$$

where $\langle \tau_f, \ell_f \| d_1 \| \tau_i, \ell_i \rangle$ is the reduced matrix element of d_{1q} with the angular part given by eqn (12). Since for the dipole moment $k = 1$, a selection rule of THz absorption by a spherical oscillator, $\ell_f = \ell_i \pm 1$, follows from the properties of the $3j$ -symbol. The selection rule for n comes from the matrix element of the radial part of harmonic oscillator wavefunction, $\langle R_{n_f, \ell_f} | r^N | R_{n_i, \ell_i} \rangle$. For the linear term in eqn (13) it is $n_f = n_i \pm 1$ and for the cubic term it is $|n_f - n_i| \leq 3$, where n_i and n_f must have different parities.

3 Experimental

³He@C₆₀ and ⁴He@C₆₀ were synthesised using a solid-state process for the critical step, as described in ref. 20. The initial filling factors were 30% to 50%. The samples were further purified by recirculating HPLC on Cosmosil Buckyprep columns to remove trace impurities of H₂O@C₆₀ and empty C₆₀. Finally, the ⁴He@C₆₀ sample had a filling factor of $f_0 = (88.2 \pm 0.5)\%$ while the ³He@C₆₀ had a filling factor of $f_0 = (97.2 \pm 0.5)\%$, as determined by ¹³C NMR. Samples were sublimed under vacuum.

The sublimed powdered sample was put inside the 3 mm diameter hole of cylindrical brass frame and pressed under the vacuum into a pellet. The mass and thickness of the ³He@C₆₀ pellet were 28 mg and 2.16 mm and of the ⁴He@C₆₀ pellet were 21 mg and 1.72 mm. The brass frame with the pellet was



inserted into a sample chamber with two thin-film polypropylene windows and with a vacuum line for pumping and filling with helium heat exchange gas. The sample chamber was in a thermal contact with the cold finger of the cryostat. The cryostat was placed inside the interferometer Vertex 80v sample compartment. The cold finger with the sample chamber was moved up and down by letting the beam through the sample chamber or through a reference hole with 3 mm diameter. The transmission spectra were recorded up to 300 cm^{-1} using a Hg lamp, a $6\text{ }\mu\text{m}$ Mylar beam splitter, and a 4 K bolometer. The spectral resolution was 0.2 cm^{-1} which was found to be smaller than the width of the He absorption lines or their sub-components.

The absorption spectra were calculated from $\alpha(\omega) = -d^{-1} \ln[\mathcal{T}(\omega)\mathcal{R}(\omega)^{-1}]$ where $\alpha(\omega)$ is the absorption coefficient, $\mathcal{T}(\omega)$ is the transmission, and $\mathcal{R}(\omega)$ is the amount of light lost in reflections from the pellet surfaces and the sample chamber windows. The measured transmission is $\mathcal{T}(\omega) = I_s(\omega)/I_r(\omega)$, where $I_s(\omega)$ is the beam intensity at the bolometer with the sample chamber in the beam and $I_r(\omega)$ is the beam intensity at the bolometer with the reference hole in the beam. The reflection losses and the absorption in the sample chamber windows affect the background absorption but do not affect the absorption line areas of helium.

4 Results

The THz absorption spectra of $^3\text{He}@C_{60}$ and $^4\text{He}@C_{60}$ at different temperatures in a spectral range between 75 and 150 cm^{-1} are shown in Fig. 1. The baseline of the 5 K spectrum was fitted and then subtracted. The same procedure but covering only the spectral range around the line no. 1 was applied to the spectra of higher temperatures. For the rest of the spectra above the line no. 1 the average of 5 and 15 K spectra was used for the baseline subtraction. The broad line at about 140 cm^{-1} in the 5 K spectrum is the absorption feature of the mylar windows on the sample cell.

The spectra from the two isotopes share the same pattern of absorption spectra but with the ^4He lines shifted to higher energy relative to the ^3He lines. The line intensities of the two isotopes are similar. For ^3He , a line at 97 cm^{-1} is the only line present at 5 K and its intensity decreases with increasing temperature. This indicates that it corresponds to a transition from the ground state. With the rise in temperature, energy levels above the ground state become thermally populated and we observe six more absorption lines: 106, 114, 120, 122, 128 and 138 cm^{-1} .

In the case of $^4\text{He}@C_{60}$, we observed two transitions from the ground state, at 81 cm^{-1} and at 284 cm^{-1} . By increasing the temperature additional absorption lines become visible at 88, 95, 101, 106, 111, 114 and 126 cm^{-1} . The line no. 9 starts from the ground state as is confirmed by its T dependence, Fig. 7 in the Appendix. This line cannot be detected in $^3\text{He}@C_{60}$ THz spectra because of the strong absorption by the fullerene at its resonance frequency, 340.6 cm^{-1} in Table 4, but was observed

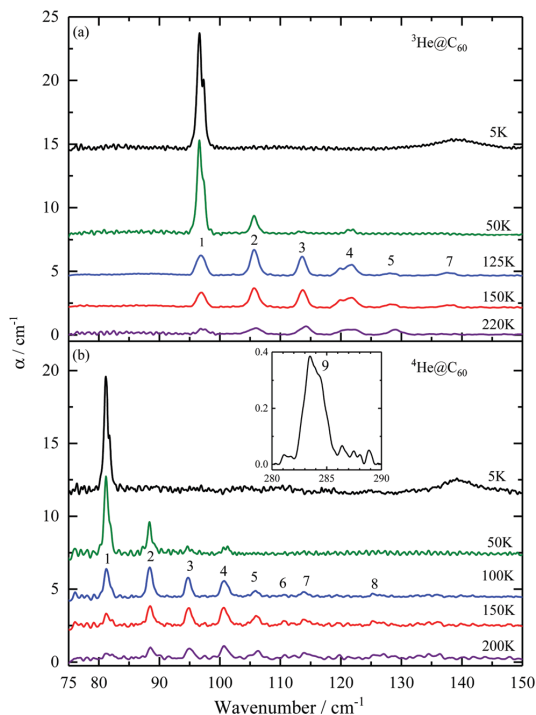


Fig. 1 Temperature dependence of THz absorption spectra of $^3\text{He}@C_{60}$ (a) and $^4\text{He}@C_{60}$ (b). Absorption lines are numbered according to the transitions between the energy levels as shown in Fig. 3. Inset to (b) shows the $^4\text{He}@C_{60}$ line no. 9 at 5 K. The line intensities are not corrected for the filling factor f_0 , see eqn (14).

in the inelastic neutron scattering spectrum, line no. e in ref. 41.

The lowest energy peak has a two-component structure which is visible at low temperatures. The separation of components is approximately 0.8 cm^{-1} for $^3\text{He}@C_{60}$ and 0.7 cm^{-1} for $^4\text{He}@C_{60}$, Tables 4 and 5 in the Appendix. We did not see any additional structure at the best resolution we used, 0.2 cm^{-1} . The possible origin of line no. 1 and no. 9 splitting is discussed in Section 5.

The synthetic spectra were fitted with a spherical oscillator model, as described in the Appendix, and the result is shown in Fig. 2. The best spherical oscillator model fit parameters are listed in Table 2. As compared to our previous fit⁴¹ the extra term, A_3r^3 , was added to the dipole moment expansion, eqn (13). This gives a better fit of the line intensities. The spherical oscillator fit revealed that line number 4 consists of three closely spaced transitions, and lines 5 and 6 of two transitions. The energy diagram together with the numbered transitions is shown in Fig. 3 and the energies of corresponding levels in Table 2. The list of line frequencies and intensities calculated with the spherical oscillator model best fit parameters for ^3He (125 K) and ^4He (100 K) is given in the Appendix, Tables 4 and 5.



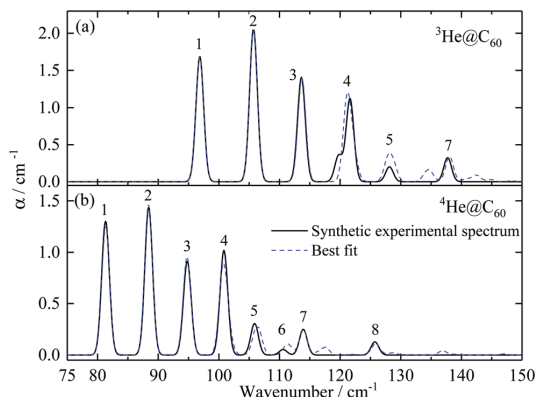


Fig. 2 Synthetic experimental THz spectrum (solid black line) and the best fit result (blue dashed line) of $^3\text{He}@C_{60}$ at 125 K (a) and $^4\text{He}@C_{60}$ at 100 K (b).

In Fig. 4 the areas of the first five THz absorption lines of $^3\text{He}@C_{60}$ and $^4\text{He}@C_{60}$ are compared with the temperature dependence of line areas derived from the spherical oscillator model fit. The line areas at each temperature are calculated using the parameters $\{V_2, V_4, V_6, A_1, A_3\}$ obtained from the anharmonic oscillator model fit of 125 K and 100 K spectra of ^3He and ^4He , respectively. For each line the line areas are normalized to the maximum of the theoretical intensity *versus* temperature curve. Same normalization factors are applied to each experimental line respectively.

5 Discussion

The overlap of potential energy curves of two He isotopes proves the reliability of our fit as the difference of potential curves is only about $\pm 0.5 \text{ cm}^{-1}$ over the energy scale probed by THz spectroscopy, Fig. 5(b). The potential is strongly anharmonic. It can be seen that for the displacement $r > 75 \text{ pm}$ the anharmonic contribution to the potential energy, $V_4 r^4 + V_6 r^6$, starts to dominate over the harmonic part, $V_2 r^2$. The significance of anharmonic correction is also evidenced by the composition of the oscillator wave function: as the energy increases the single n -component of a wavefunction becomes less dominant meaning that the components with other n values are mixed in Table 2. States with different ℓ values are not mixed by the isotropic potential and each level is $2\ell + 1$ degenerate in the quantum number m .

Experimentally determined translational energies of $A@C_{60}$ endohedral complexes are summarized in Table 3. Although the anharmonic contributions to the potential have been determined experimentally,^{15,22,23} a more detailed comparison with is not meaningful as firstly, has translation-rotation coupling terms in the potential and secondly, it misses the V_6 term in the potential fit. The shape of the potential curve is not known for other A species. We approximate the translational energy, ω_T , as the difference of energies between the ground

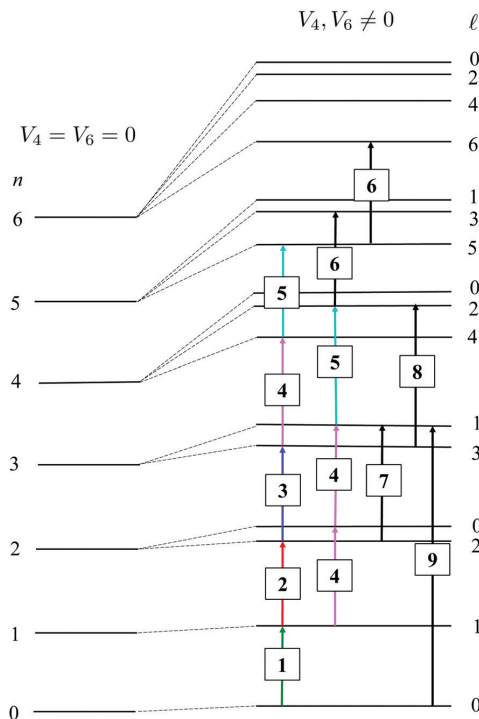


Fig. 3 Energy level diagram and THz transitions of $\text{He}@C_{60}$. The principal translational quantum number is n and the angular momentum quantum number is ℓ . The energy levels of a spherical harmonic oscillator are degenerate in ℓ , shown on left. The anharmonic terms in the potential, and V_6 , split the energy levels with different ℓ and each energy level has the unique ℓ value within the spherical symmetry, on the right. The mixing of states with different n by V_4 - and V_6 -term is not shown on the diagram. The THz transitions between the translational energy levels observed in the experiment are labeled with numbers, see Fig. 1 and Tables 4 and 5, and the translational energies are in Table 2.

state and the first excited translational state. Assuming harmonic approximation, $V_2^A \approx M_A \omega_{01}^2 / 2$, we scaled the potential of other species, V_2^A , relative to hydrogen, V_2^H . The last column demonstrates that $1/\sqrt{M_A}$ scaling of translational frequency of different A species has no predictive power. In general, the interaction of neutral A with can be separated into repulsive interaction and electrostatic interaction expanded in induction and dispersion terms.³³ Since has no electric dipole nor quadrupole moment the induction terms are zero. The absence of induction terms may only partially explain the “softness” of potential because the dominant interactions are repulsion and dipole-dipole dispersion for endohedral atoms and molecules.³³ In general, modern quantum chemistry calculations of $\text{He}@C_{60}$ give a good description of $V(r)$.⁴¹

To further validate the potential parameters of obtained from the fit of single high temperature spectra we compare the temperature dependence of line intensities of measured and calculated spectra, Fig. 4. The parameters determined from



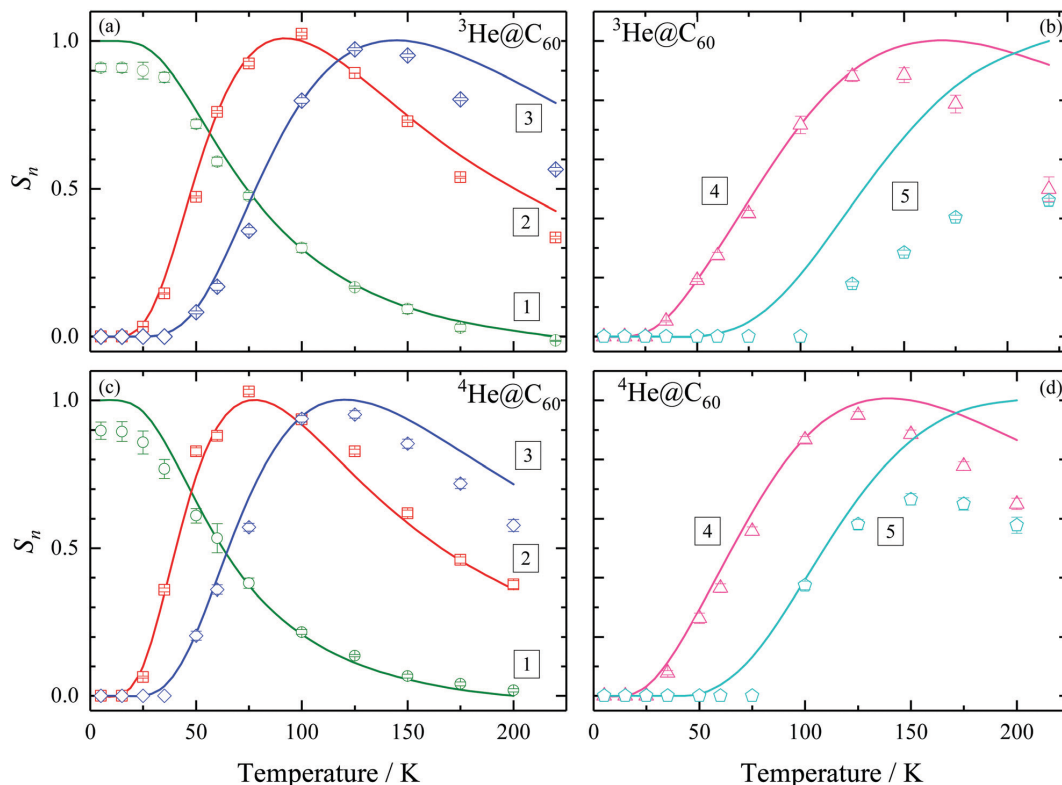


Fig. 4 Temperature dependence of normalized THz absorption line areas S_n of $^3\text{He}@C_{60}$, panels (a) and (b) and of $^4\text{He}@C_{60}$, panels (c) and (d). Symbols are experimental line areas with errors from the fit with Gaussian lines and solid lines are theoretical areas calculated with the parameters from Table 1. Line areas have been normalized to the maximum value in the T dependence of theoretical area for each line. The lines are numbered according to the transitions shown in Fig. 3 and listed in Tables 4 and 5.

the ^3He (^4He) fit at 125 K (100 K) describe the temperature dependence from 5 to 200 K rather well except for the line no. 5. Other lines, no. 6, no. 7, no. 8 and no. 9, are weak and their intensities could not be determined reliably from the experimental spectra and therefore their T dependence was not analyzed. The intensity of the lowest frequency line no. 1, transition from the ground state, is overestimated by the fit at the lowest temperatures. The discrepancy of calculated and measured T dependence could be due the thermal motion of C_{60} not taken into account in our model.

The dipole moment of is induced by the displacement from the C_{60} cage center. The estimate for the displacement of the first transition can be made from the potential energy which is half of the total energy, $V(r) = E_1/2$. Using the data from Table 2, $E_1 = 222.5 \text{ cm}^{-1}$ (^3He) and $E_1 = 187.9 \text{ cm}^{-1}$ (^4He), we obtain the displacement to be about 60 pm. The dipole moment induced by 60 pm displacement is $d = A_1 r + A_3 r^3 = 2.7 \times 10^{-2} \text{ D}$, small compared to permanent dipole moments of molecules. For example, the permanent screened dipole moment of C_{60} endohedral water is about 0.5 D.^{49,50}

Transition no. 9 starts from the ground state with $\ell = 0$ and predominantly with $n = 0$ radial content. The final state is the

$\ell = 1$ state, see Fig. 3 and Table 2, but with predominantly $n = 3$ radial part. It is an allowed electric dipole transition with the selection rule $\Delta\ell = +1$ but three translation quanta are created, $\Delta n = +3$. All other lines, no. 1 to no. 8, are ordinary one quantum transitions, $\Delta n = +1$. The r^3 term in the dipole moment expansion allows the $\Delta n = +3$ excitation by radiation. However, because of the mixing of states by anharmonic potential, $n = 0$ state is mixed with $n = 2$ and $n = 3$ state is the mixed $n = 1$ state, the linear term in r of the dipole moment expansion with the selection rule $\Delta n = +1$ can induce the three-quantum transition. Thus, in there are two factors what activate the three-quantum transition, the anharmonicity of the potential and the r^3 term in the dipole moment expansion.

Two absorption lines, no. 1 and no. 9, show partially resolved fine structure at 5 K, Fig. 1. These lines are the transitions from the ground state with $\ell = 0$ to the state $\ell = 1$, see Fig. 3 and Table 2. In the icosahedral potential the first A_g symmetry representation after fully spherical potential, rank $k = 0$, is a combination of spherical harmonics of rank $k = 6$.⁵¹ Rank 6 term in the potential splits states with $\ell \geq 3$, which cannot explain the fine structure of helium line no. 1 and no. 9.



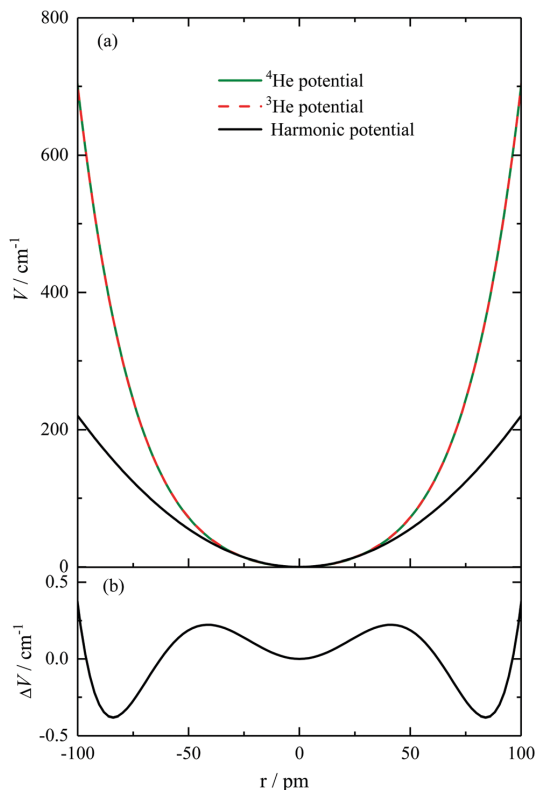


Fig. 5 (a) Potential energy curves of ^3He and ^4He , $V(r) = V_2r^2 + V_4r^4 + V_6r^6$, calculated with parameters from Table 1. The harmonic part of ^3He potential curve, V_2r^2 , is plotted as blue solid line. The potential curves of two isotopes, green solid line of ^3He and red dashed line of ^4He , are indistinguishable in this plot. (b) The difference between the potential curves of ^3He and ^4He , $\Delta V = V_3 - V_4$, is less than $\pm 0.5 \text{ cm}^{-1}$.

To explain the spectral line splitting, a potential with symmetry lower than the icosahedral or two different exohedral environments must be invoked.

Fullerene molecules stop rotating below 90 K.⁵² This leads to two sites distinguished by the relative orientation of the central cage and its 12 nearest-neighbor C_{60} .⁵³ In the pentagonal orientation the electron-rich double bonds are facing pentagonal rings and in the hexagonal orientation the electron-rich double bonds are facing hexagonal rings of nearest-neighbor cages. It was proposed by Felker *et al.*⁵⁴ that the orientational order creates electrostatic field that interacts with the quadrupole moment of endohedral molecule. Their model explains the splitting of $J = 1$ rotational state observed in $\text{H}_2@C_{60}$,^{22,23,28} $\text{HF}@C_{60}$,¹⁶ and $\text{H}_2\text{O}@C_{60}$.^{49,55,56} This mechanism is not applicable to the helium atom because it does not have rotational degrees of freedom nor quadrupole moment. The icosahedral symmetry of $V(r)$ could still be disturbed by the nearest-neighbor C_{60} molecules. A splitting similar to the splitting of line no. 1 was observed in $\text{H}_2@C_{60}$ for the $\ell = 0 \rightarrow \ell = 1$

Table 1 The best fit parameter values for $^3\text{He}@C_{60}$ and $^4\text{He}@C_{60}$. V_2 , V_4 and V_6 are potential parameters, eqn (2) and (3), and A_1 and A_3 are the dipole moment parameters, eqn (13)

κ_i	$^3\text{He}@C_{60}$	$^4\text{He}@C_{60}$	Unit
V_2	$(2.500 \pm 0.015) \times 10^{-3}$	$(2.46 \pm 0.04) \times 10^{-3}$	meV pm^{-2}
V_4	$(3.64 \pm 0.03) \times 10^{-7}$	$(3.77 \pm 0.08) \times 10^{-7}$	meV pm^{-4}
V_6	$(2.560 \pm 0.017) \times 10^{-11}$	$(2.46 \pm 0.06) \times 10^{-11}$	meV pm^{-6}
A_1	$(3.83 \pm 0.10) \times 10^{-4}$	$(3.73 \pm 0.22) \times 10^{-4}$	D pm^{-1}
A_3	$(1.7 \pm 0.3) \times 10^{-8}$	$(2.3 \pm 0.6) \times 10^{-8}$	D pm^{-3}

Table 2 Translational energy levels of $^3\text{He}@C_{60}$ and $^4\text{He}@C_{60}$ obtained from the fit of THz absorption spectra. Translational energy E , the angular momentum quantum number ℓ (single-valued for each energy level), and the amplitude squared of the main component of eigenstate with the principal quantum number n . The zero point energy 125.7 cm^{-1} (106.5 cm^{-1}) of ^3He (^4He) has been subtracted

$^3\text{He}@C_{60}$				$^4\text{He}@C_{60}$			
E/cm^{-1}	ℓ	n	$ \xi_{n,\ell} ^2$	E/cm^{-1}	ℓ	n	$ \xi_{n,\ell} ^2$
0	0	0	0.95	0	0	0	0.95
96.8	1	1	0.87	81.4	1	1	0.88
202.6	2	2	0.77	169.8	2	2	0.79
218.3	0	2	0.64	182.1	0	2	0.68
316.3	3	3	0.65	264.5	3	3	0.69
340.6	1	3	0.43	283.7	1	3	0.48
437.3	4	4	0.54	365.1	4	4	0.58
469.4	2	6	0.39	390.6	2	6	0.39
483.0	0	6	0.40	401.1	0	6	0.40
565.1	5	5	0.43	471.1	5	5	0.47
604.3	3	7	0.36	502.0	3	7	0.38
625.8	1	7	0.31	519.0	1	7	0.35
699.3	6	8	0.37	582.2	6	8	0.38
745.1	4	10	0.29	618.2	4	8	0.31
774.0	2	10	0.30	640.8	2	10	0.30
787.4	0	10	0.30	650.5	0	10	0.31

Table 3 The translational energies of endohedral species A in $A@C_{60}$ from the ground to the first excited state, $\hbar\omega_{01}$. The scaling of V_2^A with respect to $V_2^{\text{H}_2}$ is found using harmonic approximation, $\omega_{\tau} = \omega_{01}$, and eqn (10) where M_A is the mass in atomic mass units, a.u.

A	$\hbar\omega_{01}/\text{cm}^{-1}$	$M_A/\text{a.u.}$	$V_2^A/V_2^{\text{H}_2}$
H_2	179.5 ²³	2	1
^3He	96.7 ⁴¹	3	0.44
^4He	81.3 ⁴¹	4	0.41
HF	78.6 ¹⁶	20	1.92
H_2O	110 ⁴⁹	18	3.4

transition of *para*- $\text{H}_2@C_{60}$ in the $J = 0$ rotational state.^{22,23} Application of pressure changes the relative population of pentagon- and hexagon-oriented molecules.⁵⁷ The analysis of the inelastic neutron scattering spectra of pressure-treated $\text{H}_2@C_{60}$ shows that the potential and the energy levels are sensitive to the orientation of neighboring cages.²⁸ Similar THz and infrared spectroscopy experiments are planned to verify the effect of orientational order on the potential energy function of endohedral molecules and atoms in C_{60} .

In summary, with the THz absorption spectroscopy we have determined the energy level structure of quantized



translational motion of single ^3He and ^4He atoms trapped in the C_{60} molecular cages. The fitted potential energy curves and the induced dipole moments of two isotopes overlap with high precision. However, there are deviations between the modeled and measured spectra. Firstly, the fine structure of spectral lines observed in the low temperature spectra cannot be explained by icosahedral symmetry of C_{60} molecule. Secondly, there are some discrepancies between the measured and modeled spectra in the line intensities and their temperature dependence. Both deviations could be due to the orientational order and the thermal motion of C_{60} molecules in the solid.

Conflicts of interest

There are no conflicts to declare.

Appendix

Fit of anharmonic spherical oscillator and dipole moment parameters

The experimental THz absorption spectrum was fitted using Gaussian line shapes to find the line areas, line widths and frequencies, see Fig. 6. A synthetic experimental spectrum $y(\omega_n)$, the distance between the points in the spectrum $\omega_n - \omega_{n-1} = \Delta\omega/4$, was then generated consisting of lines with equal full width at half maximum, $\Delta\omega = 1.5 \text{ cm}^{-1}$, while keeping the line areas and frequencies of the original experimental lines. The synthetic spectrum approach was needed as the model did not include any line broadening mechanism.

The synthetic spectra were fitted using the anharmonic spherical oscillator model. The reduced basis was limited to

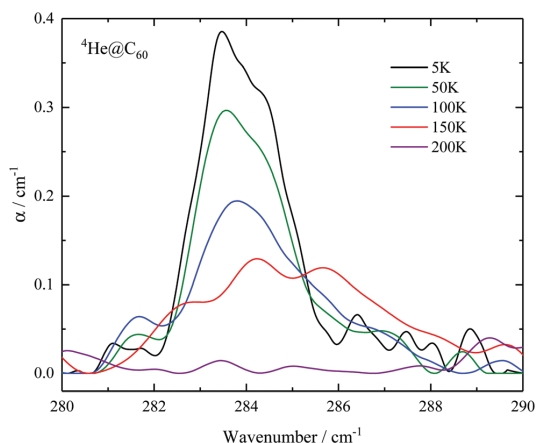


Fig. 7 Temperature dependence of line no. 9 in $^4\text{He@C}_{60}$.

$n_{\text{max}} = 18$ providing 100 states in the reduced basis $|n, \ell\rangle$. For a given model and basis, matrix elements of the Hamiltonian, eqn (1), and the dipole operator, eqn (13), were evaluated analytically in a symbolic form using the Mathematica software. At each step of minimizing chi squared, $\chi^2 = \sum [y - f(\omega_n, \{\kappa\})]^2$, the Hamiltonian was diagonalized numerically. Here $f(\omega_n, \{\kappa\})$ is the theoretical spectrum with the same linewidth and lineshape as the synthetic experimental spectrum; $\{\kappa\} = \{V_2, V_4, V_6, A_1, A_3\}$ is the set of Hamiltonian and dipole operator fit parameters. Errors were calculated using the method described in ref. 49. Adding the V_6 term to V_4 in the potential reduced χ^2 of ^3He and ^4He fit by three and two times, respectively. The frequencies and intensities of experimental spectra and spectra calculated using the best fit parameters are given in Tables 4 and 5.

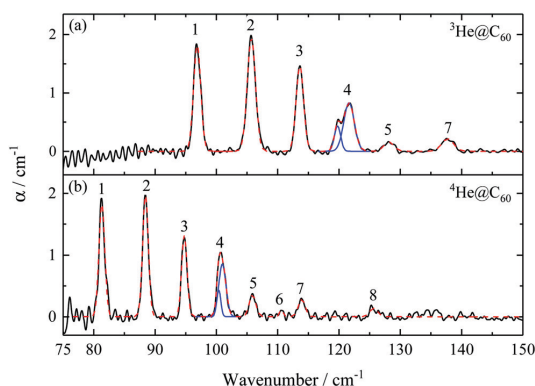


Fig. 6 THz absorption spectrum of ^3He at 125 K (a) and ^4He at 100 K (b), black solid line, and the fit with Gaussian lineshapes, blue solid lines. Red dashed line is the sum of Gaussians. The line intensities are not corrected for the filling factor f_0 , see eqn (14).

Table 4 The line frequencies f and areas S of experimental spectra at 5 and 125 K and the anharmonic spherical oscillator model fit results at 125 K for $^3\text{He@C}_{60}$. The f and S of lines no. 1 and no. 9 at 5 K are calculated using the best fit parameters obtained at 125 K

Line no.	Experiment		Model fit	
	f/cm^{-1}	S/cm^{-2}	f/cm^{-1}	S/cm^{-2}
5 K				
1	96.6	8.5	96.8	11.7
	97.4	2.2	—	—
9	—	—	340.6	0.4
125 K				
1	96.9	2.7	96.8	2.7
2	105.7	3.3	105.7	3.3
3	113.6	2.3	113.7	2.2
4	119.8	0.6	121.0	1.1
	121.6	1.8	121.4	0.8
	—	—	122.4	0.5
5	128.1	0.3	127.8	0.5
	—	—	128.8	0.4
7	137.7	0.5	138.0	0.6



Table 5 The line frequencies f and areas S of experimental spectra at 5 and 100 K and the anharmonic spherical oscillator model fit results at 100 K for $^4\text{He}@C_{60}$. The f and S of lines no. 1 and no. 9 at 5 K are calculated using the best fit parameters obtained at 100 K

Line no.	Experiment		Model fit	
	f/cm^{-1}	S/cm^{-2}	f/cm^{-1}	S/cm^{-2}
5 K				
1	81.2	6.1	81.4	8.0
	81.9	1.2	—	—
	283.3	0.3	283.7	0.3
	284.3	0.4	—	—
100 K				
1	81.3	2.1	81.4	2.0
2	88.4	2.3	88.4	2.4
3	94.8	1.5	94.8	1.5
4	100.4	0.4	100.6	0.7
	101.0	1.3	100.8	0.6
5	—	—	101.6	0.3
	105.9	0.5	106.0	0.3
6	—	—	106.7	0.2
	110.6	0.1	111.0	0.09
7	—	—	111.7	0.10
	113.9	0.4	113.9	0.4
8	—	—	125.9	0.2
	125.7	0.2	125.9	0.2

Acknowledgements

This research was supported by the Estonian Ministry of Education and Research institutional research funding IUT23-3, Estonian Research Council grant PRG736, the European Regional Development Fund project TK134 and by EPSRC-UK, grant numbers EP/P009980/1 and EP/T004320/1.

References

- H. Kroto, J. Heath, S. O'Brien, R. F. Curl and R. E. Smalley, *Nature*, 1985, **318**, 162–163.
- J. R. Heath, S. C. O'Brien, Q. Zhang, Y. Liu, R. F. Curl, F. K. Tittel and R. E. Smalley, *J. Am. Chem. Soc.*, 1985, **107**, 7779–7780.
- M. H. Levitt, *Philos. Trans. R. Soc., A*, 2013, **371**, 20120429.
- Z. Bačić, *J. Chem. Phys.*, 2018, **149**, 100901.
- L. Dunsch and S. Yang, *Small*, 2007, **3**, 1298–1320.
- M. Saunders, H. A. Jiménez-Vázquez, R. J. Cross and R. J. Poreda, *Science*, 1993, **259**, 1428–1430.
- M. Saunders, H. A. Jiménez-Vázquez, R. J. Cross, S. Mroczkowski, M. L. Gross, D. E. Giblin and R. J. Poreda, *J. Am. Chem. Soc.*, 1994, **116**, 2193–2194.
- M. Saunders, R. J. Cross, H. A. Jiménez-Vázquez, R. Shimshi and A. Khong, *Science*, 1996, **271**, 1693–1697.
- T. Weiske, T. Wong, W. Krätschmer, J. K. Terlouw and H. Schwarz, *Angew. Chem., Int. Ed. Engl.*, 1992, **31**, 183–185.
- T. A. Murphy, T. Pawlik, A. Weidinger, M. Höhne, R. Alcalá and J.-M. Spaeth, *Phys. Rev. Lett.*, 1996, **77**, 1075–1078.
- C. Knapp, N. Weiden, H. Kass, K.-P. Dinse, B. Pietzak, M. Waiblinger and A. Weidinger, *Mol. Phys.*, 1998, **95**, 999–1004.
- K. Komatsu, M. Murata and Y. Murata, *Science*, 2005, **307**, 238–240.
- Y. Rubin, T. Jarrosson, G.-W. Wang, M. D. Bartberger, K. N. Houk, G. Schick, M. Saunders and R. J. Cross, *Angew. Chem., Int. Ed.*, 2001, **40**, 1543.
- K. Kurotobi and Y. Murata, *Science*, 2011, **333**, 613–616.
- M. Ge, U. Nagel, D. Hübner, T. Rööm, S. Mamone, M. H. Levitt, M. Carravetta, Y. Murata, K. Komatsu, X. Lei and N. J. Turro, *J. Chem. Phys.*, 2011, **135**, 114511.
- A. Krachmalnicoff, R. Bounds, S. Mamone, S. Alom, M. Conciatrè, B. Meier, K. Kouřil, M. E. Light, M. R. Johnson, S. Rols, A. J. Horsewill, A. Shugai, U. Nagel, T. Rööm, M. Carravetta, M. H. Levitt and R. J. Whitby, *Nat. Chem.*, 2016, **8**, 953–957.
- S. Bloodworth, G. Sitinova, S. Alom, S. Vidal, G. R. Bacanu, S. J. Elliott, M. E. Light, J. M. Herniman, G. J. Langley, M. H. Levitt and R. J. Whitby, *Angew. Chem., Int. Ed.*, 2019, **58**, 1–7.
- S. Bloodworth, G. Hoffman, M. C. Walkey, G. R. Bacanu, J. M. Herniman, M. H. Levitt and R. J. Whitby, *Chem. Commun.*, 2020, **56**, 10521–10524.
- Y. Morinaka, F. Tanabe, M. Murata, Y. Murata and K. Komatsu, *Chem. Commun.*, 2010, **46**, 4532–4534.
- G. Hoffman, M. C. Walkey, J. Gräsvik, G. R. Bacanu, S. Alom, S. Bloodworth, M. E. Light, M. H. Levitt and R. J. Whitby, *Angew. Chem., Int. Ed.*, 2021, **60**, 8960–8966.
- M. Xu, F. Sebastianelli, Z. Bačić, R. Lawler and N. J. Turro, *J. Chem. Phys.*, 2008, **128**, 011101.
- S. Mamone, M. Ge, D. Hübner, U. Nagel, A. Danquigny, F. Cuda, M. C. Grossel, Y. Murata, K. Komatsu, M. H. Levitt, T. Rööm and M. Carravetta, *J. Chem. Phys.*, 2009, **130**, 081103.
- M. Ge, U. Nagel, D. Hübner, T. Rööm, S. Mamone, M. H. Levitt, M. Carravetta, Y. Murata, K. Komatsu, J. Y.-C. Chen and N. J. Turro, *J. Chem. Phys.*, 2011, **134**, 054507.
- T. Rööm, L. Peedu, M. Ge, D. Hübner, U. Nagel, S. Ye, M. Xu, Z. Bačić, S. Mamone, M. H. Levitt, M. Carravetta, J. Chen, X. Lei, N. J. Turro, Y. Murata and K. Komatsu, *Philos. Trans. R. Soc., A*, 2013, **371**, 20110631.
- A. J. Horsewill, K. S. Panesar, S. Rols, M. R. Johnson, Y. Murata, K. Komatsu, S. Mamone, A. Danquigny, F. Cuda, S. Maltsev, M. C. Grossel, M. Carravetta and M. H. Levitt, *Phys. Rev. Lett.*, 2009, **102**, 013001.
- A. J. Horsewill, S. Rols, M. R. Johnson, Y. Murata, M. Murata, K. Komatsu, M. Carravetta, S. Mamone, M. H. Levitt, J. Y.-C. Chen, J. A. Johnson, X. Lei and N. J. Turro, *Phys. Rev. B: Condens. Matter Mater. Phys.*, 2010, **82**, 081410.
- A. J. Horsewill, K. S. Panesar, S. Rols, J. Ollivier, M. R. Johnson, M. Carravetta, S. Mamone, M. H. Levitt, Y. Murata, K. Komatsu, J. Y.-C. Chen, J. A. Johnson, X. Lei and N. J. Turro, *Phys. Rev. B: Condens. Matter Mater. Phys.*, 2012, **85**, 205440.
- S. Mamone, M. R. Johnson, J. Ollivier, S. Rols, M. H. Levitt and A. J. Horsewill, *Phys. Chem. Chem. Phys.*, 2016, **18**, 1998–2005.
- A. L. R. Bug, A. Wilson and G. A. Voth, *J. Phys. Chem.*, 1992, **96**, 7864–7869.
- C. Williams, M. Whitehead and L. Pang, *J. Phys. Chem.*, 1993, **97**, 11652–11656.



- 31 L. Pang and F. Brisse, *J. Phys. Chem.*, 1993, **97**, 8562–8563.
- 32 P. Pyykkö, C. Wang, M. Straka and J. Vaara, *Phys. Chem. Chem. Phys.*, 2007, **9**, 2954–2958.
- 33 C. Wang, M. Straka and P. Pyykkö, *Phys. Chem. Chem. Phys.*, 2010, **12**, 6187–6203.
- 34 F. Cimpoesu, S. Ito, H. Shimotani, H. Takagi and N. Dragoe, *Phys. Chem.*, 2011, **13**, 9609–9615.
- 35 B. Frecus, C. M. Buta, C. I. Oprea, A. Stroppa, M. V. Putz and F. Cimpoesu, *Theor. Chem. Acc.*, 2016, **135**, 133.
- 36 S. Jalife, J. Arcudia, S. Pan and G. Merino, *Chem. Sci.*, 2020, **11**, 6642–6652.
- 37 M. S. Syamala, R. J. Cross and M. Saunders, *J. Am. Chem. Soc.*, 2002, **124**, 6216–6219.
- 38 N. Dragoe, A. M. Flank, P. Lagarde, S. Ito, H. Shimotani and H. Takagi, *Phys. Rev. B: Condens. Matter Mater. Phys.*, 2011, **84**, 155448.
- 39 E. K. Campbell, E. S. Reedy, J. Rademacher, R. J. Whitby and G. Hoffman, *Astrophys. J.*, 2020, **897**, 88.
- 40 S. Patchkovskii and W. Thiel, *J. Chem. Phys.*, 1997, **106**, 1796–1799.
- 41 G. R. Bacanu, T. Jafari, M. Aouane, J. Rantaharju, M. Walkey, G. Hoffman, A. Shugai, U. Nagel, M. Jiménez-Ruiz, A. J. Horsewill, S. Rols, T. Rööm, R. J. Whitby and M. H. Levitt, *J. Chem. Phys.*, 2021, **155**, 144302.
- 42 W. H. Shaffer, *Rev. Mod. Phys.*, 1944, **16**, 245–259.
- 43 S. Flügge, *Practical Quantum Mechanics*, Springer-Verlag, Berlin, 1971, vol. 1.
- 44 C. Cohen-Tannoudji, B. Diu and F. Laloë, *Quantum Mechanics*, John Wiley & Sons, 2005.
- 45 D. A. Varshalovich, A. N. Moskalev and V. K. Khersonskii, *Quantum Theory of Angular Momentum*, World Scientific, 1988.
- 46 R. N. Zare, *Angular Momentum*, John Wiley & Sons, Inc., 1988.
- 47 D. L. Dexter, *Phys. Rev.*, 1956, **101**, 48–55.
- 48 C. C. Homes, P. J. Horoyski, M. L. W. Thewalt and B. P. Clayman, *Phys. Rev. B: Condens. Matter Mater. Phys.*, 1994, **49**, 7052–7055.
- 49 A. Shugai, U. Nagel, Y. Murata, Y. Li, S. Mamone, A. Krachmalnicoff, S. Alom, R. J. Whitby, M. H. Levitt and T. Rööm, *J. Chem. Phys.*, 2021, **154**, 124311.
- 50 B. Meier, S. Mamone, M. Concistrè, J. Alonso-Valdesueiro, A. Krachmalnicoff, R. J. Whitby and M. H. Levitt, *Nat. Commun.*, 2015, **6**, 8112.
- 51 S. L. Altmann and P. Herzog, *Point-Group Theory Tables*, University of Vienna, Vienna, 2nd edn, 2011.
- 52 W. I. F. David, R. M. Ibberson, T. J. S. Dennis, J. P. Hare and K. Prassides, *Europhys. Lett.*, 1992, **18**, 219–225.
- 53 P. A. Heiney, *J. Phys. Chem. Solids*, 1992, **53**, 1333–1352.
- 54 P. M. Felker, V. Vlček, I. Hietanen, S. FitzGerald, D. Neuhauser and Z. Bačić, *Phys. Chem. Chem. Phys.*, 2017, **19**, 31274–31283.
- 55 C. Beduz, M. Carravetta, J. Y.-C. Chen, M. Concistrè, M. Denning, M. Frunzi, A. J. Horsewill, O. G. Johannessen, R. Lawler, X. Lei, M. H. Levitt, Y. Li, S. Mamone, Y. Murata, U. Nagel, T. Nishida, J. Ollivier, S. Rols, T. Rööm, R. Sarkar, N. J. Turro and Y. Yang, *Proc. Natl. Acad. Sci. U. S. A.*, 2012, **109**, 12894–12898.
- 56 K. S. K. Goh, M. Jimenez-Ruiz, M. R. Johnson, S. Rols, J. Ollivier, M. S. Denning, S. Mamone, M. H. Levitt, X. Lei, Y. Li, N. J. Turro, Y. Murata and A. J. Horsewill, *Phys. Chem. Chem. Phys.*, 2014, **16**, 21330–21339.
- 57 B. Sundqvist, *Adv. Phys.*, 1999, **48**, 1–134.



Appendix 3

3

T. Jafari, A. Shugai, U. Nagel, G. R. Bacanu, M. Aouane, M. Jiménez-Ruiz, S. Rols, S. Bloodworth M. Walkey, G. Hoffman, R. J. Whitby, M. H. Levitt, and T. Rõõm, "Ne, Ar, and Kr oscillators in the molecular cavity of fullerene C₆₀," *J. Chem. Phys*, vol. 158, p. 234305, June 2023

RESEARCH ARTICLE | JUNE 20 2023

Ne, Ar, and Kr oscillators in the molecular cavity of fullerene

C₆₀ 

Tanzeeha Jafari ; Anna Shugai ; Urmaz Nagel ; George Razvan Bacanu ; Mohamed Aouane ; Monica Jiménez-Ruiz ; Stéphane Rols ; Sally Bloodworth ; Mark Walkey ; Gabriela Hoffman ; Richard J. Whitby ; Malcolm H. Levitt ; Toomas Rõõm

 Check for updates

J. Chem. Phys. 158, 234305 (2023)

<https://doi.org/10.1063/5.0152628>



View
Online



Export
Citation

CrossMark



The Journal of Chemical Physics

Special Topic: Adhesion and Friction

Submit Today!

 AIP
Publishing

 AIP
Publishing

Ne, Ar, and Kr oscillators in the molecular cavity of fullerene C₆₀

Cite as: J. Chem. Phys. 158, 234305 (2023); doi: 10.1063/5.0152628

Submitted: 31 March 2023 • Accepted: 5 June 2023 •

Published Online: 20 June 2023



Tanzeeha Jafari,¹ Anna Shugai,¹ Urmaz Nagel,¹ George Razvan Bacanu,² Mohamed Aouane,³ Monica Jiménez-Ruiz,³ Stéphane Rols,³ Sally Bloodworth,² Mark Walkey,² Gabriela Hoffman,² Richard J. Whitby,² Malcolm H. Levitt,² and Toomas Rõõm^{1,a)}

AFFILIATIONS

¹National Institute of Chemical Physics and Biophysics, Tallinn 12618, Estonia

²School of Chemistry, University of Southampton, Southampton SO17 1BJ, United Kingdom

³Institut Laue-Langevin, BP 156, 38042 Grenoble, France

^{a)}Author to whom correspondence should be addressed: toomas.room@kbfi.ee

ABSTRACT

We used THz (terahertz) and INS (inelastic neutron scattering) spectroscopies to study the interaction between an endohedral noble gas atom and the C₆₀ molecular cage. The THz absorption spectra of powdered A@C₆₀ samples (A = Ar, Ne, Kr) were measured in the energy range from 0.6 to 75 meV for a series of temperatures between 5 and 300 K. The INS measurements were carried out at liquid helium temperature in the energy transfer range from 0.78 to 54.6 meV. The THz spectra are dominated by one line, between 7 and 12 meV, at low temperatures for three noble gas atoms studied. The line shifts to higher energy and broadens as the temperature is increased. Using a spherical oscillator model, with a temperature-independent parameterized potential function and an atom-displacement-induced dipole moment, we show that the change of the THz spectrum shape with temperature is caused by the anharmonicity of the potential function. We find good agreement between experimentally determined potential energy functions and functions calculated with Lennard-Jones additive pair-wise potentials with parameters taken from the work of Pang and Brisse, J. Chem. Phys. 97, 8562 (1993).

© 2023 Author(s). All article content, except where otherwise noted, is licensed under a Creative Commons Attribution (CC BY) license (<http://creativecommons.org/licenses/by/4.0/>). <https://doi.org/10.1063/5.0152628>

I. INTRODUCTION

Endofullerenes are a class of supramolecular complexes where atoms or molecules, A, are confined inside the C₆₀ molecular cage, represented as A@C₆₀. An effective method to synthesize endofullerenes in milligram quantities was introduced by Komatsu and co-workers in 2005.¹ They successfully enclosed single H₂ molecules in C₆₀ cages after a series of organic synthesis steps known as “molecular surgery.” Over the years, the list of endofullerenes produced by molecular surgery² has been supplemented by H₂O@C₆₀,³ HF@C₆₀,⁴ CH₄@C₆₀,⁵ and noble gas endofullerenes.^{6–8}

Endofullerenes give an opportunity to study non-covalent interactions between the guest and the molecular cage of C₆₀. The confining potential quantizes the translational motion of the guest. In the case of confined molecules, there are additional degrees of rotational and vibrational freedom, which complicate the energy spectrum of A@C₆₀. The monatomic noble gas endofullerenes, on

the other hand, are relatively simple systems with only translational degrees of freedom.

Since the discovery of noble gas endofullerenes in the early 1990s by mass spectroscopy,⁹ they have been studied using a variety of techniques, such as infrared or THz (terahertz) absorption spectroscopy,^{10,11} INS (inelastic neutron scattering),¹¹ NMR (nuclear magnetic resonance),^{6,8,12,13} and others.^{14,15} In the work of Takeda *et al.*,¹² the influence of the inserted atom on the lattice parameters was revealed for Ar@C₆₀. The ¹³C chemical shift of the C₆₀ cage carbon atoms shows downfield shifts of 0.027, 0.17, 0.39, and 0.95 ppm in He@C₆₀,¹³ Ar@C₆₀,¹² Kr@C₆₀,^{8,16} and Xe@C₆₀,¹⁷ respectively. This trend consisted in the greater interaction of the endohedral atom with fullerene electrons as the size of the guest atom increases. Frunzi *et al.*¹⁸ even concluded that the xenon atom pushes the fullerene electrons outward. The first experimental evidence of confinement-induced internuclear J-coupling was reported by Bacanu *et al.*¹³ in ³He@C₆₀.

Several theoretical approximations have been made to calculate the potential energy function of a noble gas atom in the fullerene cage.^{11,19–24} One approach to model dispersive interactions between atoms is to use a superposition of Lennard-Jones (LJ) 6-12 potentials. The molecular dynamics of Ne inside C_{60} was reported by Bug *et al.*²⁵ where the LJ potential was employed to describe the C–Ne interaction within the flexible cage of C_{60} . The translational frequency of Ne@ C_{60} was predicted at 90 cm^{-1} . Pang and Brisse¹⁹ calculated endohedral energies of He, Ne, Kr, Ar, and Xe inside C_{60} and C_{70} using LJ functions. They concluded that He and Ne form more stable complexes with C_{60} due to their smaller van der Waals radii as compared to larger Ar, Kr, and Xe. The potential function of He in C_{60} calculated by Pang and Brisse reproduces the recently spectroscopically determined potential function remarkably well.¹¹ However, there have been no experimental data for the potential functions of other noble gas atoms in C_{60} .

This paper is a continuation of our previous work on He@ C_{60} .^{11,24} Here, we report a study of Ne, Ar, and Kr endofullerenes by THz spectroscopy and INS. Although the center-of-mass motion of a neutral atom in free space does not interact with electromagnetic radiation, atoms acquire an induced electric dipole moment upon their interaction with C_{60} , allowing for the oscillatory center-of-mass motion of an endohedral atom to absorb THz radiation. We report both THz and INS data for Ne@ C_{60} . However, in the case of Ar@ C_{60} and Kr@ C_{60} , only the THz data are presented since the difficulties in the synthesis precluded the production of sufficient samples for INS, in these cases.

In the case of an anharmonic potential, the distance between consecutive energy levels changes as the energy increases. This leads to a “comb” of well-resolved THz absorption peaks at temperatures high enough to populate excited transitional states. Such THz “combs” were prominent in the case of He endofullerenes, where the confining potential is highly anharmonic.¹⁰ In contrast, “combs” of THz peaks were not observed for Ar, Ne, and Kr endofullerenes. As discussed below, this is because the confining potential is much more harmonic than for He.

To study the anharmonicity of the interaction potential, THz absorption spectra were measured over a wide temperature range from 5 to 300 K. The INS spectra were acquired for Ne@ C_{60} at low temperature. The interaction potential parameters were determined by fitting the experimental spectra to a spherical anharmonic oscillator model. Finally, the experimentally derived potential functions were compared with predictions using the LJ two-body potential parameters of Pang and Brisse.¹⁹

II. MATERIALS AND METHODS

A. Sample preparation

Endofullerenes containing Ne, Ar, and Kr atoms were synthesized by multi-step “molecular surgery.” The shell of C_{60} is chemically opened to create an orifice. The orifice should be of proper size to allow for the entering of a guest atom and at the same time to prevent its quick loss. An open-cage intermediate fullerene incorporating atom is closed with a sequence of chemical reactions. Ar@ C_{60} and Kr@ C_{60} ^{6,8} were made using a similar sequence of chemical reactions for the contraction and the closure of the open-cage endofullerene orifice. For Ne@ C_{60} , the open-cage fullerene was filled by Ne gas in the solid state and the Ne atom was trapped through the solid-state

Wittig reaction induced by raising the temperature.⁷ It was found that traces of a $H_2O@C_{60}$ impurity interfered with INS measurements due to the strong incoherent scattering of water protons. This impurity was removed from the Ne@ C_{60} sample by extensive HPLC (high-performance liquid chromatography). To improve the signal-to-noise ratio of THz spectroscopy, the filling factor of the samples was further increased by extensive recirculating HPLC. The achieved filling factors f (defined as the fraction of C_{60} cages containing an endohedral guest) are given below. All samples were sublimed under vacuum before spectroscopic measurements.

B. Terahertz spectroscopy

The powdered samples of A@ C_{60} were pressed under vacuum into 3 mm diameter pellets to perform THz measurements. The pellet thicknesses of Ne@ C_{60} , Ar@ C_{60} , and Kr@ C_{60} were 1.61, 1.06, and 0.95 mm, and the filling factors were 0.99, 1.0, and 1.0. The sample masses were estimated to be 21.5, 13.2, and 12.3 mg for Ne@ C_{60} , Ar@ C_{60} , and Kr@ C_{60} , respectively.

The transmission spectra of Ar@ C_{60} and Kr@ C_{60} were recorded using a vacuum FTIR Bruker spectrometer (Vertex 80v). A standard far-infrared setup covering the range from 10 to 600 cm^{-1} was used for the measurements: an electrically heated SiC (Glo-bar) radiation source, a $6\text{ }\mu\text{m}$ thick Mylar beam splitter, and a 4 K bolometer for detection. In order to reach low temperatures, a compact cold-finger continuous flow cryostat was used. The required temperature within the cryostat was maintained by controlling the flow of helium and by using the heater. To register the transmission spectra, the cryostat insert with the cold finger moves up and down, allowing the signal to pass through the sample or through a 3 mm diameter hole as a reference channel. The sample channel was equipped with a sample cell with two polypropylene windows that kept the sample in an atmosphere of helium exchange gas. This technique allowed for good thermal contact between the cold-finger and the pellet.

The Ne@ C_{60} spectra were measured from 5 up to 100 cm^{-1} using a Martin–Puplett interferometer equipped with a high-pressure Hg lamp as a radiation source. The chamber of the ^3He cooled bolometer (working temperature $T = 0.3\text{ K}$) and the sample chamber were immersed in a liquid helium bath. The sample and reference hole shared the same He heat exchange gas environment. The sample temperature T was controlled by the heater and the exchange gas pressure. The resolution used on both instruments was 0.3 cm^{-1} , which is less than the linewidth of the measured absorption lines for the studied samples. The calculations of the THz absorption spectra of A@ C_{60} and the baseline corrections are described in the supplementary material.

C. Inelastic neutron scattering

INS experiments were conducted using the IN1–Lagrange spectrometer at the Institut Laue–Langevin (ILL) in Grenoble. Incident neutrons are provided by the “hot source” moderator of the reactor, resulting in a high flux neutron beam. Selection of three different single crystal monochromators, namely, Si(111), Si(311), and Cu(220), enables selection of the incident energy of the monochromatic neutron beam arriving at the sample by using Bragg reflection. The neutrons scattered by the sample enter a secondary spectrometer comprising a large area array of pyrolytic graphite analyzer

crystals. The focusing geometry of the secondary spectrometer ensures that only neutrons with a fixed kinetic energy of 4.5 meV are detected by using the ^3He detector. INS spectra were recorded in the energy transfer range from 0.78 to 54.6 meV. The 170 mg $\text{Ne}@C_{60}$ powder, $f = 0.7$, was wrapped in a thin aluminum pocket and attached to the tip of the cryostat. The $\text{Ne}@C_{60}$ spectra were corrected for the scattering from the aluminum foil and from C_{60} (supplementary material).

D. Model and parameter fitting

The details of the spherical oscillator model of an atom encapsulated by C_{60} can be found in Refs. 11 and 24. Here, we highlight the key aspects. C_{60} is treated as a rigid body with a fixed center of mass. This excludes temperature effects on the confining potential caused by C_{60} molecular vibrations, crystal lattice modes, and crystal lattice thermal expansion. In principle, the confining potential inherits icosahedral symmetry from the symmetry of the fullerene cage. For simplicity, we neglect the deviations from spherical symmetry and expand the spherically symmetrical potential in even powers of r , defined as the displacement of the endohedral atom from the cage center,

$$\hat{V}(r) = \sum_{k=2}^{\infty} V_k r^k. \quad (1)$$

The harmonic spherical oscillator Hamiltonian,

$$\hat{H} = -\frac{\hat{p}^2}{2m} + V_2 r^2, \quad (2)$$

has been solved analytically,²⁶ p and m are the momentum and mass of the atom. The radial quantum number n and the orbital quantum number ℓ characterize the eigenstates and eigenvalues (energy levels) of the Hamiltonian (2), where ℓ takes even values from 0 to n for even n and odd values from 1 to n for odd n . The energies of a harmonic spherical oscillator are given by $E_{n\ell} = \hbar\omega_0(n + 3/2)$ and $\omega_0 = \sqrt{2V_2/m}$. The Hamiltonian including anharmonic terms V_k , $k > 2$, is diagonalized numerically using a finite-size basis of the harmonic Hamiltonian eigenstates. Here, we used eigenstates up to the quantum number $n_{\text{max}} = 18$. Because the potential is approximated as being spherical, there is no mixing of states with different ℓ values and the energy levels remain $(2\ell + 1)$ -fold degenerate.

To fit the THz absorption line intensities of translational transitions, we assume that the dipole moment is induced by the displacement of an atom from the C_{60} cage center, $\mathbf{r} = (r, \phi, \theta)$, as expressed in spherical coordinates. As discussed in Ref. 24, the displacement-induced electric dipole moment may be expressed in terms of rank-1 spherical harmonics as follows:

$$d_{1q} = \sqrt{\frac{4\pi}{3}} \sum_{p=1}^{\infty} A_{pq} r^p Y_{1q}(\theta, \phi), \quad (3)$$

where A_{pq} is the dipole amplitude coefficient and $q \in \{-1, 0, +1\}$. Within the approximation of spherical symmetry, A_{pq} is independent of q , $A_{pq} = A_p$. Furthermore, since the dipole moment is a polar vector, only odd powers of r are involved, i.e., $p \in \{1, 3, \dots\}$. For the atoms studied here, it was found that the terms linear in r (i.e., $p = 1$) are sufficient. Cubic and higher-order terms were ignored

in the fit. The selection rule for transitions between the spherical oscillator levels induced by the electric field coupled to the dipole moment, Eq. (3), linear in r is $\Delta\ell = \pm 1$ and $\Delta n = \pm 1$.²⁴ The relationship between the THz absorption coefficients and the matrix elements of the induced dipole moment, including the thermal populations of the oscillator levels, is given in Ref. 24.

The fitted parameters, $\{V_2, V_4, A_1\}$, are found by minimizing the difference-squared of the calculated spectrum and the baseline-corrected experimental spectrum. In the cases where there is more than one isotope, the diagonalization and the dipole matrix calculation are carried out separately for each mass. The spectra of isotopes are added using the natural abundances as weighting factors. The minimization is done simultaneously over several temperatures assuming temperature-independent linewidths of the calculated peaks. Parameter confidence limits are calculated using the method described in Ref. 27.

E. Potential energy functions from the Lennard-Jones model

The Lennard-Jones (LJ) 6-12 potential describes the interaction energy between two atoms as a function of their distance of separation with two empirical parameters; see, e.g., Ref. 21. In the case of $A@C_{60}$, the potential energy function for the A atom is calculated by displacing atom A from the center of the fullerene cage by r and summing over sixty A - C two-body interactions for each position r . LJ confining potentials given in this article are obtained by moving the noble gas atom toward the center of a HH bond (the bond in between two hexagons). As shown in the supplementary material, the direction of the displacement of the atom from the center of the cage has very little effect on the potential. As reported in Ref. 11, the positions of the C_{60} atoms were fixed to the best known values as calculated from the neutron scattering data.²⁸ The given structural parameters are $r_0 = 354.7 \pm 0.5$ pm, the distance of all carbon nuclei from the center of the cage; $h = 138 \pm 0.27$ pm, the bond length that joins hexagonal C_6 rings; and $p = 145.97 \pm 0.18$ pm, the bond length that joins C_6 and pentagonal C_5 rings. The parameters of Pang and Brisse,¹⁹ corrected by Jiménez-Vázquez and Cross,²¹ were used for all LJ potentials.

III. RESULTS

A. $\text{Ne}@C_{60}$

$\text{Ne}@C_{60}$ absorption spectra are shown as a function of temperature in Fig. 1. At 3 K, we see a strong peak at 56.6 cm^{-1} , which according to our model calculation is the transition from the ground state $n = 0$ to the first excited translational state $n = 1$; see Table II. The shape of this main line at 3 K is described by a Lorentzian function, with 0.5 cm^{-1} full width at half maximum (FWHM).

The position of the main peak changes when T increases from 3 to 40 K (see the inset of Fig. 1) and also the line broadens. The absorption spectrum continues to shift and broaden at higher temperatures, as shown in Fig. 1. This effect is attributed to the increasing population of higher translational states at higher temperatures, combined with the significant anharmonicity of the potential. Because our model does not explain the temperature dependence observed below 30 K, the spectra measured at following T were used to fit the potential and dipole moment parameters: 30, 40, 50, 60, 70,

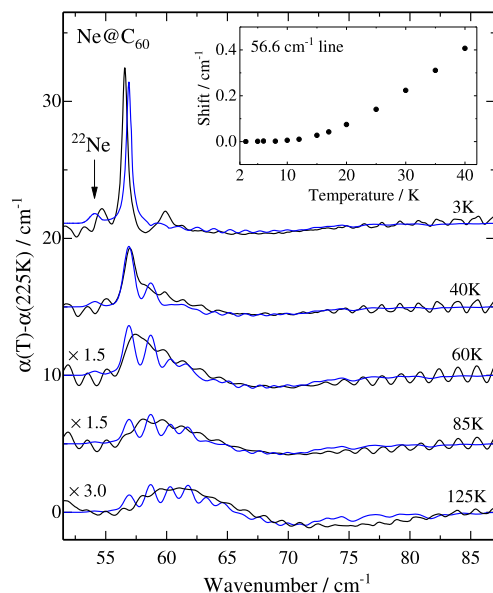


FIG. 1. THz differential absorption spectra of Ne@C₆₀ at different temperatures (black) and the differential spectra calculated with the best fit parameters from Table I (blue). The line shape is assumed to be Lorentzian at 3 K (FWHM = 0.5 cm⁻¹) and Gaussian (FWHM = 1.0 cm⁻¹) for temperatures of 40 K and higher. The intensities of the 60, 85, and 125 K differential spectra have been multiplied by factors of 1.5 and 3. The inset shows the temperature dependence of the main peak frequency shift, $\omega_{01}(T) - \omega_{01}(3\text{ K})$, between 3 and 40 K.

85, 100, 125, 150, and 175 K. For the model fitting, these spectra were referenced to the 225 K spectrum. Similarly, the spectra calculated with the model parameters were referenced to the model spectrum at 225 K. The difference spectra, $\alpha(T) - \alpha(225\text{ K})$, calculated with the best fit model parameters, given in Table I, are plotted in Fig. 1. The oscillations seen in the calculated spectra are individual lines

resolved by FWHM = 1.0 cm⁻¹ used for plotting. The ²²Ne peak, natural abundance 9.3%,²⁹ is clearly seen on the lower frequency side of the main ²⁰Ne peak in the calculated spectra. The ²²Ne peak is obscured in the experimental spectra by baseline artifacts associated with the subtraction of spectra taken at widely different temperatures, Fig. 1. This peak is more visible in the $\alpha(T) - \alpha(100\text{ K})$ difference spectra; see Fig. S5 of the supplementary material. However, its frequency differs slightly from the anticipated isotope shift; see Sec. IV.

The low *T* INS spectrum of Ne@C₆₀ is plotted in Fig. 2. The peak at 7 meV and the THz peak at 56.6 cm⁻¹ coincide well within the width of the INS peak. Although there is a peak in the INS spectrum at 13 meV, its energy is too low to be assigned to the *n* = 0 → *n* = 2 transition. Other two peaks above 13 meV, coinciding with *n* = 0 → *n* = 2 transitions, are too weak compared to the noise to be assigned to Ne@C₆₀ transitions (supplementary material).

B. Ar@C₆₀

The temperature-dependence of the THz absorption spectra of Ar@C₆₀ is shown in Fig. 3. The 5 K spectrum displays one sharp peak at 91.9 cm⁻¹. The shape of the peak up to 50 K is best described by a Lorentzian line shape with FWHM = 0.5 cm⁻¹. As the temperature increases, the absorption peak broadens and its maximum shifts to higher frequency. This is due to the increasing population of higher translational states at higher temperatures, combined with the significant anharmonicity of the potential. The experimental spectra were fitted at 5, 10, 20, 30, 40, 50, 60, 80, 100, 140, 180, 220, 250, 270, and 300 K using the Lorentzian shape with FWHM = 0.5 cm⁻¹. The spectra calculated with the best fit parameters from Table I and plotted in Fig. 3 show that the experimentally observed *T* dependence of the spectrum is well described by an anharmonic potential.

C. Kr@C₆₀

Unlike Ne@C₆₀ and Ar@C₆₀, the Kr@C₆₀ spectrum shows a broad asymmetrical absorption line even at 5 K, Fig. 4. At higher temperatures, the Kr@C₆₀ spectrum broadens further and its maximum shifts to higher frequency, similar to the behavior of Ne and Ar. The fit of the experimental absorption spectra of Kr@C₆₀ was done at temperatures of 5, 40, 80, 120, 160, 200, 240, 280, and 310 K

TABLE I. Best fit polynomial coefficients and confidence limits for the radial potential function $V(r) = V_2r^2 + V_4r^4 + V_6r^6$ and induced dipole function $d_{1q} = (4\pi/3)^{1/2}(A_1r + A_3r^3)Y_{1q}(\theta, \phi)$ of the confined atoms. ω_{01} is the peak frequency of the absorption line at 5 K in the measured THz spectrum corresponding to the *n* = 0 → *n* = 1 transition. $v_{\text{anh}} = (\omega_{01} - \omega_0)/\omega_{01}$ is the fractional contribution of the anharmonic potential to ω_{01} , where $\omega_0 = \sqrt{2V_2/m}$ is the frequency of the harmonic oscillator, *m* is the mass of the endohedral atom, and *c* is the speed of light in vacuum. The ⁴He@C₆₀ data are from Ref. 24.

Parameter	⁴ He	²⁰ Ne	⁴⁰ Ar	⁸⁴ Kr
V_2 (J m ⁻²)	0.39 ± 0.006	1.58 ± 0.04	9.56 ± 0.03	17.81 ± 0.12
V_4 (J m ⁻⁴)	(0.60 ± 0.01) × 10 ²⁰	(2.28 ± 0.22) × 10 ²⁰	(8.19 ± 0.16) × 10 ²⁰	(13.2 ± 1.60) × 10 ²⁰
V_6 (J m ⁻⁶)	(3.94 ± 0.09) × 10 ³⁹	0	0	0
A_1 (C)	(0.68 ± 0.04) × 10 ⁻²¹	(1.84 ± 0.13) × 10 ⁻²¹	(3.31 ± 0.01) × 10 ⁻²¹	(3.30 ± 0.21) × 10 ⁻²¹
A_3 (Cm ⁻²)	0.04 ± 0.01	0	0	0
$(2\pi c)^{-1}\omega_{01}$ (cm ⁻¹)	81.4	56.6	91.8	85.4
v_{anh}	0.29	0.085	0.018	0.007

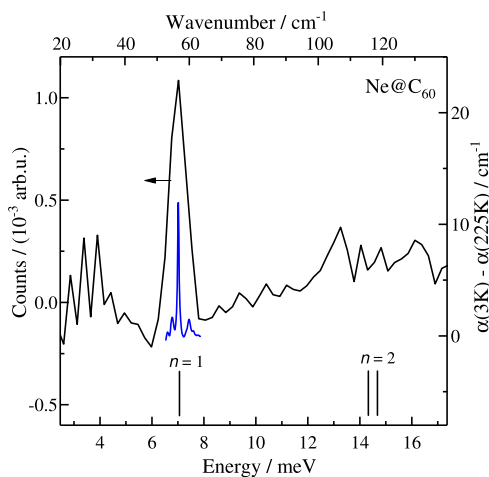


FIG. 2. INS spectrum of Ne@C₆₀ at 2.7 K (black). The INS signal of empty C₆₀ is subtracted. Sticks denote the predicted energies of the transitions from the ground state $n = 0$ to the first ($n = 1, \ell = 1$) and to the second translational level ($n = 2, \ell = 2$, and $\ell = 0$), Table II, calculated from the anharmonic oscillator model using the best fit parameters of the THz absorption spectra, Table I. The THz spectrum at 3 K is plotted for comparison, blue line.

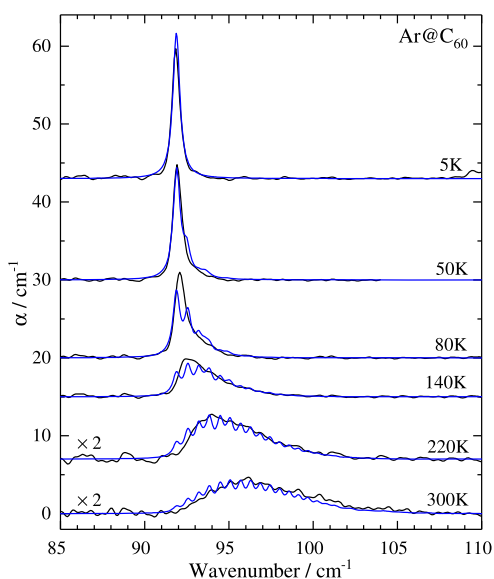


FIG. 3. THz absorption spectra of Ar@C₆₀ at different temperatures (black) and the spectra calculated with the best fit parameters from Table I and plotted with a Lorentzian line shape, FWHM = 0.5 cm⁻¹ (blue). The 220 and 300 K spectra are multiplied by a factor of 2.

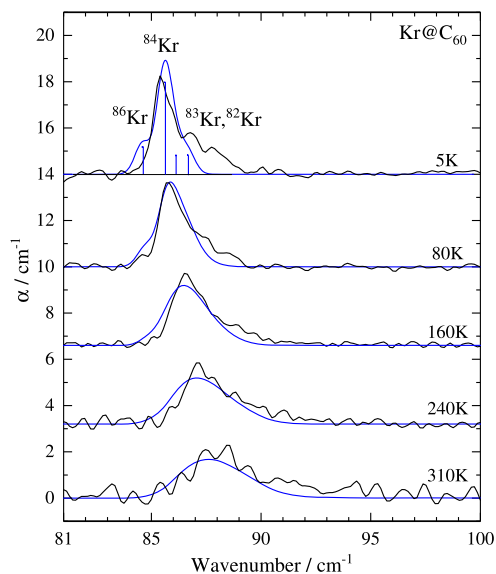


FIG. 4. THz absorption spectra of Kr@C₆₀ at different temperatures (black) and the spectra calculated with the best fit parameters from Table I and plotted using a Gaussian line shape with FWHM = 0.8 cm⁻¹ (blue). The simulated spectra for the four most abundant isotopes are included, weighted by their natural abundances. The sticks indicate the isotopic composition of the 5 K spectrum.

with FWHM = 0.8 cm⁻¹ for all isotopes. The spectra calculated with the best fit parameters from Table I are plotted in Fig. 4. Compared to Ne and Ar, the calculated spectra of Kr do not show oscillations because first the spread of line frequencies in the high temperature spectra is less for Kr@C₆₀ due to a smaller anharmonicity and second the FWHM of individual lines is larger in the calculated spectra of Kr@C₆₀. The asymmetric line shape at 5 K is partially caused by the isotope distribution of Kr: ⁸²Kr – 11.6%, ⁸³Kr – 11.5%, ⁸⁴Kr – 57%, and ⁸⁶Kr – 17.3%, counting the four most abundant isotopes.²⁹ The model predicts extra absorption on both sides of the most abundant isotope peak at 5 K but does not account for all absorption on the higher frequency side of that peak, as discussed in Sec. IV.

IV. DISCUSSION

The spherical oscillator parameters that provide the best match to the experimental THz spectra, and their confidence limits, are summarized in Table I. In all cases, the anharmonic terms V_4 are positive, which means that the separation between the energy levels increases with the increasing energy. Unlike the highly anharmonic case of He@C₆₀ (see the fractional anharmonicity ν_{anh} in Table I), for which the transitions from different starting levels are resolved in the THz spectrum at high temperature, the transitions for Ne, Ar, and Kr merge into one broad line. Since the separation between the energy levels increases with the increasing energy, this broad spectral line shifts to higher energy with the increasing temperature as

TABLE II. Translational energy levels of $^{20}\text{Ne}@C_{60}$, $^{40}\text{Ar}@C_{60}$, and $^{84}\text{Kr}@C_{60}$ calculated with the parameters given in Table I, which provide the best correspondence between the THz absorption spectra and the anharmonic spherical oscillator model. The columns gives the translational energy E , the angular momentum quantum number ℓ (single-valued for each energy level), and the amplitude-squared $|\xi_n|^2$ of the main component of the eigenstate with the principal quantum number n . The tabulated energies are relative to the zero-point energies, which are as follows: 81.75 cm^{-1} for $^{20}\text{Ne}@C_{60}$, 136.52 cm^{-1} for $^{40}\text{Ar}@C_{60}$, and 127.86 cm^{-1} for $^{84}\text{Kr}@C_{60}$.

$^{20}\text{Ne}@C_{60}$				$^{40}\text{Ar}@C_{60}$				$^{84}\text{Kr}@C_{60}$			
$E\text{ (cm}^{-1}\text{)}$	n	ℓ	$ \xi_n ^2$	$E\text{ (cm}^{-1}\text{)}$	n	ℓ	$ \xi_n ^2$	$E\text{ (cm}^{-1}\text{)}$	n	ℓ	$ \xi_n ^2$
0	0	0	1.0	0	0	0	1.0	0	0	0	1.0
56.9	1	1	0.99	91.9	1	1	1.0	85.6	1	1	1.0
115.6	2	2	0.98	184.4	2	2	1.0	171.5	2	2	1.0
118.4	2	0	0.97	185.4	2	0	1.0	171.9	2	0	1.0
175.9	3	3	0.96	277.6	3	3	1.0	257.7	3	3	1.0
180.3	3	1	0.93	279.3	3	1	1.0	258.4	3	1	1.0
237.7	4	4	0.94	371.5	4	4	1.0	344.1	4	4	1.0
243.5	4	2	0.89	373.8	4	2	0.99	345.1	4	2	1.0
246.0	4	0	0.87	374.8	4	0	0.99	345.6	4	0	1.0
301.0	5	5	0.92	466.0	5	5	1.0	430.9	5	5	1.0
308.1	5	3	0.89	468.9	5	3	0.99	432.2	5	3	1.0
312.0	5	1	0.79	470.5	5	1	0.99	432.9	5	1	1.0
365.6	6	6	0.89	561.1	6	6	0.99	517.9	6	6	1.0
373.9	6	4	0.77	564.6	6	4	0.98	519.5	6	4	1.0
379.2	6	2	0.70	566.8	6	2	0.98	520.5	6	2	1.0
381.4	6	0	0.67	567.8	6	0	0.98	520.9	6	0	1.0
431.5	7	7	0.86	656.8	7	7	0.99	605.2	7	7	1.0
440.8	7	5	0.70	660.9	7	5	0.98	607.0	7	5	1.0
447.4	7	3	0.60	663.7	7	3	0.97	608.3	7	3	0.99
451.0	7	1	0.56	665.3	7	1	0.97	609.0	7	1	0.99
498.6	8	8	0.82	753.1	8	8	0.99	692.8	8	8	1.0
509.0	8	6	0.62	757.8	8	6	0.97	694.9	8	6	0.99
516.7	8	4	0.50	761.2	8	4	0.96	696.4	8	4	0.99
521.6	8	2	0.43	763.4	8	2	0.95	697.4	8	2	0.99
523.7	8	0	0.41	764.3	8	0	0.95	697.8	8	0	0.99
566.9	9	9	0.79	850.0	9	9	0.98	780.6	9	9	1.0
578.2	9	7	0.40	855.2	9	7	0.96	783.0	9	7	0.99
587.0	9	5	0.40	859.2	9	5	0.94	784.8	9	5	0.99
593.1	11	3	0.39	862.0	9	3	0.93	786.0	9	3	0.98
596.5	11	1	0.4	863.6	9	1	0.93	786.7	9	1	0.98

observed for Ne, Ar, and Kr. The anharmonic term of the potential, V_4 , mixes states with different n but the same ℓ in the approximation of spherical symmetry. The amplitude squared, $|\xi_n|^2$, of the dominant harmonic oscillator state with the principal quantum number n is given in Table II. In the case of Ne, the $|\xi_n|^2$ factor decreases as n increases, reflecting the significant anharmonicity of the potential, which mixes states with different n quantum numbers. For Kr, on the other hand, there is little mixing, which corresponds to a low level of anharmonicity. The behavior of Ar is intermediate.

In Fig. 5, we compare the best-fit anharmonic interaction potentials $V(r)$ with the potentials derived by a summation of LJ two-body terms using the parameters of Pang and Brisse.¹⁹ The best-fit anharmonic oscillator potential and the LJ potential agree best for the case of Ne@C₆₀. Other atoms show minor discrepancies between the best-fit anharmonic oscillator potential and the LJ potential curves. In general, the LJ potentials with parameters from Pang and Brisse¹⁹ agree surprisingly well with the experimental data,

especially considering the delocalized electronic structure of C₆₀. As can be seen in Fig. 5, the potential curves become increasingly steep when going from He to Kr, which is consistent with the larger size of the atoms.

Despite the overall good agreement between the theoretical model and the experimental data, some discrepancies remain. These include the following: (1) An anomalous temperature-dependent shift of the main THz absorption peak of Ne@C₆₀ at temperatures below 30 K is seen, Fig. 1 (inset). This low-temperature frequency shift is not predicted by the theoretical model, in contrast to the behavior at higher temperatures, which does appear to be well-predicted. (2) In some cases, the difference in translational frequency for isotopes of different masses is not in full agreement with theoretical expectations. This is the case for the ²²Ne and ²⁰Ne peaks, Fig. 1. (3) In some cases, an additional structure is observed above the main THz absorption peak frequency, e.g., a peak at 60 cm⁻¹ in the Ne@C₆₀ spectrum, Fig. 1. Although we do not have a full explanation

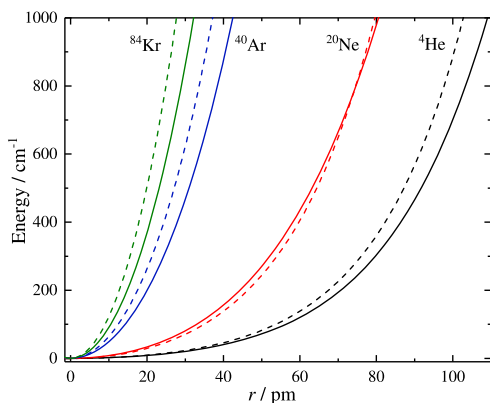


FIG. 5. Comparison of the experimentally determined potential functions $V(r)$ and the LJ potential functions of ${}^4\text{He}@C_{60}$, ${}^{20}\text{Ne}@C_{60}$, ${}^{40}\text{Ar}@C_{60}$, and ${}^{84}\text{Kr}@C_{60}$. Solid lines: Potential energy curves for the anharmonic spherical oscillator model, with parameters given in Table I, which provide the best fit to the experimental data. Dashed lines: Potential energy curves obtained by summing Lennard-Jones two-body potentials, with parameters given in Ref. 19.

of all of these features, the following factors may be considered: (1) Temperature-dependent phase transitions and lattice parameters for crystalline C_{60} . (2) Merohedral disorder. (3) Interference between the translational modes of the endohedral atom and inter-molecular lattice modes.

Crystalline C_{60} has a first-order phase transition from the face-centered cubic phase above 260 K to a simple cubic structure below 260 K.³⁰ The lattice constant decreases gradually with temperature with a jump at 260 K and a small kink at about 90 K. Below 90 K, there is a frozen-in merohedral disorder. The two orientations, named hexagonal and pentagonal, are distinguished by the relative orientation of the central cage and its 12 nearest-neighbor C_{60} molecules. About 85% of C_{60} molecules have their electron-rich double bond facing the pentagonal face and 15% have the same bond facing the hexagonal face of a neighboring molecule.^{30,31}

The phonon density of states has a gap between ~ 70 and 240 cm^{-1} .³² The phonons below 70 cm^{-1} have mainly inter-molecular character, and those above 240 cm^{-1} have mainly intra-molecular character.

The anomalous temperature-dependent shift of the main THz absorption peak of $\text{Ne}@C_{60}$ at temperatures below 30 K might be associated with the interference between the translational modes of the endohedral atom and inter-molecular lattice modes. The low-temperature shift is not observed for helium²⁴ nor for argon, Fig. 3, which is consistent with the observation that the translational frequencies of these two atoms are above the density of states of inter-molecular phonons of crystalline C_{60} . For Ne, on the other hand, there is a clear overlap of the translational peak with the region of high phonon density, as can be seen in the INS spectrum (supplementary material). The interaction with inter-molecular lattice modes may also explain why the frequencies of the ${}^{20}\text{Ne}$ and ${}^{22}\text{Ne}$ translational peaks do not agree with the theoretical prediction.

The additional structure above the main absorption peak at low temperature could be explained by merohedral disorder. It was shown theoretically that the two lattice orientations of C_{60} molecules produce different electric field gradients at the C_{60} cage centers. The interaction of these electric field gradients with the molecular quadrupole moments splits the rotational levels of endohedral molecules.³³ Although the noble gas atoms lack a quadrupole moment, it is possible that the atom has a different potential function, Eq. (1) in the hexagonal and pentagonal sites. There are two experimental observations that support this idea in the case of $\text{Ne}@C_{60}$. First, the behavior of the $\text{Ne}@C_{60}$ 60 cm^{-1} line is consistent with transitions starting from the ground state (supplementary material). Second, the ratio of the areas of 56.6 and 60 cm^{-1} peaks for $\text{Ne}@C_{60}$ is 8:2 (supplementary material), which is consistent with the relative population of pentagonal and hexagonal sites in C_{60} at low temperature.³⁰ The temperature dependence and the spectral weight of the 87 cm^{-1} line of $\text{Kr}@C_{60}$ are not possible to evaluate reliably because it overlaps with the spectral lines of the main site. We have no experimental evidence that $\text{Ar}@C_{60}$ has any side peaks that can be related to the minority site, Fig. 3. However, a clear minority side-peak was observed for $\text{He}@C_{60}$.²⁴

To summarize, we have observed THz peaks from the translation of Ne, Ar, and Kr atoms inside fullerene cages. The THz spectra, and their temperature-dependence, are mainly consistent with confinement of the atoms by an anharmonic spherical potential. The translational frequency of He, Ar, and Kr is close to 90 cm^{-1} (2.7 THz) although the mass changes by a factor of 20 from He to Kr. This is because the increase in mass of the endohedral atom and its accompanying increase in size lead to opposite influences on the translational frequency. The increase in mass decreases the translational frequency, while the increases in size leads to a steeper confining potential, which increases the translational frequency. The combination of mass and atom size sets $\text{Ne}@C_{60}$ to the lower frequency side from other atoms to 57 cm^{-1} . The anharmonic part of the potential is positive, $V_4 > 0$, and the anharmonicity weakens with the increase of the atom size. Since the anharmonicity of the heavier atoms is not as large as for the lighter helium, the peaks are not resolved in the spectrum, and instead, the anharmonicity leads to a broadening and shift of the peak to higher frequency with an increase in temperature.

SUPPLEMENTARY MATERIAL

The supplementary material includes technical details of the inelastic neutron scattering measurements and the subtraction of the empty C_{60} spectrum from the $\text{Ne}@C_{60}$ spectrum; the details of how the THz absorption spectra were calculated and the baseline subtracted and additional data about $\text{Ne}@C_{60}$ spectra are included; and the induced dipole moments of atoms that are compared and the dependence of LJ potential curves on the direction of atom displacement that is plotted.

ACKNOWLEDGMENTS

This research was supported by the Estonian Ministry of Education, personal research funding PRG736; the European Regional Development Fund, Project No. TK134; and EPSRC under Grant Nos. EP/P009980/1 and EP/T004320/1 of UK. Use of the INS

spectroscopy setup was granted by the ILL through Proposal No. 7-04-176 (doi:10.5291/ILL-DATA.7-04-176). M.A. acknowledges the ILL for a financial support.

AUTHOR DECLARATIONS

Conflict of Interest

The authors have no conflicts to disclose.

Author Contributions

M.W., G.H., S.B., and R.J.W. carried out synthesis and purification of endofullerenes. G.R.B., M.J.-R., M.A., and S.R. performed the INS experiments and processed the INS data. T.J., A.S., U.N., and T.R. performed the THz experiments and processed the THz data. T.J., A.S., and T.R. derived the potential parameters by fitting the THz spectra. G.R.B. calculated the LJ potential functions. T.J. and A.S. wrote an initial draft of the paper. T.R. and M.H.L. developed the concept of the paper. All authors reviewed the manuscript.

Tanzeeha Jafari: Data curation (equal); Formal analysis (equal); Visualization (equal); Writing – original draft (equal); Writing – review & editing (equal). **Anna Shugai:** Data curation (equal); Formal analysis (equal); Visualization (equal); Writing – original draft (equal); Writing – review & editing (equal). **Urmaz Nagel:** Funding acquisition (equal); Resources (equal); Software (lead); Writing – review & editing (equal). **George Razvan Bacanu:** Data curation (equal); Formal analysis (equal); Methodology (equal); Visualization (equal); Writing – review & editing (equal). **Mohamed Aouane:** Data curation (equal); Formal analysis (equal); Writing – review & editing (supporting). **Monica Jiménez-Ruiz:** Data curation (equal); Formal analysis (equal); Writing – review & editing (supporting). **Stéphane Rols:** Data curation (equal); Formal analysis (equal); Funding acquisition (equal); Resources (equal); Supervision (equal); Writing – review & editing (equal). **Sally Bloodworth:** Resources (equal); Writing – review & editing (equal). **Mark Walkey:** Resources (equal); Writing – review & editing (supporting). **Gabriela Hoffman:** Resources (equal); Writing – review & editing (supporting). **Richard J. Whitby:** Funding acquisition (equal); Resources (equal); Supervision (equal); Writing – review & editing (equal). **Malcolm H. Levitt:** Conceptualization (equal); Funding acquisition (equal); Project administration (equal); Supervision (equal); Validation (equal); Writing – original draft (equal); Writing – review & editing (equal). **Toomas Rööm:** Conceptualization (equal); Funding acquisition (equal); Methodology (equal); Project administration (equal); Resources (equal); Supervision (equal); Validation (equal); Writing – original draft (equal); Writing – review & editing (equal).

DATA AVAILABILITY

The data that support the findings of this study are available from the corresponding author upon reasonable request.

REFERENCES

- ¹K. Komatsu, M. Murata, and Y. Murata, “Encapsulation of molecular hydrogen in fullerene C₆₀ by organic synthesis,” *Science* **307**, 238–240 (2005).
- ²S. Bloodworth and R. J. Whitby, “Synthesis of endohedral fullerenes by molecular surgery,” *Commun. Chem.* **5**, 121 (2022).

- ³K. Kurotobi and Y. Murata, “A single molecule of water encapsulated in fullerene C₆₀,” *Science* **333**, 613–616 (2011).
- ⁴A. Krachmalnicoff, R. Bounds, S. Mamone, S. Alom, M. Concistré, B. Meier, K. Kouřil, M. E. Light, M. R. Johnson, S. Rols, A. J. Horsewill, A. Shugai, U. Nagel, T. Rööm, M. Carravetta, M. H. Levitt, and R. J. Whitby, “The dipolar endofullerene HF@C₆₀,” *Nat. Chem.* **8**, 953–957 (2016).
- ⁵S. Bloodworth, G. Sotinova, S. Alom, S. Vidal, G. R. Bacanu, S. J. Elliott, M. E. Light, J. M. Herniman, G. J. Langley, M. H. Levitt, and R. J. Whitby, “First synthesis and characterization of CH₄@C₆₀,” *Angew. Chem., Int. Ed.* **58**, 5038–5043 (2019).
- ⁶S. Bloodworth, G. Hoffman, M. C. Walkey, G. R. Bacanu, J. M. Herniman, M. H. Levitt, and R. J. Whitby, “Synthesis of Ar@C₆₀ using molecular surgery,” *Chem. Commun.* **56**, 10521–10524 (2020).
- ⁷G. Hoffman, M. C. Walkey, J. Gräsvik, G. R. Bacanu, S. Alom, S. Bloodworth, M. E. Light, M. H. Levitt, and R. J. Whitby, “A solid-state intramolecular Wittig reaction enables efficient synthesis of endofullerenes including Ne@C₆₀, ³He@C₆₀, and HD@C₆₀,” *Angew. Chem., Int. Ed.* **60**, 8960–8966 (2021).
- ⁸G. Hoffman, G. R. Bacanu, E. S. Marsden, M. C. Walkey, M. Sabba, S. Bloodworth, G. J. Tizzard, M. H. Levitt, and R. J. Whitby, “Synthesis and ⁸³Kr NMR spectroscopy of Kr@C₆₀,” *Chem. Commun.* **58**, 11284–11287 (2022).
- ⁹T. Weiske, T. Wong, W. Krätschmer, J. K. Terlouw, and H. Schwarz, “The Neutralization of HeC₆₀⁺ in the gas phase: Compelling evidence for the existence of an endohedral structure for He@C₆₀,” *Angew. Chem., Int. Ed.* **31**, 183–185 (1992).
- ¹⁰F. Cimpoesu, S. Ito, H. Shimotani, H. Takagi, and N. Dragoë, “Vibrational properties of noble gas endohedral fullerenes,” *Phys. Chem. Chem. Phys.* **13**, 9609–9615 (2011).
- ¹¹G. R. Bacanu, T. Jafari, M. Aouane, J. Rantaharju, M. Walkey, G. Hoffman, A. Shugai, U. Nagel, M. Jiménez-Ruiz, A. J. Horsewill, S. Rols, T. Rööm, R. J. Whitby, and M. H. Levitt, “Experimental determination of the interaction potential between a helium atom and the interior surface of a C₆₀ fullerene molecule,” *J. Chem. Phys.* **155**, 144302 (2021).
- ¹²A. Takeda, Y. Yokoyama, S. Ito, T. Miyazaki, H. Shimotani, K. Yakigaya, T. Kakiuchi, H. Sawa, H. Takagi, K. Kitazawa, and N. Dragoë, “Superconductivity of doped Ar@C₆₀,” *Chem. Commun.* **2006**, 912–914.
- ¹³G. R. Bacanu, J. Rantaharju, G. Hoffman, M. C. Walkey, S. Bloodworth, M. Concistré, R. J. Whitby, and M. H. Levitt, “An internuclear J-coupling of ³He induced by molecular confinement,” *J. Am. Chem. Soc.* **142**, 16926–16929 (2020).
- ¹⁴N. Dragoë, A. M. Flank, P. Lagarde, S. Ito, H. Shimotani, and H. Takagi, “Molecular thermal contraction of the Ar@C₆₀ endohedral fullerene,” *Phys. Rev. B* **84**, 155448 (2011).
- ¹⁵E. K. Campbell, E. S. Reedy, J. Rademacher, R. J. Whitby, and G. Hoffman, “Electronic spectroscopy of He@C₆₀⁺ for astrochemical consideration,” *Astrophys. J.* **897**, 88 (2020).
- ¹⁶K. Yamamoto, M. Saunders, A. Khong, R. J. Cross, M. Grayson, M. L. Gross, A. F. Benedetto, and R. B. Weisman, “Isolation and spectral properties of Kr@C₆₀, a stable van der Waals molecule,” *J. Am. Chem. Soc.* **121**, 1591–1596 (1999).
- ¹⁷M. S. Syamala, R. J. Cross, and M. Saunders, “¹³³Xe NMR spectrum of xenon inside C₆₀,” *J. Am. Chem. Soc.* **124**, 6216–6219 (2002).
- ¹⁸M. Frunzi, R. J. Cross, and M. Saunders, “Effect of xenon on fullerene reactions,” *J. Am. Chem. Soc.* **129**, 13343 (2007).
- ¹⁹L. Pang and F. Brisse, “Endohedral energies and translation of fullerene-noble gas clusters G@Cn (G = helium, neon, argon, krypton, and xenon: n = 60 and 70),” *J. Phys. Chem.* **97**, 8562–8563 (1993).
- ²⁰M. S. Son and Y. K. Sung, “The atom-atom potential. Exohedral and endohedral complexation energies of complexes of X@C₆₀ between fullerene and rare-gas atoms (X = He, Ne, Ar, Kr, and Xe),” *Chem. Phys. Lett.* **245**, 113–118 (1995).
- ²¹H. A. Jiménez-Vázquez and R. J. Cross, “Equilibrium constants for noble-gas fullerene compounds,” *J. Chem. Phys.* **104**, 5589–5593 (1996).
- ²²S. Patchkovskii and W. Thiel, “Equilibrium yield for helium incorporation into buckminsterfullerene: Quantum-chemical evaluation,” *J. Chem. Phys.* **106**, 1796–1799 (1997).
- ²³C. Wang, M. Straka, and P. Pyykkö, “Formulations of the closed-shell interactions in endohedral systems,” *Phys. Chem. Chem. Phys.* **12**, 6187–6203 (2010).
- ²⁴T. Jafari, G. R. Bacanu, A. Shugai, U. Nagel, M. Walkey, G. Hoffman, M. H. Levitt, R. J. Whitby, and T. Rööm, “Terahertz spectroscopy of the helium endofullerene He@C₆₀,” *Phys. Chem. Chem. Phys.* **24**, 9943–9952 (2022).

- ²⁵A. L. R. Bug, A. Wilson, and G. A. Voth, "Nonlinear vibrational dynamics of a neon atom in fullerene C_{60} ," *J. Phys. Chem.* **96**, 7864–7869 (1992).
- ²⁶S. Flügge, *Practical Quantum Mechanics* (Springer-Verlag, Berlin, 1971), Vol. 1.
- ²⁷A. Shugai, U. Nagel, Y. Murata, Y. Li, S. Mamone, A. Krachmalnicoff, S. Alom, R. J. Whitby, M. H. Levitt, and T. Ródm, "Infrared spectroscopy of an endohedral water in fullerene," *J. Chem. Phys.* **154**, 124311 (2021).
- ²⁸F. Leclercq, P. Damay, M. Foukani, P. Chieux, M. C. Bellissent-Funel, A. Rassat, and C. Fabre, "Precise determination of the molecular geometry in fullerene C_{60} powder: A study of the structure factor by neutron scattering in a large momentum-transfer range," *Phys. Rev. B* **48**, 2748–2758 (1993).
- ²⁹J. Mejja, T. B. Coplen, M. Berglund, W. A. Brand, P. De Bièvre, M. Gröning, N. E. Holden, J. Irrgeher, R. D. Loss, T. Walczyk, and T. Prohaska, "Isotopic compositions of the elements 2013 (IUPAC Technical Report)," *Pure Appl. Chem.* **88**, 293–306 (2016).
- ³⁰W. I. F. David, R. M. Ibberson, T. J. S. Dennis, J. P. Hare, and K. Prassides, "Structural phase transitions in the fullerene C_{60} ," *Europhys. Lett.* **18**, 219–225 (1992).
- ³¹P. A. Heiney, "Structure, dynamics and ordering transition of solid C_{60} ," *J. Phys. Chem. Solids* **53**, 1333–1352 (1992).
- ³²S. Rols, C. Bousige, J. Cambedouzo, P. Launois, J.-L. Sauvajol, H. Schober, V. N. Agafonov, V. A. Davydov, and J. Ollivier, "Unravelling low lying phonons and vibrations of carbon nanostructures: The contribution of inelastic and quasi-elastic neutron scattering," *Eur. Phys. J.: Spec. Top.* **213**, 77–102 (2012).
- ³³P. M. Felker, V. Vlček, I. Hietanen, S. FitzGerald, D. Neuhauser, and Z. Bačić, "Explaining the symmetry breaking observed in the endofullerenes $H_2@C_{60}$, $HF@C_{60}$, and $H_2O@C_{60}$," *Phys. Chem. Chem. Phys.* **19**, 31274–31283 (2017).

Curriculum Vitae

1. Personal data

Name	Tanzeeha Jafari
Date and place of birth	13 April 1984, Sialkot, Pakistan
Nationality	Pakistani

2. Contact information

Address	National Institute of Chemical Physics and Biophysics Akadeemia tee 23, 12618, Tallinn, Estonia
Phone	+372 53974925
E-mail	tanzeehajafari@hotmail.com

3. Education

2019-...	Tallinn University of Technology, School of Science, Engineering physics, PhD
2014-2016	International Islamic University Islamabad, Pakistan, Department of Physics, Master of Philosophy in Physics, MS
2010-2012	University of Wah, Department of Physics, Master of science in Physics, MSc
2006-2008	Preston University, Faculty of Science, Islamabad, Pakistan Master of science in Electronics, MSc
2002-2004	F. G College for Women F-7/2 Islamabad, Pakistan, Bachelor of Sciences, BSc

4. Language competence

Urdu	native
English	full professional

5. Professional employment

2022- ...	National Institute of Chemical Physics and Biophysics, Junior Researcher
2017-2019	International Islamic University, Islamabad, Physics Lecturer
2017-2019	Army Public School Boys wing Westridge-111, Physics Lecturer

7. Computer skills

- Document preparation: LaTeX, Microsoft Office
- Programming languages: C++, Matlab, Wolfram Mathematica
- Scientific packages: OPUS, Origin

8. Defended thesis

- 2016, Synthesis and Characterization of tin and tin-oxide nanostructure, MS, supervisors PhD Shaista Shahzada, International Islamic University Islamabad

9. Field of research

- FIELD OF RESEARCH: Natural Sciences; Discipline: Applied Physics/ Chemical Physics ; SPECIALIZATION: Quantum dynamics, spectroscopy, low temperature physics, SPECIALTY: infrared and THz spectrometry of endohedral species at low temperatures

10. Scientific work

Papers

1. G. R. Bacanu, T. Jafari, M. Aouane, J. Rantaharju, M. Walkey, G. Hoffman, A. Shugai, U. Nagel, M. Jiménez- Ruiz, A. J. Horsewill, S. Rols, T. Rõõm, R. J. Whitby, and M. H. Levitt, "Experimental determination of the interaction potential between a helium atom and the interior surface of a C₆₀ fullerene molecule" *J. Chem. Phys.*, vol. 155, p. 144302, October 2021.
2. T. Jafari, G. R. Bacanu, A. Shugai, U. Nagel, M. Walkey, G. Hoffman, M. H. Levitt, R. J. Whitby, and T. Rõõm, *Phys. Chem. Chem. Phys.* 24, 9943–9952 (2022) "Terahertz spectroscopy of the helium endofullerene He@C₆₀," *Phys. Chem. Chem. Phys.*, vol. 24, p. 9943, April 2022.
3. T. Jafari, A. Shugai, U. Nagel, G. R. Bacanu, M. Aouane, M. Jiménez- Ruiz, S. Rols, S. Bloodworth, M. Walkey, G. Hoffman, R. J. Whitby, M. H. Levitt, and T. Rõõm, "Ne, Ar, and Kr oscillators in the molecular cavity of fullerene C₆₀," *J. Chem. Phys.*, vol. 158, p. 234305, June 2023.
4. V. K. Vyas, G. R. Bacanu, M. Soundararajan, E. S. Marsden, T. Jafari, A. Shugai, M. E. Light, U. Nagel, T. Rõõm, M. H. Levitt and R. J. Whitby "Squeezing formaldehyde into C₆₀ fullerene," *Nat. Commun.*, vol 15, p 2515, March 2024.

Conference presentations

1. T. Jafari. *Synthesis and Characterization of Tin and Tin-oxide nanoparticles using Laser Ablation* , 2nd International Symposium on Advanced Materials and Nano devices, 14 Nov - 16 Nov 2016, Islamabad, Pakistan
2. T. Jafari. *Synthesis and Characterization of Tin and Tin-oxide nanoparticles using Laser Ablation*, The first International Conference on Physics and Mathematics, 2017, Islamabad, Pakistan

Elulookirjeldus

1. Isikuandmed

Nimi	Tanzeeha Jafari
Sünniaeg ja -koht	04.13.1984, Sialkot, Pakistan
Kodakondsus	pakistan

2. Kontaktandmed

Adress	Keemilise ja Bioloogilise Füüsika Instituut, Akadeemia tee 23, 12618, Tallinn, Estonia
Telefon	+372 53974925
E-post	tanzeehajafari@hotmail.com

3. Haridus

2019-...	Tallinna Tehnikaülikool, Loodusteaduskond, Tehniline füüsika, doktoriõpe
2014-2016	Rahvusvaheline Islami Ülikool Islamabad, Pakistan, füüsika osakond, füüsika filosoofia magister, MS
2010-2012	Wah'i ülikool, füüsika osakond, füüsika magister, MSc
2006-2008	Prestoni Ülikool, Loodusteaduste teaduskond, Islamabad, Pakistan Magister elektroonikas, MSc Tehniline füüsika, MSc
2002-2004	F. G Naistekolledž F-7/2 Islamabad, Pakistan, Teaduste bakalaureus, BSc

4. Keelteoskus

urdu keel	emakeel
inglise keel	kõrgtase

5. Teenistuskäik

2022- ...	Keemilise ja Bioloogilise Füüsika Instituut nooremteadur
2017-2019	Rahvusvaheline Islami Ülikool, Islamabad, füüsika lektor
2017-2019	Army Public School Boys tiib Westridge-111, füüsika lektor

7. Arvuti oskused

- Kontoritarkvara: LaTeX, Microsoft Office
- Programmeerimiskeeled: C++, Matlab, Wolfram Mathematica
- Teadustarkvara paketid: OPUS, Origin

8. Kaitstud lõputööd

- 2016, tina ja tinaoksiidi nanostruktuuri süntees ja iseloomustus, MS, juhendajad PhD Shaista Shahzada, Islamabadi rahvusvaheline islamiülikool

9. Teadustöö põhisuunad

- VALDKOND: loodusteadused; Distsipliin: rakendusfüüsika/ keemiline füüsika ; SPET-SIALISATSIOON: kvantdünaamika, spektroskoopia, madala temperatuuri füüsika, ERI-ALA: endoedriliikide infrapuna- ja THz spektromeetria madalatel temperatuuridel

10. Teadustegevus

Teadusartiklite ja konverentsiettekannete loetelu on toodud ingliskeelse elulookirjelduse juures.

ISSN 2585-6901 (PDF)
ISBN 978-9916-80-249-6 (PDF)